NEW DEVELOPMENTS IN THE THz FIELD FOR IMAGING APPLICATIONS

Memoria de la Tesis Doctoral realizada por

David Etayo Salinas

Y dirigida por

Dr. Ramón Gonzalo García

Para optar al grado de

Doctor en Ingeniería de Telecomunicación

Universidad Pública de Navarra

Departamento de Ingeniería Eléctrica y Electrónica

Pamplona, Marzo 2014

May the Force be with you

AGRADECIMIENTOS

Mediante estas líneas quisiera agradecer a todos aquellos que me han ayudado y apoyado hasta llegar a este momento.

En primer lugar, como no, a ti Ramón, por descubrirme este mundo tan apasionante como es la investigación. Siempre dispuesto a hablar sobre cualquier duda o cualquier problema. Estoy seguro que sin muchos de tus consejos no hubiera llegado hasta aquí.

Juan Carlos, con la cantidad de horas de medidas, pruebas y simulaciones que hemos pasado, gran parte de que haya llegado a escribir esto es gracias a ti. En cualquier momento, siempre has tenido la puerta abierta para hablar de lo que sea.

Iñigo, gracias por resolverme dudas que ni tan siquiera era capaz de expresar, por generar siempre una idea o un punto de vista diferente.

A todo el grupo de Antenas, Jorge y Carlos, siempre dispuestos a ayudar con el tema que fuera y a los jóvenes del grupo, Irina, Inés, Liberal, Itziar, Ainara, Belén y Amagoia por esas horas de cafés, congresos y cursos. También a la gente de la uni, Paola, Mikel, Leo…por esos buenos ratos

I would like to thank people from Lehrstuhl Höchstfrequenztechnik und Quantenelektronik in Siegen, especially to you, Prof. Haring Bolívar, and also to Gunnar, Anna, Dustin, Christian… Make extensive this acknowledgment to the rest of the group. It has been a great experience to work with you. Danke.

También me gustaría agradecer a la Universidad Pública de Navarra y al Gobierno de Navarra por el apoyo económico.

A mis amigos de toda la vida, Javi, Ramón, Solano, Raúl, Mikel, Berrade, Blanco y Jorge. A mis chicoteros de la carrera y más, Mako y Ras. Y a sus respectiv@s. Gracias por estar ahí.

A mis padres, Miguel y Ana, por estos años de apoyo y ánimos, por aguantarme a las duras y a las maduras y por alegrarse siempre por cualquier buena noticia. Gracias de corazón. También a mi abuela, que siempre ha mostrado interés, aunque no le quedara muy claro en que trabajaba su nieto. Y al resto de mis abuelos, que aunque no estén, o no vean esto, espero que estén orgullosos de su nieto.

Como siempre, lo mejor se guarda para el final. A ti, Maitane, Mai, que siempre estas a mi lado. Escribir en unas pocas líneas por qué te agradezco esto es imposible. Sin ti seguro esto no hubiera llegado a buen puerto. Me has aguantado cuando llegaban los momentos duros y me has hecho ver que, aun cuando todo parecía imposible, se podía tirar para adelante. Gracias por animarme, por hacerme reír y por soportarme. No sé cómo decírtelo mejor, o cómo expresarlo, pero lo que pienso, ya lo sabes.

Y a todos aquellos que han estado cerca de mi durante todos estos años. Seguro que algún nombre se me ha pasado. A todos vosotros, gracias.

ABSTRACT

The aim of this thesis is to go a step forward in the use of Terahertz (THz) technology within the field of imaging applications. Nowadays, THz radiation appears as a very interesting frequency range to obtain images, as related in the numerous publications. Conversely, although there are several examples of imaging in this range, it is still not possible to identify the material that it is imaged. That is why one of the objectives of this thesis will be to add new materials to the actual database. Thus, several systems have been implemented to characterize materials in the range of THz for this dissertation.

Due to these reasons, a THz imaging system that allows to obtain images for this dissertation has been developed. Thus, the first section of the thesis is focused on the implementation of that system. The design uses a network analyzer as emitter/detector of THz radiation and it measures the magnitude and/or phase of the detected signal in transmission and/or reflection configuration, in frequency and/or time domain. Furthermore, this design allows to control other imaging parameters, such as resolution, bandwidth or imaging time.

Second part of the thesis is focused in the identification of the material detected by the imaging system. First of all, the parameters used for the characterization are defined: Permittivity (or dielectric constant), refractive index, absorption coefficient and absorbance. Once they have been defined, some theoretical models to calculate those parameters are descripted. These models are: a model for (electrically) thick samples with one

interface, a model for (electrically) thin samples with two interfaces and a ellipsometry model. Note that the model for thin samples is further expanded as the sample can be composed by only one material, powder sample or a dissolute sample.

Several characterization systems based on these models have been implemented. In particular, a system able to measure thick sample in reflection configuration and based on a network analyzer, an ellipsometer and a time-domain spectrometer (a commercial THz-TDS used as a reference). In order to show the capabilities of those systems, several explosives (TNT, RDX, PETN, mine gunpowder and bullet gunpowder) have been characterized before detonation. It is important to remark that, for the first time, mine gunpowder has been measured in this thesis. Furthermore, also for the first time, TNT, RDX and PETN have been characterized after the detonation process. Thus, these explosives can be identified after a terrorist action. Finally, for the sake of comparison of THz-TDS and ellipsometry methods, the refractive index of the explosives has been obtained with both systems.

To conclude with the second part, some applications for agriculture, food industry and security and defense sectors are commented. For agriculture applications, a preliminary study to check the capabilities of the THz images to measure the water content level in transmission and reflection configuration during three days are presented. Those variations are not detected by human eye inspection but they are clearly identified in the THz range. Secondly, a study for a quality control system for food industry is described. It detects glass, metal, paper or plastic parts inside the production chain also in transmission and reflection configuration. Finally, a study (using the THz-TDS) focused on the influence of the additives and the manufacturing process in the absorbance of explosives is performed.

Third part of this dissertation presents the design, fabrication and measurement of a dual band detector operating at IR and THz frequencies. This device is based on Fresnel zones theory; a spiral antenna with the objective of measure, in the same device and at the same time, at 0.427 THz (THz frequency range) and 25 THz (IR range) has been developed. It is important to remark that, due to the use of Fresnel Zones, an improvement of 4.5 times on the power level detected in the IR range is obtained.

As a result of this dissertation, an article in an international journal has been published and two more are under review. Furthermore, 7 communications have been presented in international conferences and three more in national conferences.

RESUMEN

Con esta tesis se pretende avanzar en el desarrollo de la tecnología de Terahercios (THz) dentro del campo de las aplicaciones de imagen. Actualmente, los THz se presentan como un rango frecuencial muy interesante para la obtención de imágenes, tal y como se ve reflejado en los numerosos trabajos presentes en la literatura. Por otro lado, aunque se han obtenido cuantiosas imágenes en este rango, aun no es posible identificar el material que compone la muestra. Es por esto que uno de los objetivos de esta tesis es completar las bases de datos de materiales existentes actualmente. Para ello, se han implementado diferentes sistemas que permiten la caracterización electromagnética de diferentes materiales en el rango de los THz.

Debido a estas razones, se hizo prioritario disponer de un sistema de imagen en THz con el fin de obtener imágenes para el resto de la tesis. Por ello, la primera parte se centra en la implementación de dicho sistema. El diseño usa un analizador de redes como emisor/detector y es capaz de medir tanto en transmisión como en reflexión proporcionando la magnitud y/o fase de la señal detectada, en el dominio del tiempo y/o de la frecuencia. Además de estas configuraciones, también es posible actuar sobre otros parámetros que influyen en el proceso de adquisición o en la calidad de la propia imagen, como son la resolución, el ancho de banda de trabajo o el tiempo invertido en la toma de imágenes.

La segunda parte de la tesis se centra en la identificación de los materiales detectados con el sistema de imagen. Para ello, se definen los

parámetros electromagnéticos con los que se van a caracterizar las muestras. Estos son permitividad (o constante dieléctrica), índice de refracción, coeficiente de absorción y absorbancia. Una vez definidos los parámetros, se describen diversos modelos teóricos que calculan dichos parámetros en función del tipo de muestra: modelo para una muestra gruesa (comparada con la longitud de onda) con una única interfaz, modelo para una muestra fina (también comparada con la longitud de onda) con dos interfaces y un modelo para elipsometría. Cabe destacar que en el caso del modelo para una muestra fina, se especifican modelos más detallados en función de la composición de la muestra: el primer caso describe la muestra formada por un único material, el segundo se emplea para muestras en polvo y el último para muestras en disolución.

Una vez completados los modelos teóricos, se han implementado varios sistemas de medida que se basan en ellos. En particular, se describe un sistema capaz de medir muestras gruesas en reflexión y que se basa en un analizador de redes, un elipsómetro y un espectrómetro en el dominio del tiempo (THz-TDS, un sistema comercial que se utiliza como referencia). Para demostrar las capacidades de estos sistemas, se han caracterizado numerosos explosivos (TNT, RDX, PETN, pólvora de mina y pólvora de munición) antes de ser detonados. Es importante destacar que, por vez primera, en esta tesis se muestra la caracterización de la pólvora de mina en este rango. Es más, también por primera vez, los explosivos TNT, RDX y PETN se han caracterizado una vez detonados, lo que permite que sean identificados después de una acción terrorista. Finalmente, con el objetivo de comparar dos técnicas (THz-TDS y elipsometría), los explosivos han sido caracterizados con su índice de refracción en ambos sistemas.

Para concluir esta segunda parte, se han presentado varias aplicaciones de un sistema de THz centradas en la agricultura, la industria alimentaria y seguridad y defensa. Para un sistema con aplicación en la agricultura, se presenta un estudio preliminar de las capacidades de los THz para medir pequeñas variaciones del contenido en agua de una planta, tanto en transmisión como en reflexión, a lo largo de tres días. Estos cambios no son apreciables por el ojo humano, pero son claramente identificables en el rango de los THz. Para la industria alimentaria, el estudio se basa en el uso de THz para un sistema de control de calidad que detecte posibles cuerpos extraños, como vidrio, plástico metal o papel en la

cadena de producción. Al igual que en el caso anterior, se muestran resultados en transmisión y reflexión. Por último, se estudia la influencia de los aditivos y del proceso de fabricación en la absorbancia de los explosivos, mediante técnicas espectroscópicas.

Finalmente, la tercera parte de este trabajo presenta el diseño, fabricación y medida de un receptor que trabaja tanto en la banda de IR como en la banda de THz. Este detector se basa en la teoría de las zonas de Fresnel para diseñar una antena espiral y opera en el rango de los THz (0.427 THz) y en IR (25 THz), con el objetivo de proporcionar información complementaria en el mismo tiempo de observación. Además, debido al uso de las zonas de Fresnel, se consigue un aumento (en un factor 4.5) de Ganancia en la banda de IR.

Como resultado de este trabajo se ha publicado 1 artículo en una revista internacional, y 2 más están en proceso de revisión. Se han presentado 7 comunicaciones en conferencias internacionales y 3 en conferencias nacionales.

CONTENTS

CHAPTER I

INTRODUCTION: THz BACKGROUND AND APPLICATIONS

In this chapter, an introduction about THz technology is presented. Firstly, a short review about how to generate and detect THz waves is commented. Secondly, actual and promising applications for this frequency range are related. Finally, the scope of this dissertation is described.

I.1.-Background

The Terahertz region in the electromagnetic spectrum includes the range between the Microwaves and the Infrared (Fig. 1.1). Due to the situation in between the microwave frequency range and the optical techniques, THz frequency range provides the possibility of join the applications of both domains [Mittleman2003].

Note that also, ranges of the electromagnetic spectrum are named by its wavelength. In this case, the THz range also includes the submillimeter waves range as wavelengths change from 30 µm to 3 mm.

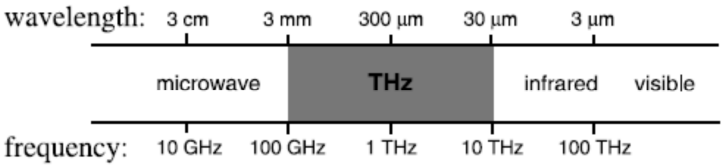

Fig. 1.1. Terahertz frequency range

The high operational frequency comparing with microwave, and the large wavelength comparing with the IR have focused the problem in how to generate and detect THz radiation due to the huge difficulty in finding sources and detectors working at these frequencies (1960s) [Abita1990]. Therefore, THz system did not come into popular used until 1970s [Chan2007] [Crowe2005].

Thus, first efforts (1960s and 1970s) were focused in the development of suitable sources, sensitive detectors and other components for the manipulation of the radiation in this frequency range.

The development of the far-infrarred gas laser and Schottky diode harmonic mixer in the mid-1970s inspired the first work in the THz image [Hartwick1976]. Unfortunately, these systems [Cheo1978] although suitable for laboratory demonstrations, were too complicate and specialized.

At the same time, the development of high-power laser sources was opening up new possibilities for THz systems. In the early 1970s tunable far-infrared radiation by using the difference-frequency generation technique in non-linear crystal was developed [Auston1973] [Yang1973]. This work

was used as a first step for developing terahertz time domain spectroscopy (THz-TDS). Hu and Nuss reported the first images using a THz-TDS system in 1995 using THz radiation [Hu1995].

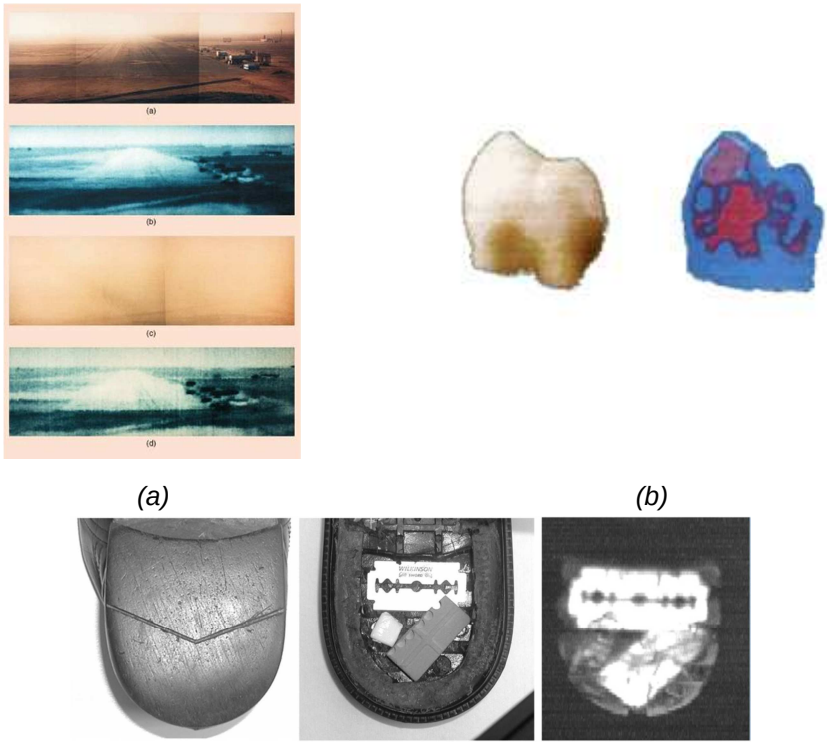

(a) *(b)*

(c)

Fig. 1.2. (a) THz Images obtained in different visibility condition, (b, left) photo of a Human tooth and (right) THz image of the same tooth, where the cavities are depicted in red color [Sim2009] *(c, left) Photo of the heel of a shoe, and (c, center) the hole inside it which contains a blade and plastic explosive. On the right side is the THz image of the heel.*

The exploitation of sub-millimeter wave regime (THz frequencies) is a natural progression in the quest to expand our vision. There are frequency bands where attenuation is relatively low in both air and mist, making them good candidates for the development of imaging systems [Thrane1995]. For example, THz radiation is attenuated least a million times through clouds

and sandstorms that radiation to visible or infrared frequencies. In addition, the images obtained in this frequency range are affected minimally by the sun or artificial lighting. Therefore, these systems also operate at low/high visibility during the day or night. It is this ability that makes THz radiation the best candidate for imaging in most low visibility conditions [Peiponen2007].

These THz images have recently aroused, large interest [Mittleman1996] mainly created by the large number of applications [Chan2007] in which these frequencies could be used, including surveillance, precision targeting, navigation, aircraft landing, refueling in clouds (see Fig. 1.2a), search and rescue, metal detection, vision through fog, concealed weapons (Fig 1.2c) or explosives detection in airports and other locations [Liu2006], wound and dental inspection (Fig 1.2b), skin inspection [Guan2011] and melanoma cancer detection [Siegel2004], passive tomography imaging and medical imaging [Beard2002].

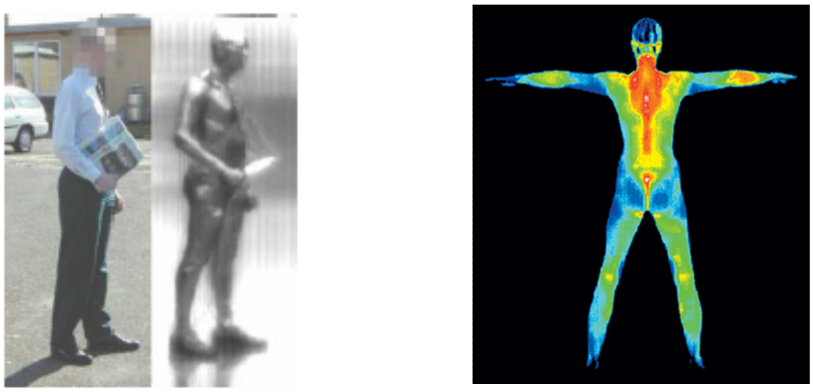

(a) *(b)*

Fig. 1.3. (a) Security application for THz images [Appleby2004] and (b) Infrared thermography [Meditherm].

Applications related above are typically implement in the IR region or in the microwave range (see Fig 1.1). Thus, THz waves allow taking images different from the visible spectrum [Hunsche1998] [Mittleman2003] (see Fig. 1.3). Also, the characterization of materials by spectrometry techniques is available, due to the wavelength size in the THz frequency range; instead of obtaining resonances by the atoms, in this range the resonances are

produced by the molecules (as the wavelength is larger than in the IR-UV range) [Beard2002].

Furthermore, typical submillimeter wave techniques, for emitter/receptor designing (based on multipliers or diodes), microwave imaging (see Fig. 1.4) [Bram2001] [Smith2001] [Martin2007] [May2009] or electromagnetic characterization (to obtain the parameters of the samples, such as refractive index or permittivity) can be used in this range [Martin1967] [Volk1985] [Volk1989] [Gum2009] to design THz sources/detectors, THz imaging and to characterize samples in this frequency range. It is important to remark that THz radiation is highly dependent on the water content that is why long distance communications are not possible with THz waves [Gebbie1970].

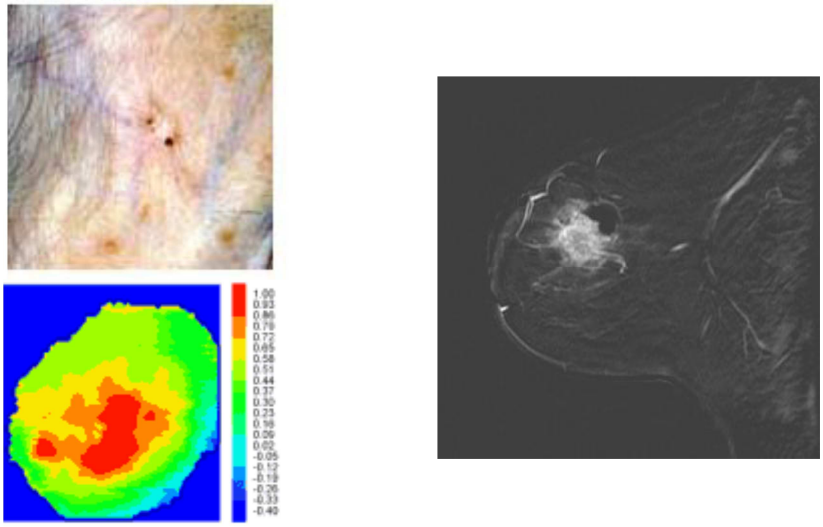

(a) *(b)*

Fig. 1.4. (a) Clinical photograph (up row) showing suspected basal cell carcinoma and THz image (bottom row) [Teraview] and (b) breast carnimona using millimeter wave imaging [Sciencecodex].

I.2.-THz radiation: generation and detection schemes

THz radiation can be generated (and detected) using optical techniques or millimeter-wave devices. This section is a short review of the THz generation and detection processes.

I.2.1.-Optical techniques

Photonic techniques are commonly used due to its high bandwidth available [Shen1976] [Fattinger1989] [Ferguson2002] [Lee2009]. As a function of the type of the sources uses for THz generation, pulsed signal or continuous wave signal will be obtained [Lee2009] [Jansen2010]. Both techniques use a photoconductive antenna [Wu1996a] [Wu1996b] [Mittleman2003] [Lee2009] as an emitter which is based on the photoconductive Auston switch [Auston1983] [Auston1984].

The detection process of the THz radiation is usually based on photodiodes or diodes UTC, as it is related in [Mukherjee2008], [Lee2009] and [Nagatsuma2009]. These devices generate electrical current proportional to the level of THz radiation detected. Note that usually, a heterodyne detector is used. This detector will be explained in Section I.2.2.2.2. In this case, the LO signal is optically generated.

I.2.2.-Electronic techniques

I.2.2.1.-Electronic generation

These techniques come from the microwave range. In that frequency range, it is very common to obtain higher (lower) frequencies using mixers and/or multipliers [Agilent][OML][VDI]. These devices transform the original low (high) frequency of the input signal to provide an output signal with higher (lower) frequency.

Electronic mixers give the possibility of achieve a high/low frequency by mixing two different signals. One of these signals is typically provided by a local oscillator and it is a fixed frequency (f_2). The second signal is the emitted/detected signal (f_1). With the addition (subtraction) of both signals, a

higher (lower) frequency is obtained (Fig. 1.5). Note that if f_1 is a ramp function, it is possible to cover a large bandwidth.

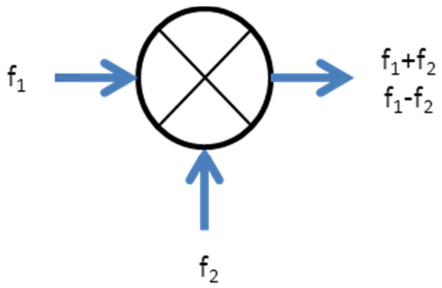

Fig. 1.5. Schematic of a harmonic mixer

Instead of using harmonic mixers, a sub-harmonic mixer can be used. Note that mixers provide a combination of multiple harmonic signals, such as $nf_1 \pm mf_2$ to obtain higher (lower) frequencies. Typically, for the case of harmonic mixers, n=m=1 because the output signal has more power. Also, sub-harmonic mixers are used. In that case, n=2 and m=1 [Sierra2003]. The output signal has lower power, but its frequency is higher than in the case of harmonic mixers.

The main problem of this technique is the difficulty of achieving very high frequencies (THz means 10^{12} cycles per second) by mixing low frequency signals (MHz or GHz). Other technique available in the microwave range is the use of multipliers. These devices are electronic circuits based on Schottky barrier diodes [Lee2009], in which the frequency of the output signal is the frequency of the input signal multiplied by factor (this factor depends on each multiplier). Thus, a higher frequency signal is obtained. Note that both devices (mixers and multipliers) can be used together to obtain THz radiation.

I.2.2.2.-Detection schemes

Several electronic-based detection techniques are available in the THz region based on antennas to collect the THz power into a detector

device [Sierra2003]. In this section, two of the most common techniques are introduced, homodyne and heterodyne detector.

I.2.2.2.1.-Homodyne detector

Direct detection (or homodyne detector) is the simplest technique (Fig. 1.6). It uses a Schottky barrier diode with a high cutoff frequency (1-10 THz). The main difficult of this technique is the sensitivity of the diode at THz range (it limits the minimum power level of the detected signal). Due to the simplicity of this scheme only power level is detected, as it has no phase reference [Nagatsuma2009].

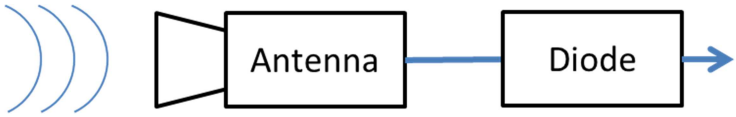

Fig. 1.6. Direct detection scheme

I.2.2.2.2.-Heterodyne Detector

To increase the sensitivity of the detector, a heterodyne detection system can be implemented [Lee2009] [Nagatsuma2009]. This scheme uses a LO signal which gates the received signal and fixes the instants of detection (Fig. 1.7). Note that the received signal is mixed with LO signal and an intermediate-frequency signal (IF signal) is obtained. Filters and selectors are tuned to work in this IF range.

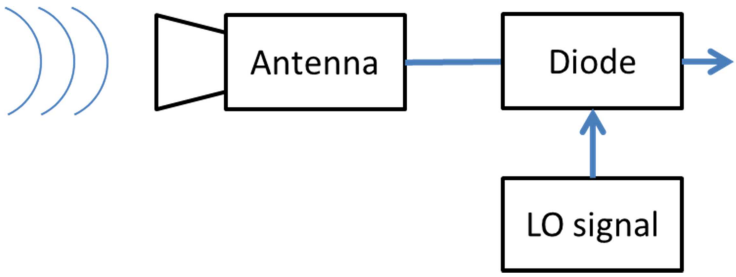

Fig. 1.7. Heterodyne detection scheme

This technique provides higher sensitivity that can be further enhanced according to the type of diode used as detector. As a difference with the previous case, the LO signal provides a phase reference, that is why, power and phase measurements can be achieved using heterodyne detection.

I.3.-THz applications

In this section, two important application fields of the THz radiation are introduced: THz imaging and electromagnetic characterization in the THz range.

I.3.1- THz technology for imaging

This frequency range allows a non-destructive (for instance, clothes are transparent to THz radiation. Thus, a THz image of a cover sample can be obtained), non-invasive (THz radiation can obtain a THz image from a security distance) and non-ionizing testing of the sample (unlike X-rays which emits ionizing radiation).

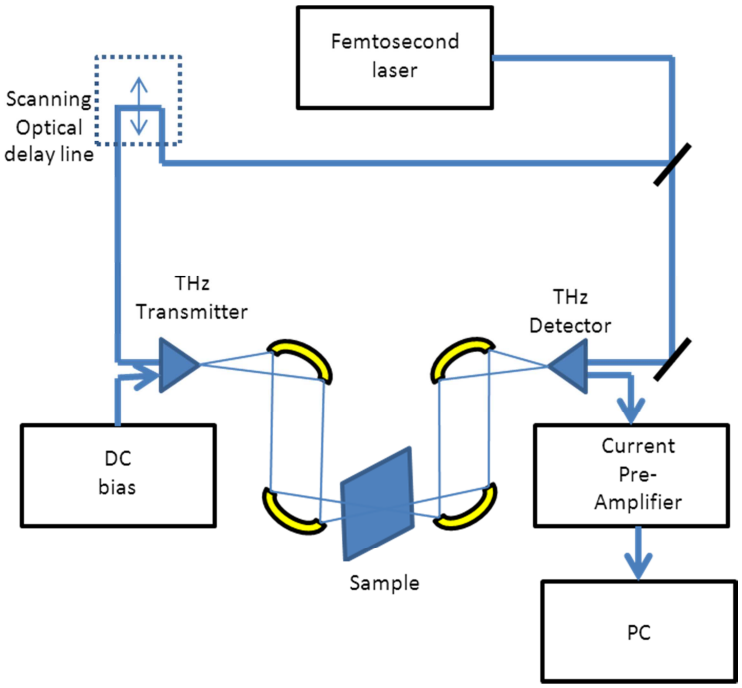

Fig. 1.8.THz-TDS spectrometer

Before the development of an imaging system for final applications, some tests at laboratory level have to be performed. The first THz imaging system, a time-domain spectrometer, was reported in 1995 [Hu1995] and it has been replicated several times [Mittleman1996] [Kindt1996] [Koch1998]. In this system, a THz pulse is emitted by the photoconductive antenna and focusing by optical elements (lenses or mirrors) into a sample (see Fig. 1.8). To map the whole sample, this one is moved by a positioning system. For each measured point in the sample, a pixel in the final image is obtained. A system similar to that illustrate in Fig. 1.8 was used in 1995 to obtain the first THz-TDS image of a leaf [Hu1995] which is depicted in Fig. 1.9. Note that, in this image the water content level is depicted due to the dependency of the THz radiation with the water content of the sample.

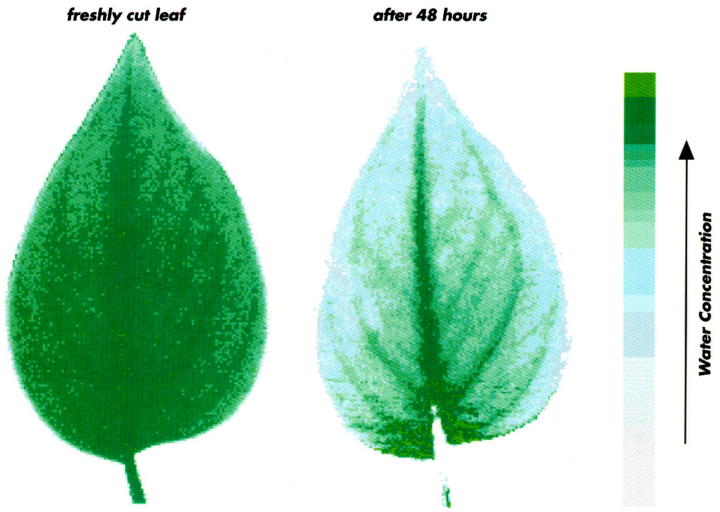

Fig. 1.9. First THz-TDS images of a leaf. [Hu1995]

In this figure it is possible to identify the leaf stack, veins and to study the water distribution inside the leaf due to the resolution achieved at this frequency range. Based on this high dependence of THz wave propagation on the water content, imaging in the THz wave range opens up new possibilities for non-destructive testing, imaging and sample characterization that can be used in industrial quality control processes and water content

detection in the agricultural and food industry [Parasoglou2009] [Federici2012].

These transmission measuring systems provide an adequate technique for thin samples or low-attenuation (transparent) samples for THz radiation. It means that the main fraction of the incident power over the sample goes through the sample and arrives to the detector. When that power arrives, it has information about the sample and its electromagnetic parameters. On the other hand, if the sample is opaque (high attenuation) to THz radiation or it is (electrically) thick; another technique is required because the level of transmitted power that arrives to the detector is very low. Thus, a reflection measuring system can be implemented for this scenario. As a substitute of the transmitted power through the sample, the reflected power by the sample is used. As in the case of transmission images, the reflected power provides electromagnetic information of the sample under test and it can be used for imaging, too [Balanis1989].

Furthermore, besides of represent magnitude of the reflected THz pulse, the time delay between pulses can be depicted [Pradarutti2007]. Using this representation, an analysis of the thickness, or the changes in the refractive index (in the direction of propagation of the THz pulse) of the sample can be performed, as time delay information can be translated into depth information, as it is illustrated in Fig. 1.10.

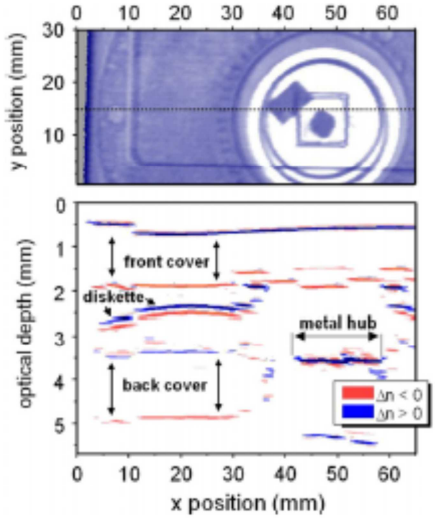

Fig. 1.10. Measuring of a diskette using time-domain representation [Mittleman1997]

Reflection technique allows measuring a sample using a simplified system comparing with transmission configuration, due to only a transmitter/receiver device is used. One of the most important limitations of this system is due to multipath and secondary reflected signals, but if the reflected signal is gated, a discrimination of the no-desired signal can be performed.

In addition to these representation standards (transmission and reflection techniques), the polarization of the THz beam can be used for imaging. Although the use of polarization techniques has not yet become widespread in the THz community, this promising area is worth a brief comment. The THz beam generated by a typical photoconductive antenna is linearly polarized [Rudd2000] [Rudd2001]. Electro-optic generation provides higher polarization purity than photoconductivity antennas and also, extremely purely polarizer THz beams can be obtained using wire grid polarizers.

On the other hand, control of the polarization can be quite challenging for anything other than pure linear polarization. However, linear polarization can provide a useful contrast mechanism in imaging [vdValk2005]. For

example, Fig. 1.11 shows terahertz transmission images of a plastic coin, illuminated with linearly polarized radiation.

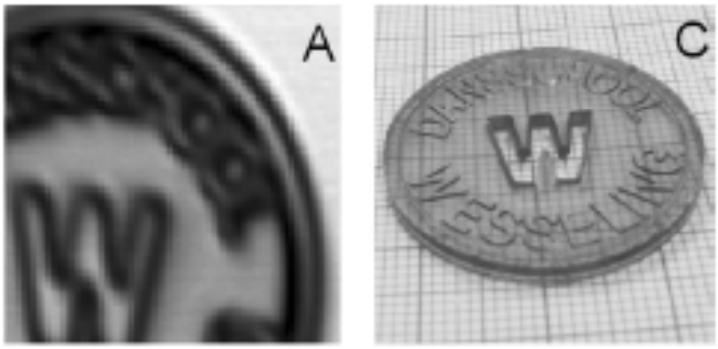

Fig. 1.11. Transmission images of a plastic coin illuminated with a linearly polarized terahertz beam. A Transmitted terahertz power parallel to the incident polarization, and C a photograph of the object. [vdValk2005].

The most common imaging system operates at only one frequency, in order to obtain a THz image in a short period of time [Lee2009]. The technology used for the generation/detection of the THz radiation can be optical or electric based [Peiponen2013] as both generation systems provides enough dynamic range at one single frequency. Some conditions of the final application (such as operational frequency) can take influence of the technology selection. Also, due to the requirements of the imaging applications, these systems can be designed for transmission/reflection configuration.

THz imaging systems have been designed for industrial applications (non-destructive inspection), or security applications (drugs or weapons detection) [Peiponen2013]. In these situations, the main problem of those systems is to determinate the material that they are imaging. They can detect suspicious objects but they cannot identify them. (Identify refers to characterize a sample by its electromagnetic parameters to determinate the material) [Kemp2011]. Thus, a characterization system has be to implemented in that range.

In this dissertation, an active imaging system for the 0.09-0.50 THz frequency range has been implemented. It is based on a network analyzer and provides transmission and reflection images for this thesis.

Furthermore, in order to improve the capabilities of the THz in the imaging field, a dual-band device based on Fresnel Theory has been designed in this thesis. This device works at THz frequencies and also in the IR range. Thus, it can be used as a front-end for an imaging application as it provides complementary information (THz and IR) at the same time.

I.3.2- Electromagnetic characterization in the THz range

The existence of molecular resonances in these frequencies has fostered the development of imaging and spectroscopy THz systems. These systems make use of the properties of the THz radiation (non-invasive, non-ionizing and non-destructive) and these resonances to complement the electromagnetic characterization information at different frequency ranges (such as IR, UV or visible) by dealing with the electromagnetic characterization of different materials using THz-TDS or THz-ellipsometry. As a consequence, material databases at these frequencies become an important issue [Choi2004] [Ung2007] [Yan2008].

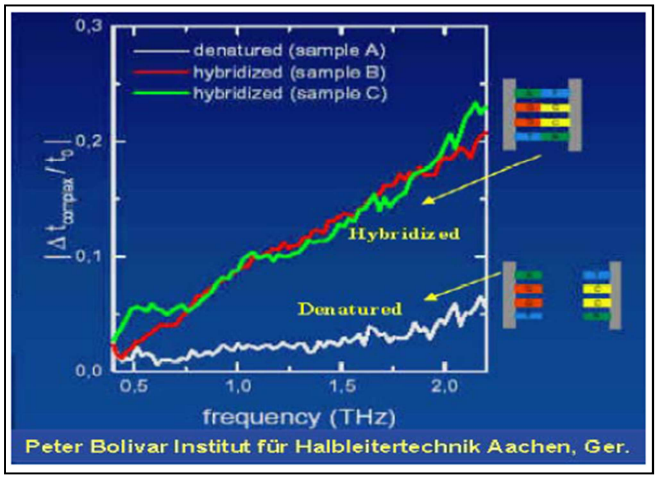

Fig. 1.12. DNA absorption for a hybridized chain (red/green) or denatured chain (white) [Haring2000].

This characterization is very important for the pharmaceutical industry to identify and differentiate drugs or medicines [Peiponen2013]. For instance, Fig. 1.12 shows the differences in absorption for hybridized chains and denatures chains of DNA. Furthermore, explosives and energetic compounds can be characterized in this frequency range opening new possibilities for security applications [Yamamoto2004] [Shen2004] [Naft2007] [Chen2007]. Finally, the determination of the parameters of the circuit substrates is a very important field for the development of new THz devices.

These systems have been demonstrated to be very useful and interesting at laboratory level to characterize samples. On the other hand, the use of them out of the laboratory is, nowadays, a challenge [Kemp2011] as these systems are not able to identify materials.

In this case, the bandwidth available is a very important parameter to characterize samples. As the THz system comes popular since 70's, it is very essential to characterize materials in this frequency range to know their properties. Note that as each material presents a different frequency response, a large bandwidth is required to identify it. It is necessary to determinate the refractive index or the absorbance spectrum of the sample for the available bandwidth. Thus, the most common electromagnetic characterization systems are based on optical sources to generate the THz beam, as this generation technique provides large bandwidth.

Furthermore, as polarization can be useful for imaging, as it has been introduced above, changes in this polarization can be used for electromagnetic characterization, as it is done in ellipsometry systems in the optical domain [Tomp2005]. This technique (ellipsometry) can be introduced in the THz domain, like spectrometry, to extend the possibilities of identify the sample under test.

Thus, in this dissertation some THz electromagnetic characterization systems have been implemented to measure samples in the THz range. These systems are able to characterize thick samples based on the use of a network analyzer and an ellipsometry system. Those developed systems allow measuring the refractive index, permittivity and/or absorbance of the sample under test.

Several explosives have been characterized in the THz range using these systems. Those explosives are PETN, RDX, TNT, bullet gunpowder and mine gunpowder. Furthermore, PETN, RDX and TNT have been also measured after the detonation process. Note that detonated explosives and mine gunpowder have been characterized for the first time in this thesis.

These measurements allow identifying several common explosives before or after a terrorist action and it can help in the counter terrorism fight.

I.4.-Scope of the thesis and survey of its contents

This dissertation is focused in developing THz technology and contributes to go a step forward in the application field.

The scope of the first section of the thesis is to implement a THz imaging system for the 0.090-0.500 THz band (Chapter II). The main remarkably difference of this imaging system is the operational bandwidth. Instead of taking images at only one frequency, the system can obtain THz images in a large bandwidth (Note that the system uses a network analyzer as emitter/detector of THz radiation).

This configuration provides a high dynamic range with a very low sensitivity. In addition, it allows to measure at the same time power and phase of the THz signal. It is important to stand out that this system is able to take images in transmission and reflection configuration.

This THz imaging system has been implemented to obtain THz images that they will be used in the next chapters. It has been designed in order to control all the parameters of the imaging acquisition process.

Nowadays, imaging systems are focused on the detection of unwanted objects because they are not able to identify the material of those items (identify using their electromagnetic parameters, such as refractive index or absorbance). As it has been mentioned, to complete material databases in this frequency range is an important issue. That is why some electromagnetic characterization systems in the THz range have been developed for this dissertation. These systems have been designed for laboratory applications and they will be described in Chapter III. They have been used to characterize several samples in the THz range. It is important to remark that some explosives before and (for the first time) after the detonation have been characterized.

Thus, a characterization system based on a network analyzer has been implemented. This system is able to measure in transmission and/or reflection configuration and also in frequency and time domain. Usually, it measures thick samples (electrical size). This system and its theoretical models are descripted in Chapter III.

Moreover, the polarization of the detected signal plays an important role in characterization systems. Ellipsometry systems are based on the

polarization angle to identify thin samples by its refractive index. A large description of this system is commented in Chapter III where the description of the null-ellipsometry system designed in this thesis is allocated. Note that as a reference system, TPS Spectra 3000 from Teraview was used. This system is a commercial THz-TDS spectrometer which works in the range 0.060-3.5 THz and measure in transmission/reflection configuration.

Both systems (THz-TDS and ellipsometry) use a laser source and therefore, they are compared. The refractive index of some non-detonated explosives has been obtained using both systems.

In order to show the images provided by the imaging system and some examples of the electromagnetic characterization systems (THz-TDS and ellipsometry), some applications of them are presented in Chapter IV.

Firstly, an electromagnetic characterization of several non-detonated explosives has been performed using THz-TDS and the ellipsometry system. For the first time, mine gunpowder has been characterized in the THz range. Furthermore, in order to extend the actual databases, some explosives after the detonation process have been measured.

Secondly, some examples in agriculture and food industries of the THz radiation are presented. In this case, THz systems demonstrate their capabilities to develop a water sensor or a quality control sensor in this frequency range.

Finally, for the purpose of showing the capabilities of the THz range to join the THz waves and the IR frequencies, a dual-band detector for a THz-IR system has been designed and manufactured in this dissertation. It is very important to remark that the joining of both frequency ranges in only one device provides new possibilities for imaging applications, where this device will be used as a front-end.

This device works in the submillimeter wave range and in the IR range. Note that two detectors are used, one for the submillimeter wave range, and the second for the IR range. The main remarkable characteristic of the device is that the submillimeter wave antenna also works as a lens for the IR range. This device will be presented in Chapter V.

The implemented characterization system for this dissertation have been demonstrate the capabilities of the THz radiation to detect and identify

unwanted or dangerous objects inside the sample under test, by the use of a non-invasive, non-destructive and non-ionizing radiation. Those techniques open new possibilities in agriculture, food industries or security and defense applications.

The characterization of the energetic materials or explosives is a very important topic for counterterrorist fight. This thesis has characterized explosives before and, for the first time, after the detonation. The obtained results provide new possibilities to security forces to fight against terrorist actions.

Finally, in this dissertation, a new dual-band device that works at THz frequencies and at IR range has been designed. This detector combines the measurements in the THz and the IR region at the same time. This allows to save measuring time and also to combines the imaging results at the same points from both domains.

CHAPTER II

IMPLEMENTATION AND DEFINITION OF PARAMETERS FOR AN IMAGING SYSTEM OPERATING IN THE 0.09-0.50 THz BAND

In this chapter, the implementation of an imaging system and the definition of its main parameters are presented. The imaging system measures samples by THz inspection and it is based on a network analyzer as emitter/detector. Furthermore, frequency and time domain methods in transmission/reflection configuration are discussed to show the capabilities of each method. Finally, some imaging results in the frequency range from 0.09 to 0.50 THz will be drawn.

II.1.- Introduction

An active imaging system, based on a commercial network analyzer has been implemented to provide THz images in transmission and/or reflection for the frequency range 0.060-0.5 THz for this thesis

This imaging system is based on electronic approach and it uses up converter mixers to reach the THz range from lower frequencies. The network analyzer provides a great dynamic range and a large bandwidth.

Thus, active images have been taken due to the use of an external source (Network Analyzer) to emit power that impinges on the sample. The transmitted and reflected powers are also detected by the network analyzer. It is important to remark that for each single frequency, an image is obtained.

For every pixel in the final image, a measure point has been recorded at each instant of time in all the frequency range by the network analyzer so a positioning system is used to move the sample.

The resolution of the imaging system has been improved by a quasioptical setup which collimates the THz beam. These three main parts of the imaging system (Network Analyzer, positioning system and quasioptical setup) will be descripted and commented.

This chapter is structured as follows. Section II lists the parameters taken into account to design and characterize the imaging system. Each sub-system of the global system is described in Section III. Section IV explains the method and the parameters measured with the Network Analyzer to obtain THz images while Section V summits the final characterization of the imaging system and Section VI presents several results obtained using the system. Finally, some conclusions about the use of the imaging system are commented in Section VII.

II.2.- Imaging Parameters

In order to implement an imaging system based on a network analyzer, some important parameters have been defined so that in this subsection, a short description of every one will be related.

II.2.1.- Spatial Resolution

It is defined as the ability of an imaging system to resolve detail in the object that is being imaged. This parameter is used as the capability of the system to differentiate two objects [Peiponen2013].

Abbe Diffraction Limit [Abbe1873] fixes the minimum resolution of the system. This limit, d, is calculated using the following equation

$$d = \frac{\lambda}{2(nsin\theta)} \tag{2.1}$$

Where λ is the wavelength at central frequency, n is the refractive index of the material where the electromagnetic wave is propagated and θ is the incident angle. For normal incident and propagation through the air, $d = {\lambda}/{2}$.

This diffraction limit was defined in 1873 and refined by Rayleigh in 1896. Thus, in a conventional far-field, imaging setup, the spatial resolution Δl is determined by the Rayleigh criterion:

$$\Delta l = 0.61 \frac{\lambda}{n \sin(\theta)} \tag{2.2}$$

Where λ is the wavelength of the light in vacuum, n the refractive index of the medium and θ half of the opening angle of the focused light beam. Note that $n\sin(\theta)$ is the numerical aperture, NA, of the focusing element which can be related with the focal length, f, and the diameter, D, of the focusing element as

$$n\sin(\theta) = NA \approx n\frac{D}{2f} \tag{2.3}$$

The resolution of the system has been measured in an experimental way, using two metal strips and varying the distance between them. The minimum distance between the strips that can be identified will be the minimum resolution of the system.

Note that this parameter will change as the frequency range changes. In Table 2.1, the resolution calculated for both definitions Abbe diffraction limit and Rayleigh criterion for each frequency range are related. Note that diffraction limit is calculated for propagation through the air and normal incident over the sample.

Table 2.1. Diffraction limit

Bandwidth *(THz)*	Wavelength *(mm)*	Abbe Diffraction Limit *(mm)*	Rayleigh Criterion *(mm)*
0.090-0.140	3.33-2.142	1.665-1.071	2.031-1.307
0.140-0.220	2.142-1.363	1.071-0.681	1.307-0.831
0.220-0.325	1.363-0.923	0.681-0.461	0.831-0.562
0.325-0.500	0.923-0.600	0.461-0.300	0.562-0.366

Typically, the measurements present in this chapter have been done in the range of 0.140-0.220 THz. The best achieved resolution in this range is good enough and less than one millimeter which allows obtaining a good quality imaging. This range has been used to obtain the images for the thesis. If an image is obtained in other range, it will be indicated.

II.2.2.- Sensitivity and Dynamic Range

Both sensitivity and dynamic range are internal parameters of the network analyzer and their vector network analyzer (VNA) extenders [OML] [VDI]. These devices will be described in Section II.3.1.

The sensitivity is the minimum signal that allows a proper operation of the system and it is fixed by the noise level. The dynamic range is defined as the ratio between the maximum and the minimum power at the detector [Sierra2003]. Usually they are expressed in decibels (dB). As the system is divided in some frequency ranges (due to the use of several VNA extenders to cover the bands) different dynamic ranges (and sensitivities) are obtained (Table 2.2). Note that the signal achieved in the detector is always higher than the sensitivity of the system.

Table 2.2. VNA Extenders

Freq. Range	Sensitivity	Dynamic Range		Manufacturer
(THz)	*(dB)*	*Min. (dB)*	*Typ. (dB)*	
0.090-0.140	-110	90	105	OML
0.140-0.220	-105	80	95	OML
0.220-0.325	-124	90	110	VDI
0.325-0.500	-127	80	110	VDI

The frequency range of 0.14-0.22 THz is the range with lower dynamic range and the worst sensitivity. It means that in this range, the power level achieved at the detector has to be higher than in other ranges to allow a good performance of the detection system.

II.2.3.- Imaging Time

This parameter is defined as the time necessary for taking an image. In the system used in the laboratory, it is related with time using for measuring a pixel of the image, and the movement time to map the entire sample (mapping time).

The pixel time is related with the bandwidth of the Intermediate Frequency Filter (IFF) and the sweep time (both of them are parameters of the network analyzer). The bandwidth has influence over the signal-to-noise ratio (SNR). If the bandwidth decreases, the SNR is higher but the pixel time increases. Sweep time is the time needed to measure the full bandwidth of the network analyzer and, as it is expected, if the bandwidth is smaller, the sweep time is lower.

The mapping time depends on the distance between two pixels of the image, the number of pixels and the speed of the positioning system. Usually, the distance between pixels has been fixed to 1mm for all the images and the number of pixel is determined by the size of the image. As the samples are not heavy sample, the speed of the scan system is maximum.

In this thesis, the imaging time parameter has not been taken into account. Instead of reducing the imaging time, the measurements have been done to cover the overall band (longer sweep time), with enough points in each image (related with the distance between pixels and the number of pixels) and low noise (narrow band intermediate frequency filter). Note that the speed movement is the same for all the images.

II.2.4.- Time Resolution and Time Length

These parameters appear in the time domain. Time resolution is the minimum time step obtained in the frequency-time domain transformation and it is limited by the bandwidth of the frequency signal in the network analyzer. Note that time resolution is inversely proportional to the bandwidth [Oppenheim1998] [Agilent]. Furthermore, time resolution defines the minimum distance that can be identified (time can be translated into distance using the speed of light).

Also, the time length is an important parameter. It depends on the number of points of the frequency signal and limits the depth distance. Normally, number-of-points parameter has been fixed to 201 frequency points. It means that the bandwidth is divided into 201 discrete points. In Table 2.3, time resolution and time length for 201 points are presented, for each frequency range.

Table 2.3. Time Resolution and Time Length

Bandwidth *(THz)*	Time Resolution *(ps)*	Time Length *(ns)*
0.090-0.140	40	8.0
0.140-0.220	25	5.0
0.220-0.325	19	3.8
0.325-0.500	11	2.2

II.3.- Imaging System Description

The imaging system is formed by three different parts. As emitter/detector, a network analyzer is used. Secondly, for mapping the sample, a three dimensional scanning system is utilized. Finally, a quasioptical system improves the resolution of the setup. A scheme of the imaging system is shown in Fig 2.1:

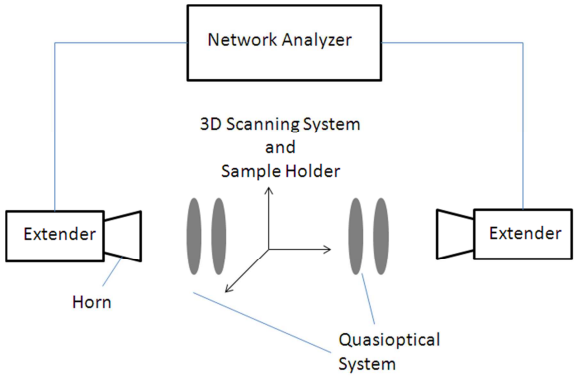

Fig. 2.1. Scheme of the measuring system

II.3.1.- Network Analyzer

Vector Network Analyzer (VNA) is used as emitter/detector and it provides power and phase detectors. Also, time domain operation is available using FFT algorithm within the VNA. As it has been commented, for operating from 0.090 THz to 0.500 THz, some external headers (VNA Extenders) are used. The pairs of VNA extenders and their bandwidth are related in Table 2.2. These VNA extenders allow to measure at higher frequencies and implement mixers and multipliers to obtain the operational frequency band (Section I.2.2.1). The operational frequency is obtained from a ramp function that it is mixed with the local oscillator signal and then, multiplied.

Two Network Analyzers have been used for the imaging system: the first one was an E8361C PNA Network Analyzer. Actually, the system is configured to use a N5242A PNAX. Both analyzers are provided by Agilent [Agilent].

The sample under test is placed in between the two VNA Extenders. With this configuration, reflection and transmission parameters through the sample can be measured. Some pictures of the network analyzer and VNA extenders are shown in Fig. 2.2.

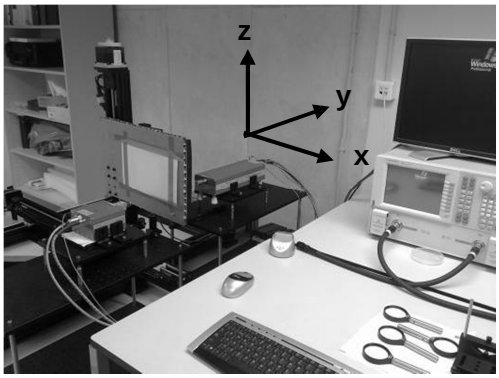

(a)

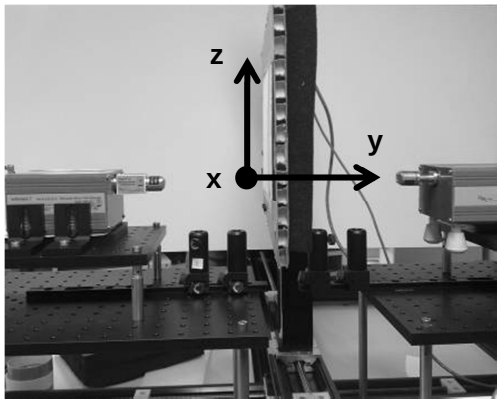

(b)

Fig. 2.2. (a) Photo of the measuring system and (b) detail of the sample place and the VNA extenders.

II.3.2.- 3D Scanning System

A 3D scanning system is used to move the sample and allows obtaining a THz image of the sample. This sample is placed in a vertical position as can be seen in Fig. 2.2. The 3D scanning system is moved in the xz plane (see Fig. 2.2a) with a minimum step of 6.25 μm, in order to map

the whole sample. The movement range is 700 x 500 x 500 mm. Each measurement point is corresponded with a pixel in the final THz image. The movement of the 3D scan and the data acquisition is governed by an in house LabView interface.

Note that the mechanical movement of the scanning system is a limiting factor for the imaging time. The speed of the axis movement can be adjusted in order to obtain more precision (low speed, 2 rev/s) or lower positioning time (high speed, 30 rev/s) [Velmex].

II.3.3.- Quasioptical Setup

The initial set-up uses two standard gain horn antennas in order to transmit and receive the THz signals, their directivity is presented in Table 2.4. This single far field configuration gives the possibility of using the same set-up for different frequency ranges. However, the achieved resolution is not sufficient. As it has been commented in Section II.2.1 diffraction limit for the frequency range of 0.14-0.22 THz is lower than 1mm while the resolution achieved with the horns is 7mm (Section II.5.1).

Table 2.4. Horn Directivity

Frequency Range *(THz)*	Directivity *(dB)*
0.090-0.140	24
0.140-0.220	24
0.220-0.325	25
0.325-0.500	25

Therefore, a quasioptical set-up based on lenses was designed in order to focus the beam [Bailey1998]. The proposal of quasioptical setup can be seen in Fig 2.3.

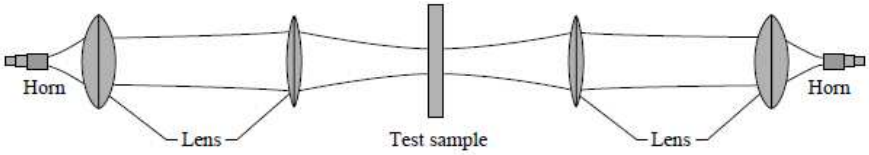

Fig. 2.3. Schematic of the proposal quasioptical system

To design the system, some parameters of a lens have to be taken into account, as Focal Length (F), distances from the beam waist to the lens (d_1 and d_2) and the beam waist diameter. (ω_1 and ω_2). They are shown in Fig. 2.4.

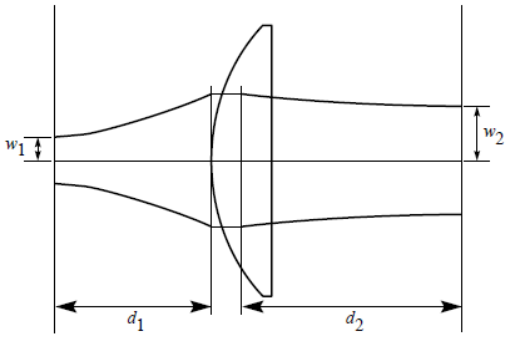

Fig. 2.4. Schematic of a plano-convex lens used in the quasioptical setup

The transformation of the Gaussian waist diameter, ω_1 through a lens is related by these equations

$$\omega_2^2 = \omega_1^2 \left[\frac{F_1^2}{(d_1 - F_1)^2 + \left({}^{\pi\omega_1^2}/_{\lambda} \right)^2} \right] \tag{2.4}$$

$$(d_2 - F_1) = (d_1 - F_1)\left[\frac{F_1^2}{(d_1 - F_1)^2 + \left(\pi\omega_1^2/\lambda\right)^2}\right] \tag{2.5}$$

These equations are developed for ideal thin lens. But they are also applicable if d_1 and d_2 were the distances from the beam waist to the principal plane of the thick lens. If the Gaussian beam is launched at the focal plane of a lens, ($d_1 = F_1$),

$$d_1 = d_2 = F_1 \tag{2.6}$$

$$\omega_2 = \frac{\lambda F_1}{\pi\omega_1} \tag{2.7}$$

These equations describe the parameters of the first lens. For the second lens, the beam waist diameter is calculated using this equation:

$$\omega_3 = \frac{\lambda F_2}{\pi\omega_2} \tag{2.8}$$

Finally, for a full design of the final quasioptical system (Fig. 2.5), the equations for the exit beam can be expressed as:

$$\frac{\omega_3}{\omega_2} = \frac{F_2}{F_1} \tag{2.9}$$

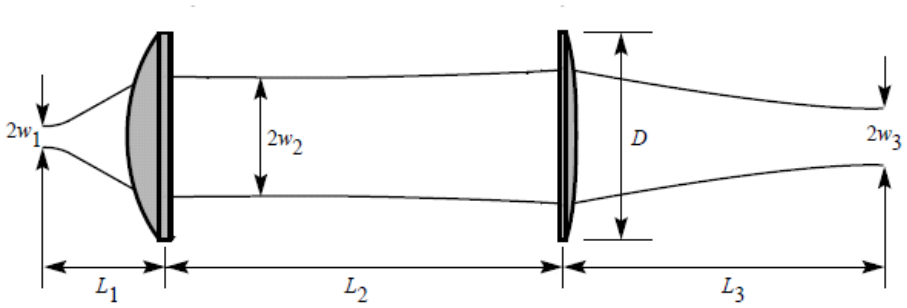

Fig. 2.5. Schematic of the quasioptical system

The lenses included in the imaging system were two pair of plano-convex lenses with F_1=50 mm [Zomega] and F_2=100mm [Thorlabs] focal length. Two lenses have been placed in between the emitter and the sample under test, and other two in between the sample and the receiver (Fig. 2.6).

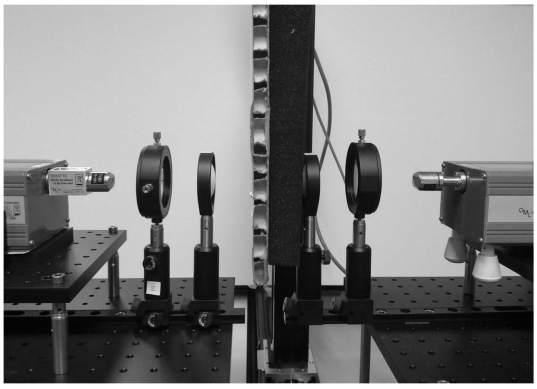

Fig. 2.6. Schematic of the quasioptical system

The calculated distance are L_1=48 mm, L_2=50 mm and L_3=47 mm. In order to simplify the system, all distances were fixed to 50 mm. Note that the optical system is symmetric and the same distances are used in both paths.

II.4.- Measuring Parameters

It is necessary to measure at the same time, both scattering parameters, S_{11} and S_{21}, in magnitude and phase, for reflections and transmission measurements respectively. A software has been specifically designed for this purpose and it controls the scan system and the network analyzer.

The measurement procedure is straight forward. The network analyzer emits an electromagnetic signal and this one impinges on the sample. Quantitative values of the overall transmitted and received power can be directly acquired. Furthermore, phase signal can also be recorded.

The fraction of the power that goes through the sample is called transmitted power (S_{21}). Typically, S_{21} parameter is measured in frequency domain. Transmission measurement provides information about the attenuation and absorption through the sample at each frequency. The measured data in the whole frequency range are post-processed to plot an image for each frequency.

The power that is reflected and goes back to the emitter is called reflected power (S_{11}). Firstly, a frequency measurement is done to achieve the S_{11} parameter. Secondly, a Fourier Transform is calculated to obtain a time domain representation which provides distance information from time-delay information. Furthermore, as it is firstly measured in frequency domain, S_{11} parameter can be represented as a function of the frequency. In this case, the obtained information is related with the refractive index (the level of the reflected power is related with changes in the refractive index as it will be explain in Section III.3.1) of the sample for each single frequency.

Note that transmitted power can also be represented in time domain if a Fourier Transform is calculated. As in the case of the S_{11} parameter, the obtained information will be related with the refractive index changes. On the other hand, this representation has been not very used in this thesis.

There is also another fraction of the power that is absorbed by the sample. This absorbed power can be calculated, using reflection and transmission measurements. (Section III.3.1)

II.4.1.- S_{21} Parameter in Frequency Domain

As it has been commented, in this case, the electromagnetic signal goes through the sample and provides information at the detector about transmittance at each frequency

The setup used in this configuration was more complicated than reflection one (it is descripted in the next subsection), due to the use of an T/R-VNA extender, a R-VNA extender and a full quasioptical system (four lenses), as can be seen in Fig. 2.7. Also, pointing problems can appear using this technique, as two VNA extenders have to be aligned.

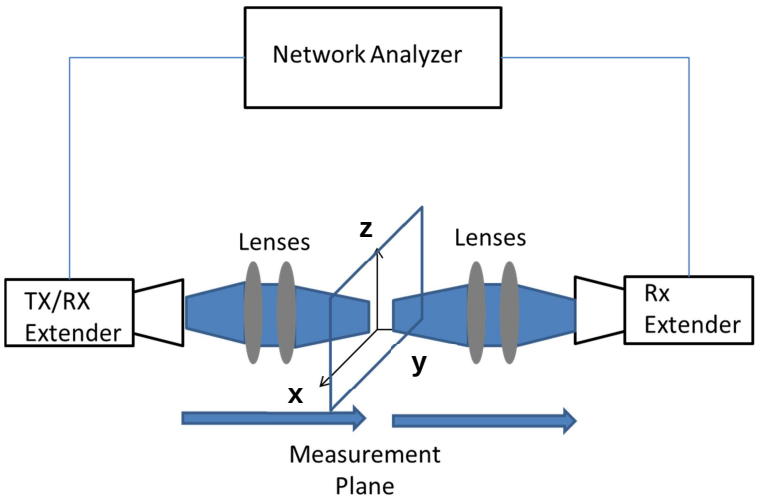

Fig. 2.7. Schematic of the measuring of S_{21} parameter

By representing for each XZ position either the amplitude or the phase of the electromagnetic wave, an image can be drawn.

This “transmission image” is obtained for one single frequency. During the measurement process, a full frequency range is measured. It has been divided into single frequency points using an internal parameter of the network analyzer, the number of points. Every point can be translated in one frequency and a transmission image (this parameter has been commented in Section II.2.4) for each frequency is obtained during the measurement.

The time required to obtain these images is large for a practical application. However, it allows obtaining high resolution images in a broad bandwidth. The study for the overall frequency range allows characterizing the performance of the sample at each single frequency.

Note that the measured values have been normalized in transmission using the transmission response without the sample in order to eliminate the influence of the reflections of the lenses and associated standing waves. Some images obtained with this technique are presented in Fig 2.8.

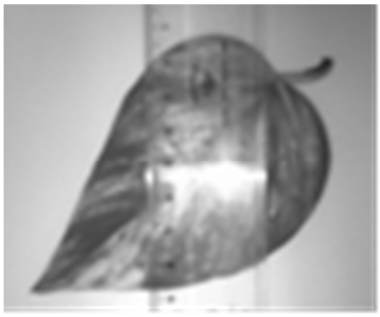

(a) Photo of the leaf

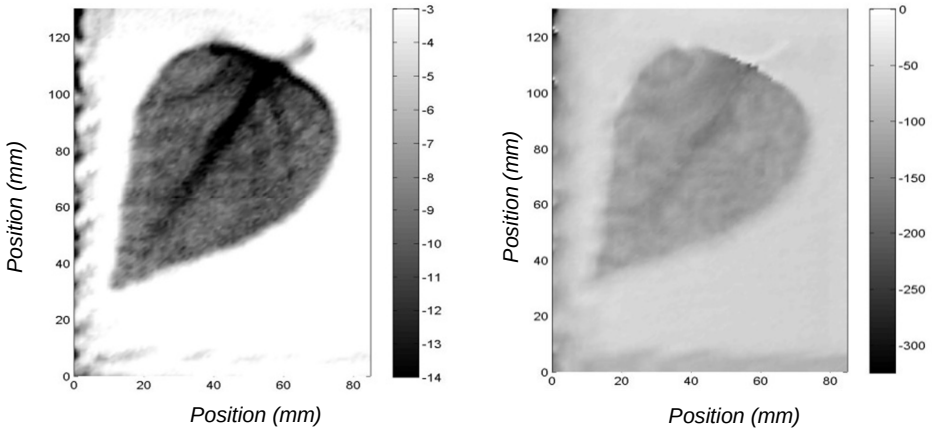

(b) Magnitude (dB) *(c) Phase (Degrees)*

Fig. 2.8. Images of the S_{21} parameter and the photo of a leaf under test

II.4.2.- S_{11} Parameter in Time Domain

In this measurement setup, reflected power was used to obtain time delay information from the sample (note that reflections inside the sample are produced due to the changes in the refractive index. Also, time distance between the reflected peaks can be translated into path distance using the speed of light). As it can be seen on Fig. 2.9, this configuration only uses an extender header and a pair of lenses. That is very important in the development of a final measuring system because it will be smaller, cheaper (only a T/R module is used) and easier to use (precision alignment is not necessary) than a transmission system.

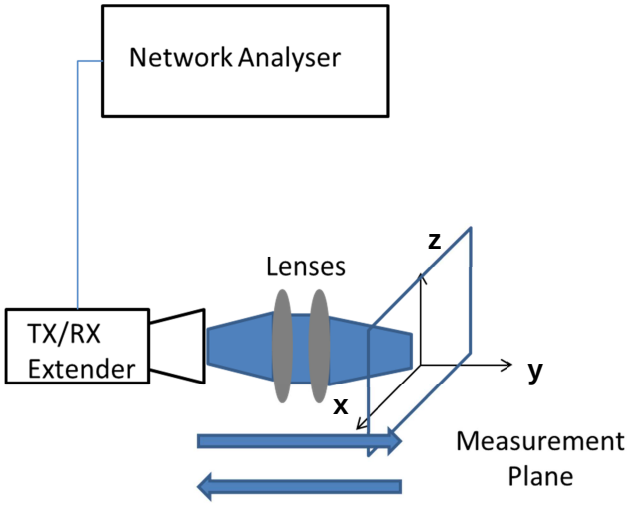

Fig. 2.9. Schematic of the measuring of S_{11} parameter

Note that for measuring in time domain, a frequency measurement is done. Once the information in magnitude and phase has been recorded, a Fast Fourier Transform (FFT) algorithm is used. In this calculation, the most important parameter is the frequency bandwidth, which fixes the time resolution. Also, the number of points of the VNA has influence in this representation, as it is proportional to the time length (Section II.2.4). Usually, a gating is used to eliminate the secondary reflections or the influence of the standing waves generated by the lenses.

With this configuration, an image in time domain is obtained. Normally, the main peak observed is related with the first reflection over the sample, as it can be seen in Fig. 2.10. It has the highest level, as the reflection over the sample (a leaf) is the main reflection. Second and third peaks are related with multipath signals (backs side of the sample for instance or resonations inside the sample itself). Note that the time delay between peaks is directly related with depth information.

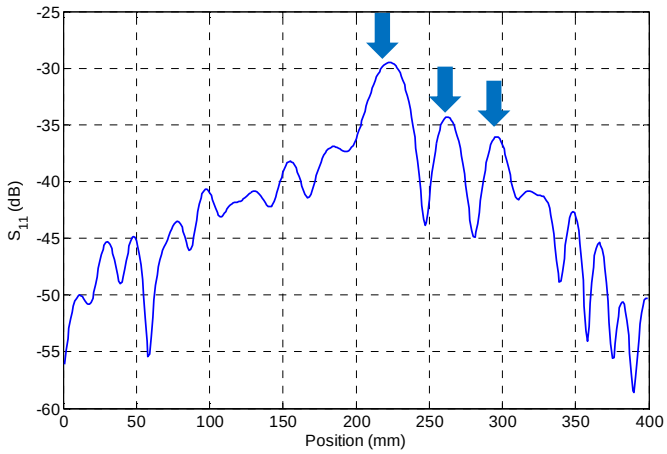

Fig. 2.10. Measurement in time domain of the S_{11} parameter of the leaf presented in Fig 2.11. Note that standing waves have been eliminated due to the normalization.

As it is depicted on Fig. 2.10; a typical trace of S_{11} parameter of a leaf in time domain has been recorded. Delay time between peaks is measured in nanoseconds and using the wavelength into the material, the distance (D) between peaks can be obtained.

$$D = \lambda f(TD) \tag{2.10}$$

Where λf is the speed of the electromagnetic wave inside the material and *TD* (time delay) is the time distance between two peaks. Furthermore, S_{11} magnitude variation gives information about refractive index (permittivity or refractive index using Fresnel coefficients. This characterization will be

further explained in Chapter III), while time delay provides information about depth (thickness of the sample). Images at different instants of time are translated into cuts of the sample under test. The combination of these cuts can be used to plot a 3D image of the sample.

Several cuts of the previous leaf can be seen in Fig 2.11. The leaf cannot be distinguished in Fig. 2.11a because it represents a cut in the foreground of a position where the leaf is placed (the control point, rounded with a red circle presents a level of -13.4 dB). On the other hand, Fig. 2.11b to Fig. 2.11e show cuts of the leaf (control point level is (b) -9.7 dB; (c) -7.1 dB; (d) -6.5 dB and (e) -8 dB). Finally in Fig. 2.11f the leaf has disappeared because it shows a cut behind the leaf (-11.5 dB).

Note that the normalization in this case was different from the case of a transmission image. In this case, a metal plane was used to obtain a maximum of reflected power. This value was used as the maximum value to normalize the measurement. The metal plane was placed in the same point that the sample was placed.

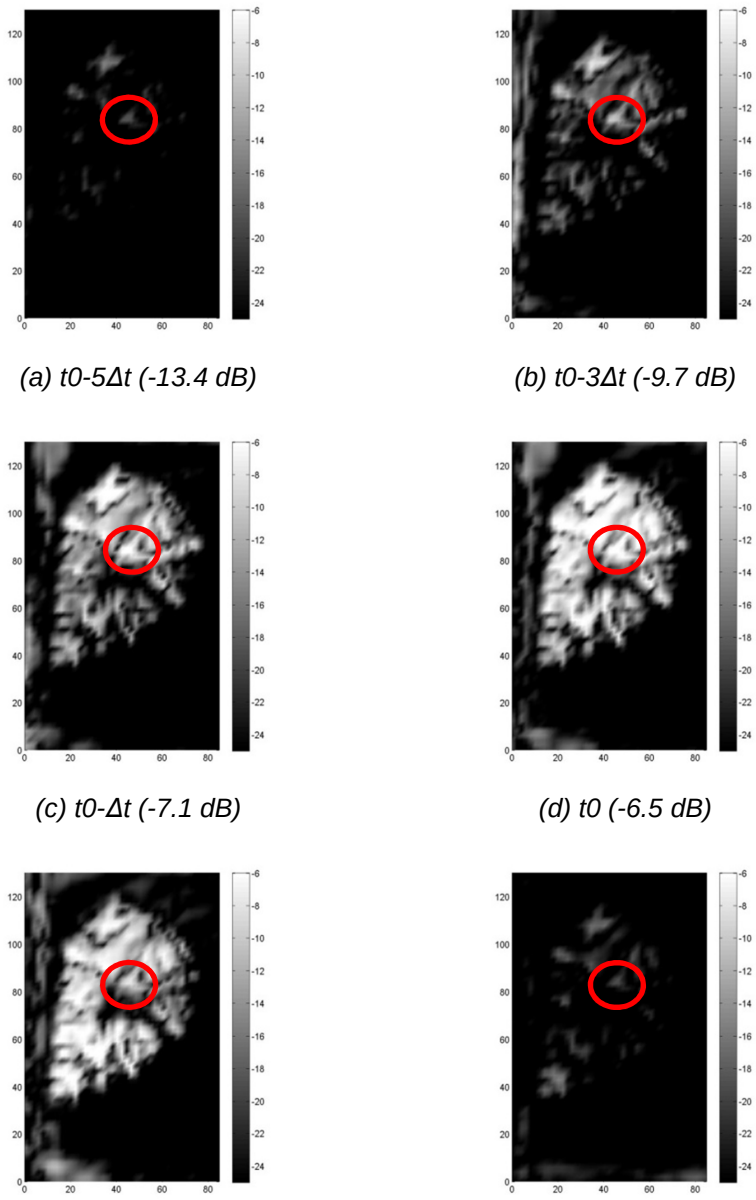

(a) t0-5Δt (-13.4 dB) *(b) t0-3Δt (-9.7 dB)*

(c) t0-Δt (-7.1 dB) *(d) t0 (-6.5 dB)*

(e) t0+Δt (-8 dB) *(f) t0+3Δt (-11.5 dB)*

Fig. 2.11.-Several cuts of the leaf measured in time domain. In parenthesis, the level of the control point, marked with a red circle.

II.4.3.- S_{11} Parameter in Frequency Domain

The measurement setup presented in Fig. 2.9 measures in frequency domain. Thus, the obtained results can be presented as a function of the frequency. The achieved measurement contains information about the reflected power, at each frequency, in the overall bandwidth.

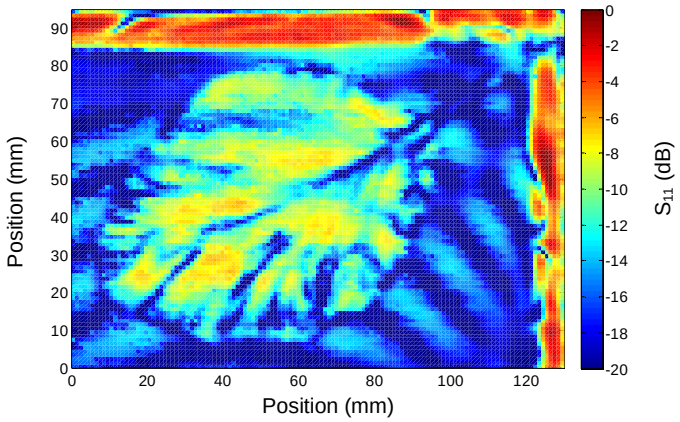

Fig. 2.12. Image in frequency domain of the S_{11} parameter using the setup depicted in Fig. 2.9.

In Fig 2.12 it is possible to identify a leaf. Note that the red area in the border is the holder of the sample. In this case, the area without sample is presented as a minimum in the image (blue areas with a reflected power level around -18 dB). On the other hand, the sample presents a higher reflection level (-8 dB) as the refractive index of the sample is different from the refractive index of the air.

As in the previous case, a metal plane is used to obtain a maximum in the reflected power to normalize the signal.

II.5.- Characterization of the imaging system

The imaging system will obtain the transmission/reflection properties of the sample between 0.09 THz and 0.5 THz. Even though the highest operational frequency gives the best resolution, f=0.2 THz was used (Section II.2.2). At this frequency, the VNA presents a dynamic range of 95 dB with a resolution following the Rayleigh criterion around 1 mm. Note that this frequency range has been selected because it provides a good resolution and presents the worst dynamic range (As it is the worst case, the system can measure in other frequency ranges without problems).

II.5.1.- Resolution

The resolution of the system was measured experimentally using a metal strips pattern (Fig. 2.13). The size of these metal strips was increased gradually until they could be clearly distinguished in the S_{21} parameter.

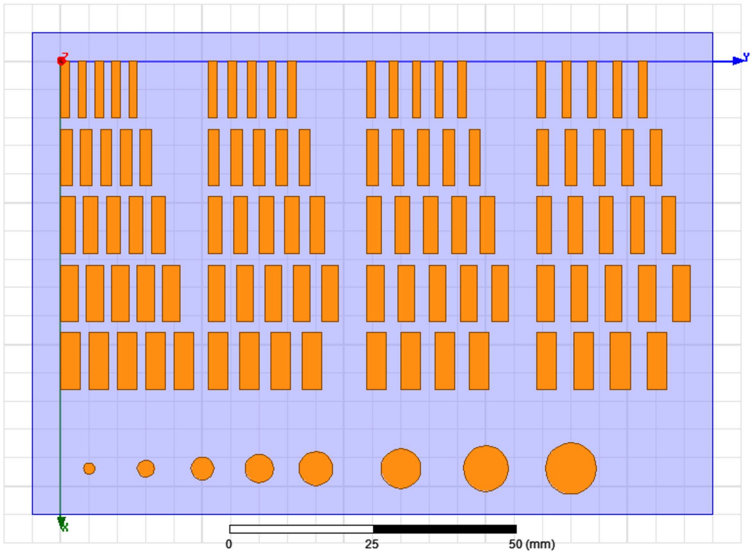

Fig. 2.13. Resolution metal strip pattern

In a first approach, using the horns only, the smallest size found, which fixes the resolution of the system, was of 7 mm. It means that the achieved resolution is far away from the theoretical diffraction limit obtained

in Section II.2.1. Taking into account this result, the quasioptical setup was designed and introduced into the system. Using the quasioptical setup, described in Section II.3.3, the achieved resolution is of 2 mm, at 0.2 THz. (see Fig. 2.14).

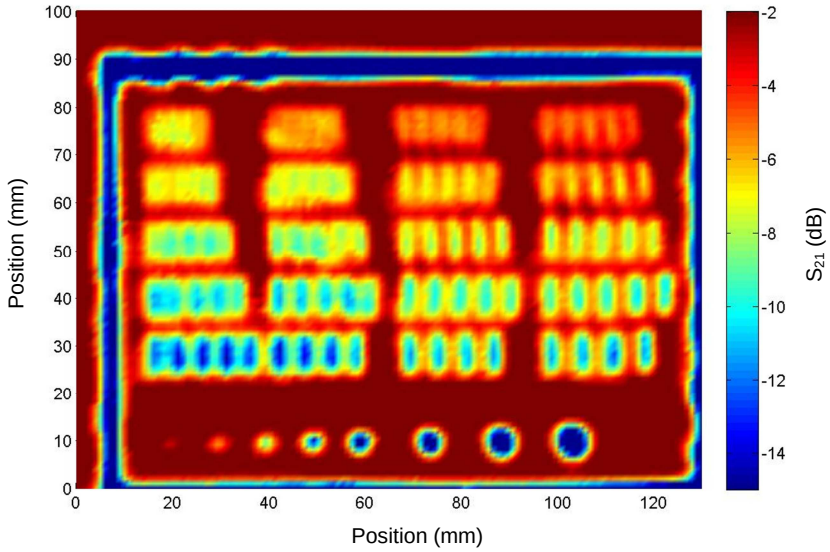

Fig. 2.14. Transmission measurement of the resolution metallic pattern

Theoretical resolution of the imaging system, (diameter of the focusing element is 50 mm, focal length, 50 mm) is about 1.5 mm, according to the Rayleigh criterion (Eq. (2.2)). Taken into account both values, it can be concluded that the experimental resolution achieved is a good result.

Note that the resolution is also higher than the Abbe diffraction limit (about 1 mm in the frequency range of 0.140-0.220 THz which is shown in Table 2.1) as it was expected.

II.5.2.- Defect Detection

Defect detection is the capability of the system of identifying one object by its size (related with the resolution of the imaging system) or by its material (related with the dynamic range and the sensitivity of the system). Note that the material of the object is related with the electromagnetic parameters (refractive index or permittivity) of the sample.

In a first step, in order to measure the defect detection capability based on the size, small metal squares from 2 mm to 7 mm side edge were placed on the surface of a leaf (Fig.2.15). A THz active image was taken using the imaging system at 0.2 THz. Squares from 3 mm to 7 mm side edge can be clearly distinguished and the smallest square (2 mm side edge) can be identified with enough precision.

It is possible to conclude that the system is able to detect metal pieces of 2x2 mm^2. This result agrees with the resolution of the system, which is 2 mm.

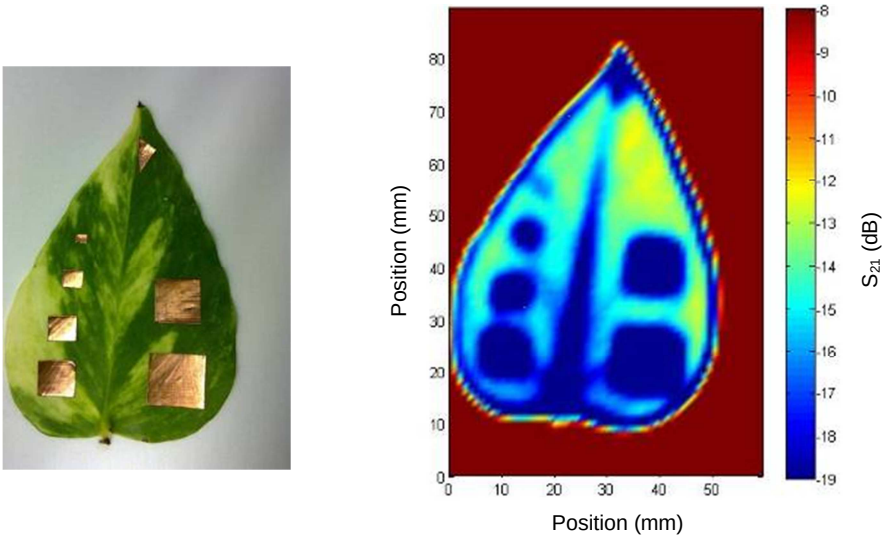

(a) *(b)*

Fig. 2.15. (a) Image in visible spectrum of the leaf with the metal squares and (b) THz active image of the same leaf.

Secondly, to measure the defect detection capability based on the type of the defect, a slice of absorbent, a hole in one of the leaves and a metal square were placed in a leaf as it can be seen in Fig. 2.16a. Furthermore, some leaves were partially superposed to check the impact of the superposition in the power levels measured in the THz image.

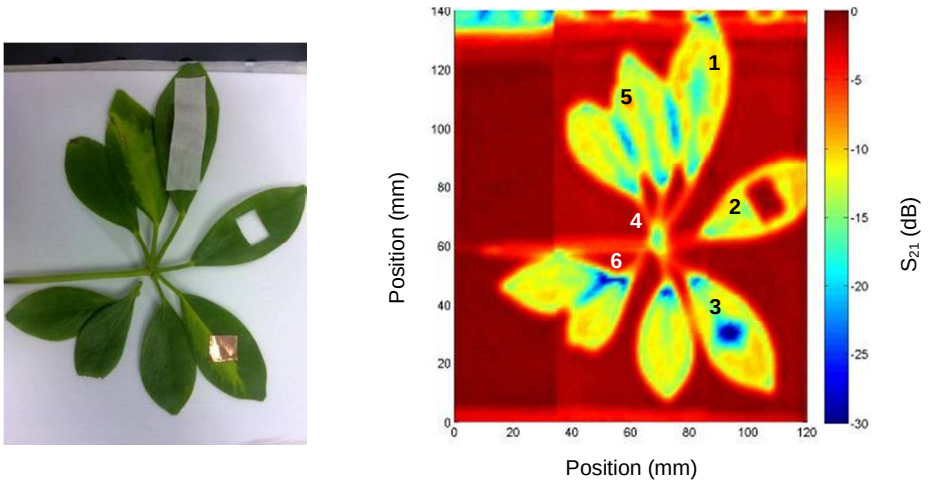

(a) *(b)*

Fig. 2.16. (a) Leaf in visible spectrum with some defects: hole, metal square and a slide of absorbent and (b) THz image of the same leaf.

The image taken is shown on Fig. 2.16b. The system can detect level differences between the absorbent (number 1), the hole (number 2) and the metal (number 3). The hole in the leave appears like a maximum in the transmitted parameter (-3dB), while the metal square has a minimum in the power level (-27dB). Finally, the slice of absorbent (this material could represent an unwanted object in the sample) presents a different absorption level (-14dB), but it cannot be identified in between the leaf. Its level is very similar to the level of the leaf.

These differences in the level of detected power allow distinguishing between two different objects. Note that in transmission configuration, the metal parts appear as a lower in the detected power (blue color) while in

reflection, the metal object is represented by a maximum value in power level as it reflects the THz power.

Furthermore, the leaf stack (number 4) and the veins (number 5) are detected on Fig. 2.16 and they present a level of -14 dB (green color) due to the fact that they have a higher level of water, which is translated in a higher absorption in the THz image. Also, it is possible to distinguish (blue color) the superposition of the leaves (number 6 with a level of -24 dB), which provides the possibility of controlling the number of slices or the thickness in a quality system.

II.6.- Imaging Results

This set of images corresponds with a measurement of a leaf in the 0.140-0.22 THz frequency band. First images were taken with no quasioptical setup to test the resolution obtained just with the VNA extenders and horns.

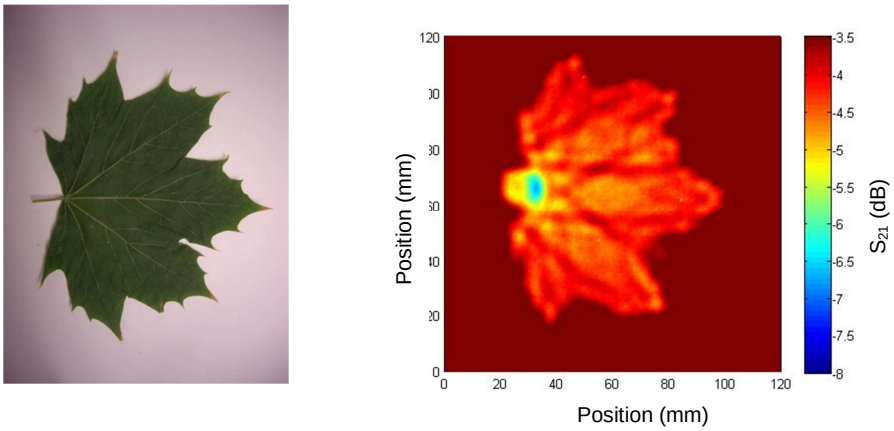

(a) *(b)*

Fig. 2.17. (a) Photo of the leaf under test and (b) first THz transmission image obtained for this thesis.

In Fig 2.17, the leaf is clearly distinguished but the resolution is very poor. The main parts of the leaf can be identified, as the leaf stack and some principal veins but the resolution achieved with this system (7 mm) is not enough to obtain a clear image.

Due to the poor results obtained, the quasioptical system was designed and implemented. A sample made with two different parts of leaves was measured as it is plotted in Fig 2.18. The lower part of the sample is a fresh leaf (the borders of the leaf are green, number 1) and the upper part of the sample is a dry leaf (with the borders in a darker color, number 2). Fig. 2.18b shows the different level of transmission power that can be obtained with the imaging system. Note that the resolution of the image has been increased using the quasioptical system, because of it is possible to identify the veins, leaf stack and small ends of the leaf.

Also, in this image, the dynamic range of the system has been tested. As it is depicted, dry leaf provides high signal level at the detector (orange color, -5.2 dB in point 2) and the fresh part provides lower levels (blue color, -7.3 dB in point 1). Due to the different water content of the two parts, it is possible to conclude that the dynamic range and the sensitivity of the system in this frequency range are enough for this application (note that the signal achieved is higher than the sensitivity of the system).

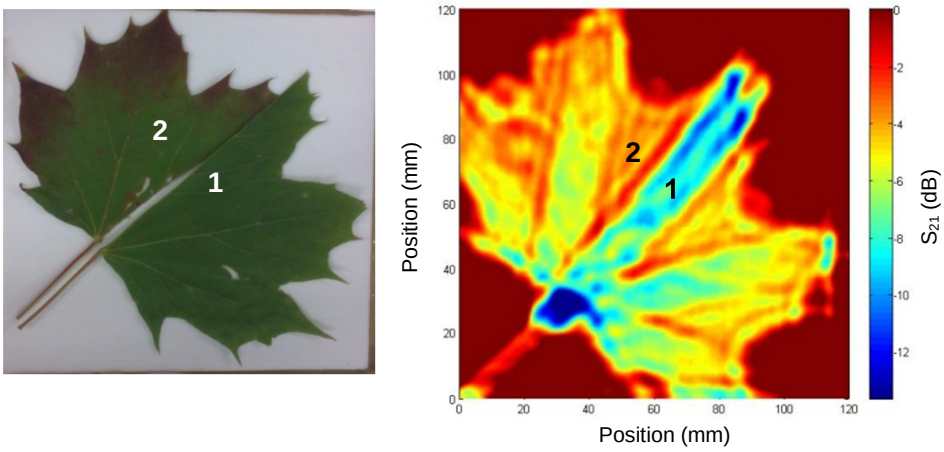

(a) *(b)*

Fig. 2.18. (a) Visible image and (b) THz transmission image for test the different levels of water content

As the resolution has been increased, a measurement of the capability to defect detection of the system was done. To reproduce a real case, an insect was used. It was placed in the leaf and all the sample (insect and leaf) was placed into a CD box. Fig 2.19 shows the image obtained, measuring S_{21} parameter. There is a zone with low transmission level near to leaf stack (it is colored in blue and presents a level of -12 dB). Taking into account other leaves' images, it is possible to say that there is a foreign body on the leaf. Note that, due to the small size of the parts of the insect, it cannot be identified as insect, but detected.

Also, it is remarkable that this result agrees with parameters of the system. The resolution achieved (2 mm) is enough to detect the insect, as it is demonstrated in Fig. 2.19. Furthermore, the dynamic range of the system allows measuring differences in the transmitted power level (four times lower). In conclusion, it is possible to detect an unwanted object with high water content, due to the low level of transmitted power. On the other hand, it is not possible to recognize it as an insect.

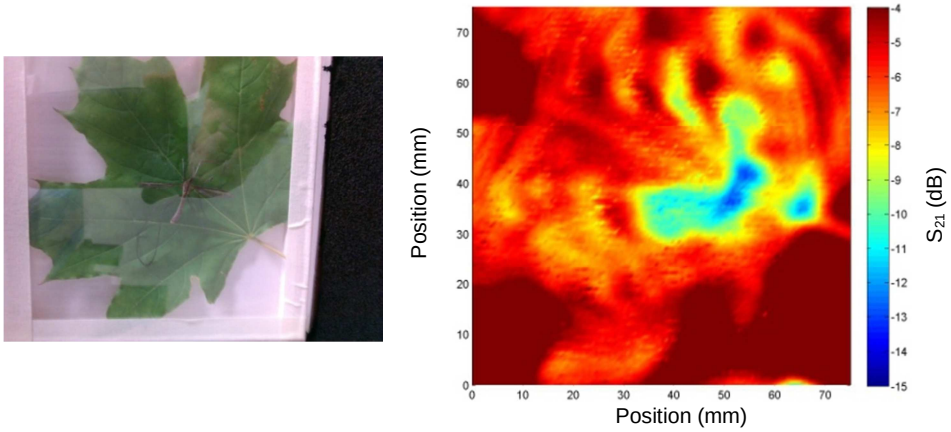

(a) *(b)*

Fig. 2.19. (a) Visible image and (b)THz image of a leaf with an insect

II.7.- Conclusions

In this chapter, the implementation of a sub-millimeter wave imaging system based on a network analyzer has been descripted. It provides the capability of measuring the magnitude and/or the phase of the achieved signal, in transmission or reflection configuration, using frequency or time domain.

The parameters taking into account for the implementation of the imaging system (spatial resolution, sensitivity, dynamic range, imaging time, time resolution and time length) have been defined and determined.

This system is able to detect unwanted objects in the obtained THz image (maximum size of 500 x 700 mm) for the 0.090 THz to 0.500 THz frequency band. Note that the frequency range is divided due to the characteristics of the network analyzer (0.090-0.140 THz; 0.140-0.220 THz; 0.220-0.330 THz; 0.330-0.500 THz). The typical dynamic range for the overall bandwidth is, at least, 95 dB and the sensitivity of the system is better than -105 dB.

The resolution achieved has been improved due to the implementation of a quasioptical system (from 7mm to 2mm at 0.200 THz) which uses PTFE lenses to focus the THz beam. This system has been optimized by Gaussian beam theory.

Some transmission images have been presented to show the capabilities of the system. These images have been obtained at 0.2 THz, which provides a resolution of 1 mm (Rayleigh criterion), with the worst sensitivity (-105 dB) and the minor dynamic range (95 dB). In these conditions, the system provides a good quality images for the thesis.

CHAPTER III

THz ELECTROMAGNETIC CHARACTERIZATION SYSTEMS

In this chapter, several electromagnetic characterization systems for the THz range are presented. Also, the theoretical models and the parameters using for the characterization are explained. To illustrate them, some examples of possible applications for these characterization systems are related.

III.1.- Introduction

Imaging systems have been demonstrated that they are able to detect an unwanted object using THz images. On the other hand, the materials of the sample are not identifying by them. Due to this consideration, several electromagnetic characterization systems were implemented for this thesis.

These systems allow identifying and differentiating samples in an imaging system (such as the system descripted in Chapter II), through the measurement of the electromagnetic parameters (refractive index, absorbance or permittivity). Note that, as a function of the thickness (electrical size) of the sample, the most appropriate system will be used for the characterization.

The first characterization system is based on a vector network analyzer, able to measure scattering parameters in time/frequency domain and in transmission/ reflection mode. With these parameters, it is possible to obtain the refractive index of the sample under test. Due to the use of the VNA (Chapter II), this system provides a very good dynamic range for the 0.09 – 0.50 THz frequency band. This system characterizes thick samples based on the theoretical model for one single interface.

The second system is a TPS Spectra 3000 from Teraview. It is based on a laser source and it is a THz-TDS in transmission and reflection configuration from 0.060 THz to 3.5 THz. This system characterizes a sample by its refractive index, permittivity and absorbance. TPS Spectra 3000 is used for thin samples based on the theoretical model for thin samples with two interfaces. Note that those samples can be formed by only one material, powder samples or liquid samples.

Finally, an ellipsometry system was developed. This system uses the TPS Spectra 3000 as a source and it characterizes samples by its refractive index. This system is based on the theoretical model for a null-ellipsometer and it is able to measure thick and thin samples.

This chapter is structured as follows. After the introduction, the electromagnetic parameters used for the characterization are listed in Section II. Section III presents theoretical models followed for the description of all the characterization systems, which are explained in Section IV. Section V shows some examples of these electromagnetic characterization systems through the measurements of some explosives

(before and after the detonation) by THz-TDS and by null-ellipsometry. Furthermore, a comparison between the THz-TDS system and the ellipsometry system is performed in this section. Finally, some conclusions about these systems are commented in Section VI.

III.2.- Parameters used in electromagnetic characterization

In this section, several electromagnetic parameters are descripted. These parameters will be used for the electromagnetic characterization of the materials in following sections.

III.2.1.- Permittivity

Permittivity is a property which is associated with how much electrical charge a material can store in a given volume [Balanis1989].

The permittivity in vacuum (free space) is denoted as ε_0 and its value is 8.85418782E-12 F/m. This parameter is obtained from the ratio D/E in vacuum, where D is the electric displacement field and E is the electric field. Note that no material has a permittivity lower than the permittivity of the vacuum.

The permittivity of any material is referred by its relative permittivity (also named as dielectric constant), and it is denoted as ε_r. This relative permittivity is obtained from:

$$\varepsilon = \varepsilon_r \varepsilon_0 = (1 + \chi)\varepsilon_0 \tag{3.1}$$

where ε is the permittivity of the material and χ is the electric susceptibility of the material.

Note that ε is a complex number and usually it is expressed as:

$$\varepsilon = \varepsilon_1 + j\varepsilon_2 = \varepsilon' + j\varepsilon'' \tag{3.2}$$

III.2.2.- Refractive index

This parameter is defined as the ratio between the light speed in the vacuum and the light speed in the medium [Tomp2005]. Thus, for each material is always higher than 1 (in the case of the vacuum, its value is 1).

As in the previous case, the refractive index is a complex number, typically expressed as:

$$N = n + jk \tag{3.3}$$

Where n is related with the phase speed and k indicates the amount of absorption loss when the electromagnetic wave propagates through the material.

III.2.3.- Absorption coefficient

This coefficient describes the fractional decrease in intensity with distance [Wooten1972]. The measured intensity of transmitted I through a layer of material with thickness L is related to the incident intensity I_0 according to the inverse exponential power law that is usually referred to as Beer–Lambert law [Beer1852]:

$$I = I_0 e^{-\alpha L} \tag{3.4}$$

Where L denotes the path length. The attenuation coefficient (or absorption coefficient) is α.

III.2.4.- Absorbance

Absorbance is a quantitative measure expressed as a logarithmic ratio between the radiation falling upon a material and the radiation transmitted through a material [Mehta2012].

$$A_\lambda = -log_{10}\left(\frac{I_1}{I_0}\right) \tag{3.5}$$

Where $A_\lambda$is the absorbance at a certain wavelength of light (λ), I_1 is the intensity of the radiation (light) that has passed through the material (transmitted radiation), and I_0 is the intensity of the radiation before it passes through the material (incident radiation).

III.3.- Theoretical Models used in electromagnetic characterization

III.3.1.- One single interface: thick samples

First theoretical model describes an interface between two different mediums, named by their refractive indexes, n_1 and n_2. This interface is characterized by the transmitted and reflected rays, as it is depicted in Fig. 3.1.

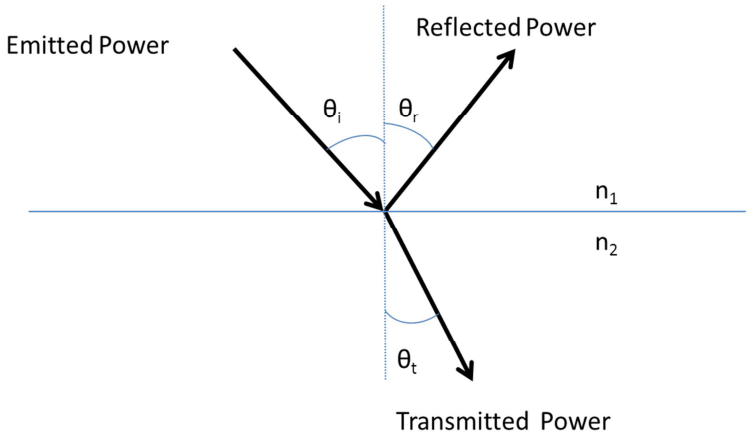

Fig. 3.1. Scheme of model for one interface

Fresnel Coefficients relate the emitted power (P_i), (which is the incident power over the interface) with transmitted (P_T) and reflected power (P_R). Also, absorbed power (P_A) can be calculated. Fresnel Coefficients are expressed by the following equations,

$$r = \frac{n_1 \cos\theta_i - n_2 \cos\theta_t}{n_1 \cos\theta_i + n_2 \cos\theta_t} \tag{3.6}$$

$$t = \frac{2n_1 \cos\theta_i}{n_1 \cos\theta_i + n_2 \cos\theta_t} \tag{3.7}$$

Thus, transmitted and reflected power can be expressed as:

$$P_R = r * P_I \quad P_T = t * P_I \tag{3.8}$$

$$P_I = P_R + P_T + P_A \tag{3.9}$$

Note that only reflected ray and incident angle are taken into account to characterize the medium. Also, the polarization of the incident ray has been supposed to be perpendicular to the incident plane. Using Fresnel Coefficients it is possible to obtain Snell law,

$$\frac{\sin\theta_i}{\sin\theta_t} = \frac{n_2}{n_1} \tag{3.10}$$

This model has been used for one single interface. Normally, the sample under test is so large (electrical size) for measuring the transmitted ray (the transmitted power that arrives to the detector has been attenuated due to the propagation distance through the sample) those only reflection parameters can be obtained. Taking into account Eq. (3.6); the reflected ray is related with the refractive index of the sample.

Some applications of this theoretical model are the characterization of thick samples (where the losses are very high. Those losses are due to thickness, the absorption of the sample or a combination of both of them)

III.3.2.- Thin sample with two interfaces

The model described in previous section is very simple and only valid for samples with one interface (thick samples). If the thickness of the sample is comparable to the wavelength at working frequency, a more detailed model is needed.

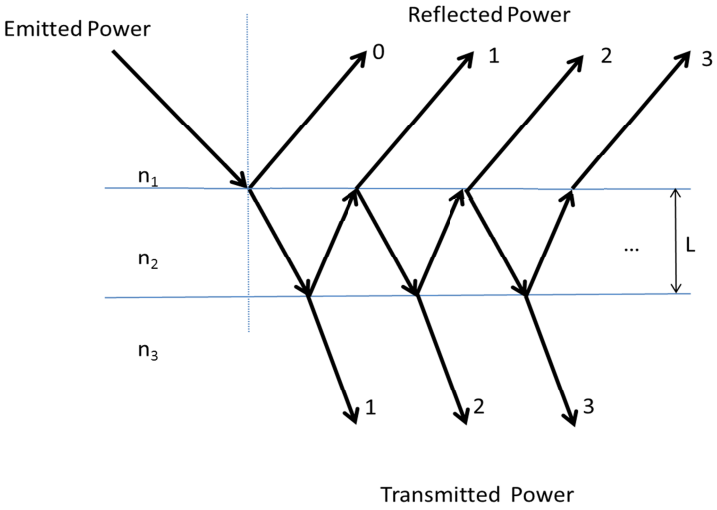

Fig. 3.2. Scheme of a thin sample with two interfaces

This model describes the interface between three media (n_1, n_2, n_3) as it can be seen in Fig. 3.2. Second medium models the sample under test and it has been descripted as a Fabry-Perot resonator. Usually, media n_1 and n_3 represents the air around the sample.

In this case, the first ray is partially reflected (reflected power, ray 0) and partially transmitted to the medium n_2. Once it is inside the medium, a resonance behavior is obtained. Several rays can be found inside sample medium (n_2), as they are reflected in both interfaces. The electromagnetic wave is reflected and transmitted successively each time it arrives to one interface. Note that R0 (ray 0) models the first reflection over the interface n_1-n_2. This reflection can be characterized using the model described before (Section III.3.1).

Multiple transmitted and reflected rays which appear due to the resonator [Duvillarret1996] are described as follows (Table 3.1).

Table 3.1.- Equations of the transmitted and reflected rays

	Transmitted	Reflected
1	$E_i t_{12} t_{23} e^{-\alpha L}$	$E_i t_{12} r_{23} t_{21} e^{-2\alpha L}$
2	$E_i t_{12} r_{23} r_{21} t_{23} e^{-3\alpha L}$	$E_i t_{12} (r_{23})^2 r_{21}\ t_{21} e^{-4\alpha L}$
3	$E_i t_{12}\ (r_{23} r_{21})^2 t_{23} e^{-5\alpha L}$	$E_i t_{12} (r_{23})^3 (r_{21})^2 t_{21} e^{-6\alpha L}$
4	$E_i t_{12}\ (r_{23} r_{21})^3 t_{23} e^{-7\alpha L}$	$E_i t_{12} (r_{23})^4 (r_{21})^3 t_{21} e^{-8\alpha L}$
	…	
N	$E_i t_{12}\ (r_{23} r_{21})^{n-1} t_{23} e^{-(2n-1)\alpha L}$	$E_i t_{12} (r_{23})^n (r_{21})^{n-1} t_{21} e^{-2n\alpha L}$

Where $e^{-\alpha L}$ is the propagation term through the second medium and L is the thickness of the sample medium. As it can be seen, there are two coefficients that appear in the equations; t_{ij} is the transmission Fresnel coefficient from the medium i to the medium j; r_{ij} is the reflection Fresnel coefficient from the medium i to the medium j. Finally, E_i is the incident electric field over the sample. These coefficients are calculated using:

$$t_{ij} = \frac{2n_i}{n_i + n_j} \tag{3.11}$$

$$r_{ij} = \frac{n_j - n_i}{n_j + n_i} \tag{3.12}$$

Note that the ray has a normal incident. Coefficients descripted in Eq. (3.11) and Eq. (3.12) are the Fresnel Coefficients calculated using Eq. (3.6) and Eq. (3.7) when $\theta_i = \theta_t = 0°$.

According to the equations for the resonance medium, reflection (R) and Transmission (T) parameters, which relate the incident power with the total reflected/transmitted power, can be described as:

$$R = t_{12}r_{23}t_{21}e^{-2\alpha L}\frac{1}{1-e^{-2\alpha L}r_{23}r_{21}} \tag{3.13}$$

$$T = t_{12}t_{23}e^{-\alpha L}\frac{1}{1-e^{-2\alpha L}r_{23}r_{21}} \tag{3.14}$$

These parameters include all the reflected/transmitted rays and have been calculated as a geometrical series. Both parameters, R and T, are used to calculate the reflected and transmitted field. Furthermore, it is possible to calculate the complex refractive index and the permittivity of the sample, so that software functions have been implemented to calculate the electromagnetic parameters for the different models. This software uses transmitted power and phase in order to characterize the sample.

If the incident electric field is known and (n_1, n_3) model the air around the sample, the refractive index of the second medium, which summarizes the electromagnetic parameters of the sample, can be calculated using the following equations.

$$n = \sqrt{\frac{\sqrt{(\varepsilon')^2 + (\varepsilon'')^2} + \varepsilon'}{2}} \tag{3.15}$$

$$k = \sqrt{\frac{\sqrt{(\varepsilon')^2 + (\varepsilon'')^2} - \varepsilon'}{2}} \tag{3.16}$$

Note that Eq. (3.15) and Eq. (3.16) are used in Eq. (3.3) to calculate the complex refractive index. It is important to remark that the model descripted in previous section is an approximation of this model. The reflected ray number 0 (R0) can be descripted as $R0=E_i r_{12}$ which is the reflected ray calculated using Eq. (3.6) (for the case of normal incident).

III.3.2.1.- Powder samples

Theoretical model for thin samples is very useful for small solid samples with a thickness comparable to the wavelength. These samples can be simply samples (only composed by one material), powder samples or liquid samples. For characterizing powder samples, another parameter, (effective permittivity of the sample) has to be taken into account because these samples are measured in combination with other materials used as base for the powder sample. Thus, the permittivity obtained in the laboratory is related with the permittivity of the polyethylene (base) and the sample under test.

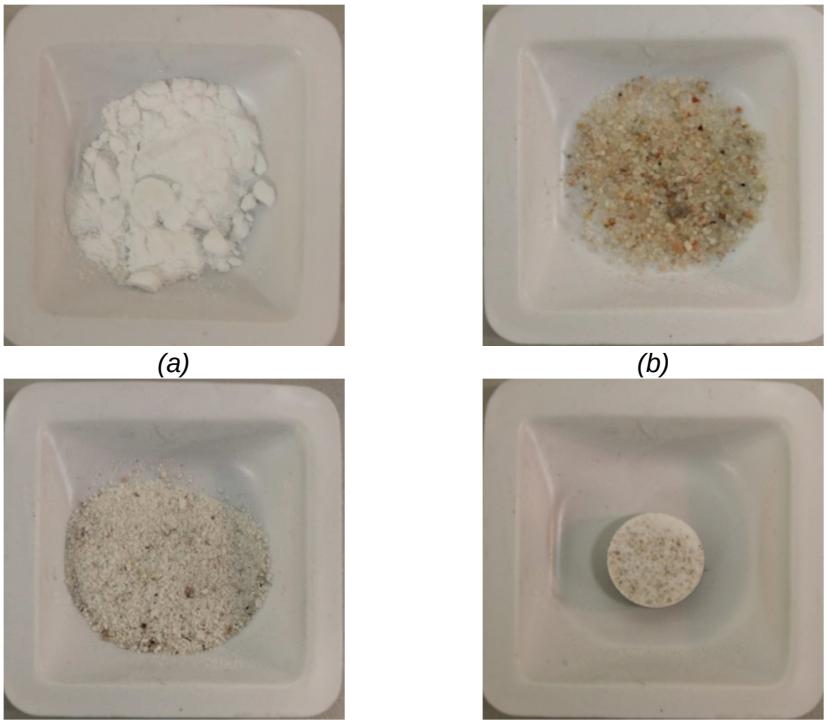

Fig. 3.3. Different stages of the pellet fabrication: (a) PE powder, (b) Sample powder, (c) mix of PE and sample and (d) the final pellet

Typically, these samples were measured using TPS Spectra 3000 equipment (it is described in the next section) due to its high dynamic range, bandwidth and beam waist (smaller than 5 mm). To be able to measure the sample, several pellets have to be manufactured. These pellets are

fabricated with the powder sample mixed with polyethylene (PE). PE is included to measure any quantity of the powder sample in similar conditions (thickness and weight of the obtained pellets)

Normally, the overall weight of the pellets is 350 mg. In most cases, the pellet will be composed of 250 mg of PE (Fig. 3.3a), whose refractive index is 1.5, and 100 mg of the corresponding sample (Fig. 3.3b). Other mixing rates have also been studied as indicated in their correspond sections. Once both quantities are perfectly mixed (Fig. 3.3c), the pellets are created by means of a hydraulic press, able to create 10 tons strength (Fig. 3.3d).

For each characterized sample, several pellets have been done with the aim to check that the properties remain the same independently of the sample and also to verify the repeatability of the manufacturing process of the pellets.

The larger wavelength to be measured is 5 mm (0.06 THz). In order to minimize the spill-over of the THz beam around the sample, the diameter of the pellets was fixed to 13 mm. Note that the final thickness of the pellet is different for each sample, due to the distinct behavior of each sample against pressure.

As PE has been used in the sample, its electromagnetic parameters affect the measured permittivity. To avoid this influence, the effect of the PE refractive index was eliminated using the Maxwell-Garnett mixing rule [Maxwell1904]:

$$\varepsilon_{eff} = \varepsilon_{PE} + 2f_{rac}\varepsilon_{PE} * \frac{\varepsilon_{SUT} - \varepsilon_{PE}}{\varepsilon_{SUT} + \varepsilon_{PE} - f_{rac}(\varepsilon_{SUT} - \varepsilon_{PE})} \tag{3.17}$$

Where ε_{PE} is the permittivity of the PE; ε_{SUT} is the permittivity of the sample under test; ε_{eff} is the permittivity of the pellet, measured in the laboratory and f_{rac} is the ratio between the sample weight and the total weight of the pellet.

Note that this equation can eliminate the influence of each base used in measurements and it can be applied for solid powder samples or powder samples in liquid medium, as it is descripted in the next subsection.

III.3.2.2.- Solid Sample inside Water Medium

The second special case of powder samples is descripted in this section. In this situation, the powder sample is dissolute in a liquid medium (typically water) e.g. a solution of the sample of interest. Note that, it is placed inside a container, just to be able to measure the liquid medium.

In this case, there are three resonance mediums and four interfaces, as they are illustrated in Fig. 3.4.

- Air (n_1)-Container wall(n_2)
- Container wall (n_2)-Sample medium(n_3)
- Sample medium(n_3)-Container wall (n_4)
- Container wall (n_4)-Air (n_5)

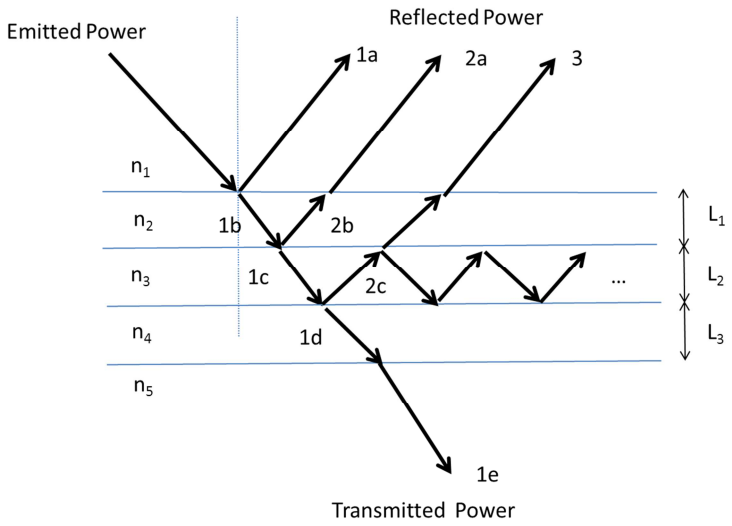

Fig. 3.4. Schematic of the model for the liquid sample

Some approximations have been used to describe this model due to its characteristics: first interface (air-container wall) has been modeled using the model descripted in section III.3.1; only one reflected (1a) and one transmitted ray (1b) have been taken into account.

Second interface has been modeled using the model described in section III.3.2. In this case, the transmitted ray calculated above is used as

incident ray for this interface. It is important to remark that, for this thesis only four rays have been used for the characterization of this model (see Fig. 3.4):

- Ray 1a: Provides information about the interface air-wall container and it is the first reflected ray achieved.
- Ray 2a: It is the second ray reflected. It provides information about the interface Container wall (n_2)-Sample medium (n_3). Note that if the thickness of the container (L_1) is electrically small (it will depend on the frequency range of measurement) ray 1a and ray 2a can be detected like only one contribution (as there is no time difference between them).
- Ray 3: Third ray detected. It provides information about the interface Sample Medium (n_3)-Container wall (n_4). Note that, in this case, ray 1b is considered as the incident ray to use Eq. (3.13).
- Ray 1e: It is the first transmitted ray. It is calculated using Eq. (3.14) as a resonance medium (n_3).

Note that media n_1 and n_2 only the first transmitted ray is considered. They are not as resonance media. To model these samples, Eq. (3.17) has to be used in order to eliminate the influence of the water, but the permittivity of the water is modified by the frequency and the temperature. In order to characterize this influence, the Double-Model of Debye has been descripted [Lie1991]. With this model (Eq. (3.18)), a frequency dependent complex permittivity will be obtained. Using this permittivity in Eq. (3.17), the influence of the water can be eliminated.

$$\varepsilon_{\text{water}} = \varepsilon_0 - \text{freq}\frac{\varepsilon_0 - \varepsilon_1}{\text{freq} + j\gamma_1} + \frac{\varepsilon_1 - \varepsilon_2}{\text{freq} + j\gamma_2} \tag{3.18}$$

Where ε_{water} is the complex permittivity of the water, T is the temperature of the water and freq is the frequency (GHz), ε_0 is the static dielectric constant of pure water, ε_1 and ε_2 are the first and second high frequency constant and γ_1 and γ_2 are the primary and secondary relaxation frequencies. Note that this model is valid from 1 GHz to 10 THz. [Lie1991].

Double-Model of Debye model uses the static dielectric constant of pure water, ε_0 which depends on the temperature, T, by Eq. (3.19) and Eq. (3.20).

$$\varepsilon_0 = 77.66 - 103.3\theta \tag{3.19}$$

$$\theta = 1 - 300\frac{1}{273.15 + \mathrm{T}} \tag{3.20}$$

Note that these expressions are valid for $-20º \leq T \leq 60º$. Once this static dielectric constant has been calculated, first and second high frequency constant, ε_1 and ε_2 are obtained.

$$\varepsilon_1 = 0.0671\varepsilon_0 \tag{3.21}$$

$$\varepsilon_2 = 3.52 + 7.52\theta \tag{3.22}$$

Furthermore, primary and secondary relaxation frequencies, γ_1 and γ_2 are also obtained, in order to calculate all the date for the final expression of the complex permittivity of the water.

$$\gamma_1 = 20.20 + 146.4\theta + 316\theta^2 \tag{3.23}$$

$$\gamma_2 = 39.8\gamma_1 \tag{3.24}$$

III.3.3.- Ellipsometry

Ellipsometry technique consists on the measurement of the change in polarization of a light beam upon reflection from the sample under test. Using the expressions descripted below, the refractive index of that sample can be obtained. Furthermore, if the sample is composed by several layers of different materials, it is possible to calculate the refractive index and the thickness of each layer [Tomp2005].

Taking into account some parameters (frequency and angle of incident), this technique can be classified as follows. If it is based on a single frequency, it is called single-wavelength ellipsometry. If ellipsometry is a function of the frequency, it is named spectroscopic ellipsometry. Furthermore, if it is a function of the angle of incident, the ellipsometry is referenced as multiple angle of incident ellipsometry. Finally, if ellipsometry is based on both parameters, frequency and angle of incident, it is called variable angle spectroscopic ellipsometry [Tomp1999].

The main characteristic of the ellipsometry system is the use of polarizers. These devices are used to set the polarization of the incident beam and they are critical components of any ellipsometric system. They are optical elements which convert a light beam of any polarization state into a light beam with a single polarization state. The deviation in the linear state of polarization is used to characterize the sample by its refractive index, as it will be commented below [Tomp1999].

III.3.3.1.- Reflectance

The reflectance is defined as the ratio of the intensity of the outgoing wave to the intensity of the incoming wave.

Some definitions are necessary to complement the reflectance. The amplitude of the electric field wave in the plane of incidence is defined as E_p and amplitude perpendicular to the plane is called E_s. The incident wave is divided into two waves, p-waves with amplitude of E_p and propagating in the plane of incidence and s-waves, with amplitude of E_s and propagating in the perpendicular plane of incidence. Also, total reflection coefficients R^P and R^s, using the two interfaces schemes depicted in Fig. 3.5, are defined as:

$$R^P = \frac{r_{12}^p + r_{23}^p e^{-j2\beta}}{1 + r_{12}^p r_{23}^p e^{-j2\beta}} \qquad R^s = \frac{r_{12}^s + r_{23}^{ps} e^{-j2\beta}}{1 + r_{12}^s r_{23}^s e^{-j2\beta}} \tag{3.25}$$

$$r_{12}^p = \frac{n_2 \cos\theta_1 - n_1 \cos\theta_2}{n_2 \cos\theta_1 + n_1 \cos\theta_{t2}} \qquad r_{12}^s = \frac{n_1 \cos\theta_1 - n_2 \cos\theta_2}{n_1 \cos\theta_1 + n_2 \cos\theta_{t2}} \tag{3.26}$$

$$\beta = 2\pi \frac{L}{\lambda} n_2 \cos\theta_2 \tag{3.27}$$

where r_{12}^p and r_{12}^s the Fresnel coefficients for the interface n_1-n_2 and β is the phase change in the wave

Finally, the reflectance, $\Re$, can be defined as

$$\Re^p = |R^p|^2 \qquad \Re^s = |R^s|^2 \tag{3.28}$$

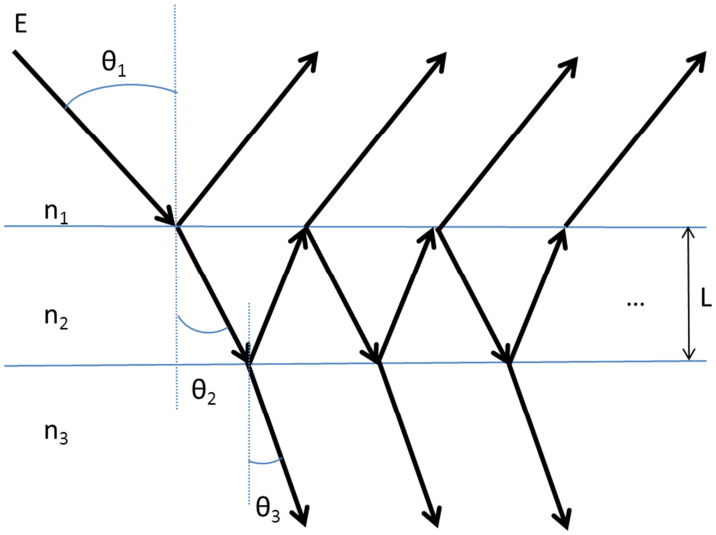

(a)

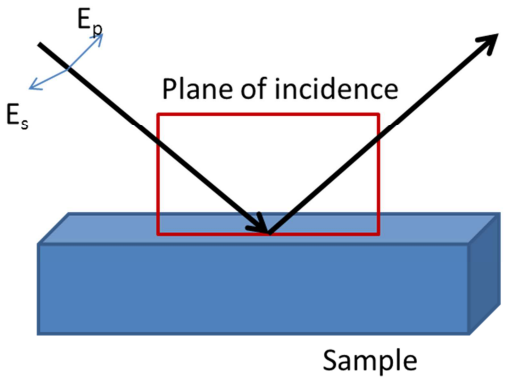

(b)

Fig. 3.5. (a) Theoretical model used for ellipsometry and (b) decomposition of the Electric field.

III.3.3.2.- Delta and Psi

The p-waves and the s-waves are not necessary in phase so that phase difference between the p-wave and the s-wave before the reflection is called δ_1 and after the reflection, δ_2. The parameter Δ is the phase shift due to the reflection over the sample. It is defined as:

$$\Delta = \delta_1 - \delta_2 \tag{3.29}$$

Reflection over the sample also introduces an amplitude reduction for both p-waves and s-waves that can be calculated using total reflection coefficients, R^p and R^s. Parameter Ψ is defined as the angle whose tangent is the ratio of the magnitudes of the total reflection coefficients.

$$\tan\Psi = \frac{|R^p|}{|R^s|} \tag{3.30}$$

III.3.3.3.- The fundamental Equation of Ellipsometry

If a new parameter, ρ is defined as the complex ratio of the total reflection coefficients:

$$\rho = \frac{R^p}{R^s} \tag{3.31}$$

The fundamental equation of the ellipsometry then is

$$\rho = \tan\Psi e^{j\Delta} = \frac{R^p}{R^s} \tag{3.32}$$

The parameters $\Psi \text{ and } \Delta$ are measured by the ellipsometer and using the equations related above, electromagnetic parameters such as refractive index and thickness of the sample can be calculated.

Taking into account all the parameters descripted above, a null-ellipsometry measuring system was design and developed (this system is descripted in Section III.4.4). Null ellipsometry is a very solid, simple technique (single-wavelength ellipsometry) that involves changing the angle of the analyzer (polarizer after the sample) to find the null in the detector for an angle of incident, θ_i. Parameters Ψ and Δ are calculated using the null angles and these equations:

$$\tan \Psi = |\tan P|$$

(3.33)

$$\Delta = 2A \pm \frac{\pi}{2}$$

(3.34)

Where P is the angle of the polarizer, and A is the angle of the analyzer that yields a null. Both values are introduced in Eq. (3.35) to calculate the refractive index of the sample under test:

$$n_2 = n_1 \tan(\theta_i) \sqrt{1 - \frac{4\rho sin^2\theta_i}{(\rho + 1)^2}}$$

(3.35)

This equation is based on Eq. (3.32), Eq. (3.33) and Eq. (3.34). Note that n_2 is the refractive index of the sample and n_1 is the refractive index of the medium around the sample, typically air.

III.4.- Description of systems for electromagnetic characterization

Different measuring systems have been used for electromagnetic characterization. In this section, the description of each one is presented.

III.4.1.- Measuring system for thick samples

This setup is based on the imaging system descripted in Chapter II. As it has been commented, the system is based on a Network Analyzer to emit and detect power, and a quasioptical system to focalize the electromagnetic beam over the sample (Fig. 3.6). Note that the sample is characterized by only one measurement point.

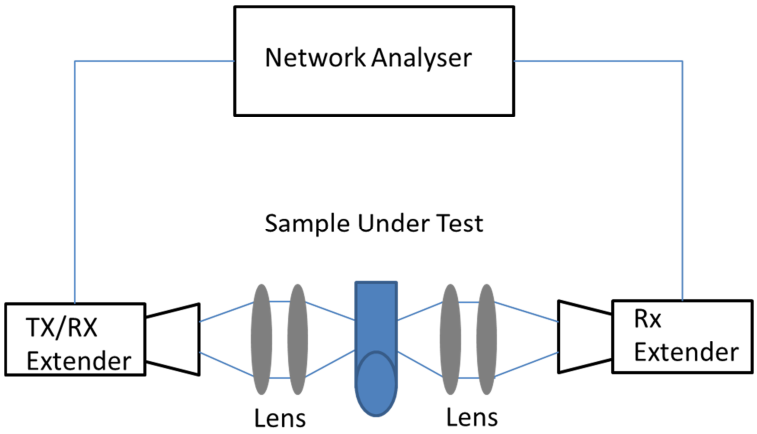

Fig. 3.6. Scheme of the measuring system for simple samples

With this configuration, transmission (S_{21}) and reflection (S_{11}) measurements can be obtained. A specifically software has been developed (it is based on the theoretical model presented in Section III.3.1) to obtain the permittivity and the refractive index of the sample under test from the measured scattering parameters.

As this system characterizes thick samples (electrical size of the sample) only reflection power is measured (note that the transmitted power through the sample is absorbed by the sample itself).

Note that the network analyzer is able to measure the time evolution of the sample. In this case, it is important to remark that this measurement is not consider as an electromagnetic characterization, but it provides useful information about the evolution of the parameters of sample (refractive index or permittivity) as a function of the time. Thus, several samples have been studied using that technique (some examples are presented in Chapter IV):

- Spanish sausage (“chorizo”) curing process
- Water content level evolution in plants

III.4.2.- THz-TDS: Teraview TPS Spectra 3000.

The measurements have been carried out using a commercial TPS Spectra 3000 [Teraview]. This equipment is a floor-standing terahertz transmission spectrometer. It is based on an ultra-fast pulsed laser technology with laser gated photo-conductive semiconductor emitter and receiver to generate and detect terahertz energy.

The transmission through the sample of a terahertz pulse is compared to a reference measurement and the sample parameters measured (Fig. 3.7). In order to eliminate the water absorption peaks the sample compartment is purged with nitrogen.

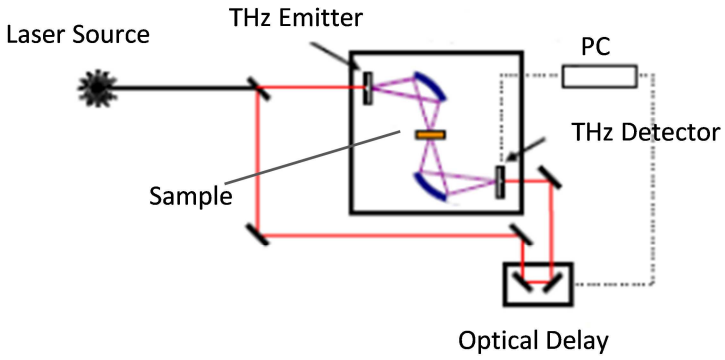

Fig. 3.7. Scheme of the measuring system of the TPS Spectra 3000

Thin samples (simple solid samples, powder samples and liquid samples) can be measured and characterized by THz-TDS for the frequency range 0.060 THz to 3.5 THz with a dynamic range higher than 70 dB. Furthermore, the beam waist is lower than 5 mm [Teraview].

Note that, although TPS Spectra 3000 has two external headers to measure larger samples in transmission or reflection configuration. They have not been used for transmission characterization because it is not possible to eliminate water vapor and oxygen absorption. Also, the dynamic range using those external headers is lower than the level obtained in the sample compartment. Note that these external headers are going to be used in the reflection scheme which is commented in the next subsection

This system provides the capability of characterizing a sample by its refractive index, permittivity and absorbance. For the sake of comparison with its Teraview software, specifically dedicated software has been developed. Note that this software takes into account all the secondary reflections (as it is described in Section III.3.2) while the Teraview software only characterize the sample using the firs transmitted ray (Section III.3.2).

III.4.3.- Reflection System

As it has been introduced, Teraview TPS Spectra 3000 can measure reflection properties of the material using the external headers of the equipment.

In this case, a normal incident reflection system was designed. As emitter and detector the Teraview external headers were used. To focus the THz beam, some lenses were included in the system. In order to reduce the path of the beam a Silicon wafer was included, working as beam splitter. The scheme is depicted in Fig. 3.8

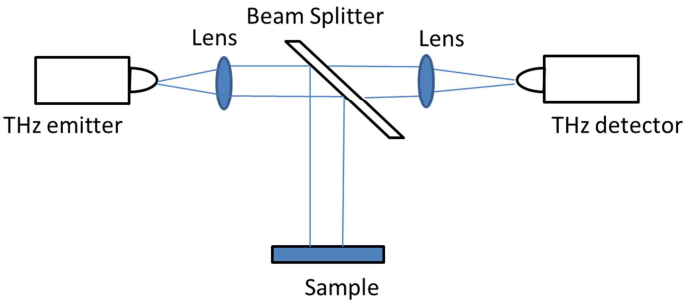

Fig. 3.8. Scheme of the reflection measuring system

The THz beam is emitted by the external header and goes through the first lens until the beam splitter. It divides the beam and the first part goes until the sample. In the backward path, when the beam arrives to the beam splitter, it is bent on a second lens that focalize the power into the detector.

This system can be used to check the reflection information and also to obtain a better characterization of the sample under test. Note that the system cannot be purged using nitrogen gas due to the use of the external headers, as it has been commented in the previous Section. Furthermore, due to the lower dynamic range provided by the external headers, reflection system has been not used in this thesis and an ellipsometry system has been implemented for reflection measurements.

That system measures at only one frequency, thus, the influence of the oxygen and water vapor is reduced. Also, it is based on the angle of the polarization (descripted below) not in the level of detected power. That is why the lower dynamic range takes no influence on the characterization.

III.4.4.- Ellipsometric System

In this case, a null ellipsometry system was design and developed. As a source/detector for the system, the TPS Spectra 3000 remote headers are used and the working frequency used for the characterization is 1 THz.

Note that the TPS Spectra 3000 provides a large bandwidth, as a matter of fact, the system can also be configured as THz spectroscopic ellipsometry system.

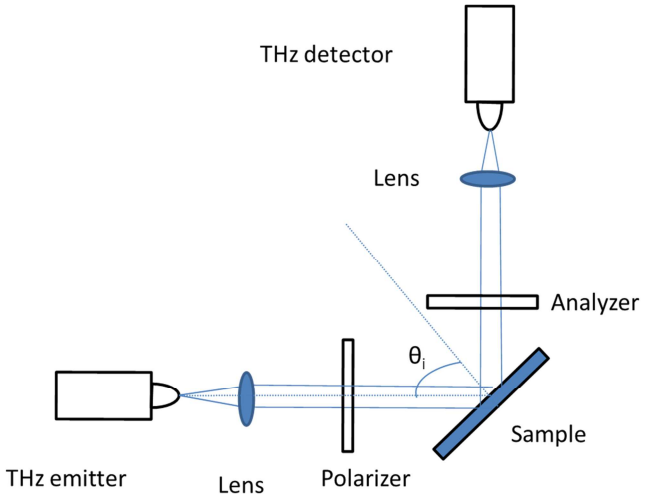

Fig. 3.9. Scheme of the ellipsometric measuring system

In order to obtain a focused beam, two lenses focus the power from the emitter to the polarizer (or from the last polarizer to the detector) as it is depicted in Fig. 3.9.

Refractive index of the sample can be obtained using this measuring system. Note that, as this system works at one single frequency. Thus, the influence of water vapor and oxygen of the air is mitigated.

This ellipsometry is a PSA type (Polarizer-Sample-Analyzer) without compensator (C) [Tomp1999]. Some ellipsometry systems (typically null-ellipsometry systems) use a compensator (for a PCSA type), where the compensator introduces a phase difference of $\pm\pi/4$ between p-wave and s-

wave (Section III.3.3). Note that a PCSA system is more complex than a PSA system, due to Compensator. It is remarkable that this device can be eliminated to simplify the system. In this situation, Eq. (3.32) is calculated using Eq. (3.33) and Eq. (3.34) instead of using the phase difference (Eq. (3.29)) and magnitude ratio (Eq. (3.30)).

In this case, the compensator has been not included to obtain a Rotating Analyzer Ellipsometer (RAE) manually operated (note that a RAE system is a PSA null-ellipsometer with a rotating analyzer controlled by a computer) [Alva2002].

It is important to remark that the polarizer angle has been arbitrary fixed to 45º. (polarization angle of the THz beam is also 45º) [Tomp2005]. This angle determinates four regions where the detected electric field is null (see Section III.5.3 for a large explanation of the measuring process). Thus, the equations described in [Alva2002] can be used for the characterization.

III.5.- Electromagnetic characterization of materials

In this section, some examples of the electromagnetic characterization systems implemented for this thesis are presented.

Firstly, a THz-TDS for explosive study is presented. In this case, the absorbance and the refractive index of the sample are calculated for the characterization. The characterized explosives are PETN; TNT, RDX, bullet gunpowder and mine gunpowder. Note that the explosives have been characterized before, to check previous results and, to extend actual databases, after the detonation. It is very important to remark that mine gunpowder and detonated explosives have been measured for the first time in this dissertation.

Secondly, a null ellipsometry system is used to obtain the refractive index of a Silicon wafer and an ellipsometric characterization of the explosives is also presented.

Finally, THz-TDS system and ellipsometry technique are compared.

III.5.1.- Explosives Characterization

This thesis aims at complementing the previous referred works [Huang2004] [Allis2006] [Liu2006] [Leahy2007a] [Wilk2008] [Allis2008] by dealing with the electromagnetic characterization of different explosives by the refractive index [Haring2003] and the absorbance [Leahy2007b] in the THz range. This study has focused on those explosives commonly used in terrorist attacks, and were provided by Spanish National Security Force “Guardia Civil”: mine gunpowder, PETN, TNT, RDX and bullet gunpowder. In particular, to the best of our knowledge, the mine gunpowder explosive has been analyzed for the first time in this thesis.

These explosives have been selected due to several reasons: RDX is one of the most powerful of the military high explosives. It was developed in order to obtain an explosive power than TNT and it has been used for several terrorist attacks (1993 in Bombay, or al-Qaeda in 1999 in Los Angeles). Furthermore it is one of the compounds of the Semtex (explosive for general purpose) together with PETN, other of the most powerful high explosives known. PETN has also used in terrorist attacks by al-Qaeda

(Nigeria, 2009 or Arabian Peninsula 2010). For instance, 400 grams of PETN can blast a hole in an aircraft skin.

The explosive yield of TNT is considered to be the standard measure of strength of bombs and other explosives. Thus, it is very important to characterize it. Bullet gunpowder has been analyzed because it is very common in the bullet industry (police/military or sport context). Finally, the selection of mine gunpowder came as a special request from the “Guardia Civil” due to the relatively easy availability from any mine.

III.5.1.1- Refractive Index

In order to characterize the electromagnetic response of the compounds, the refractive index of the pellets was measured. (These pellets have been manufactured mixing PE and explosive, as described in Section III.3.2.1). This value is calculated using an in-house tool (Section III.3.2) which uses the TPS Spectra 3000 transmission measurements data. The influence of the PE is eliminated using Eq.(3.17).

The refractive index of all the analyzed explosives presents frequency ranges of constant value (see Fig. 3.10), separated by spectral resonances, which create absorption peaks (Fig. 3.11a). In average, their refractive index is: gun explosive (n_{GUN}=1.6), PETN (n_{PETN}= 1.44), mine gunpowder (n_{MINE}=1.55), TNT (n_{TNT}=1.46) and RDX (n_{RDX}=2). Note that the refractive index of each explosive is represented until the limit frequency (cutoff frequency) where the system sensitivity is reached, i.e. the signal is smaller than the noise floor of the system [Jepsen2005]. This procedure will be followed in all the results presented along the Section III.5. Note that the position of the resonance peaks is independent of the explosive pellet used in each case. For the sake of simplicity, only one measurement of each explosive has been included in this section. The other results are presented in the Appendix A.

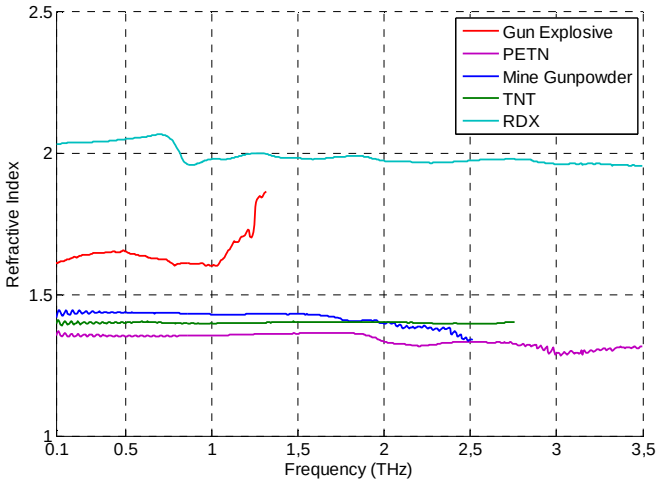

Fig. 3.10. Refractive index of characterized explosives

III.5.1.2- Absorbance

Fig. 3.11b shows the absorbance analysis of the different explosives. This analysis gives the spectral information about the absorption peaks (fingerprint) of each substance and the overall THz spectral behavior (Table 3.2). In the case of the bullet gunpowder, a very sharp absorption coefficient slope leading to very high absorbance value at 1.25 THz can be appreciated together with resonance peaks placed at 0.78, 1.03 and 1.15 THz. From 1.2 THz on, the measured results are neglected due to the loss of signal into the receiver, as it has been commented above.

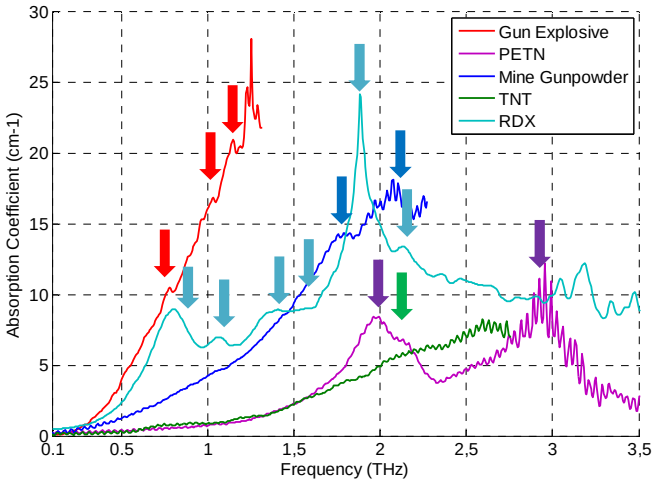

(a)

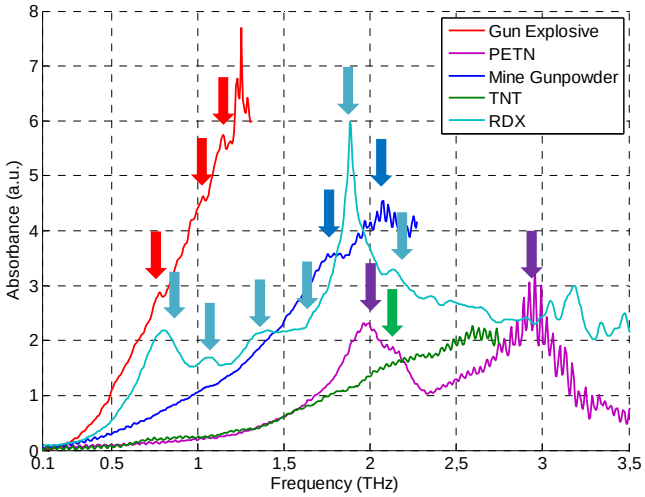

(b)

Fig. 3.11. (a) Absorption Coefficient and (b) Absorbance of the measured explosives

In the case of PETN two clearly resonance frequencies, at 2 and 2.8 THz can be found. These measured resonance values have already been measured in previous works [Palka2010] [Leahy2007b]. There is another resonance frequency, described in [Chen2007] and ratified also in this work, placed at 2.16 THz.

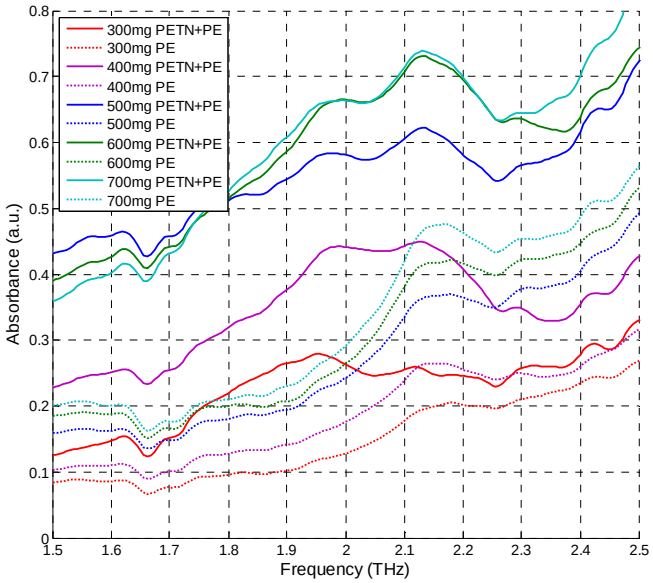

Fig. 3.12. Absorbance of different quantities of PETN and PE.

However, this resonance frequency cannot be considered as a characteristic frequency of the PETN. This peak appears due to the inclusion of the PE in the pellet. This is corroborated with the results shown in Fig. 3.12. In this figure, the absorbance of pure PE and PE-PETN samples of different weight is compared. The resonance peak of the PE-PETN samples at 2.16 THz is caused by the absorbance response of the PE.

As it can be seen in Fig. 3.12, the resonance peak place at 2.16 THz appears in all the graphs, not only in the curves composed by PETN+PE. Thus, this resonance peaks is due to the PE not to the PETN.

For the first time, the mine gunpowder has been spectrally characterized at THz frequencies. This explosive exhibits two resonance frequencies, at 1.75 and 2.1 THz, as depicted in Fig 3.11b. Note that no references exist up to now. RDX presents several absorption peaks at 0.8,

1.08, 1.3, 1.55, 1.95 and 2.2 THz as in the results presented in [Chen2007] [Palka2010] [Liu2006] [Leahy2007b].

On the other hand, the absorbance of the TNT presents a resonance peak at 2.1 THz [Leahy2007a]. Furthermore, this explosive has a monotonic growth from 1.3 THz to 2.5 THz.

Table 3.2.- Resonance Frequencies

Explosive	Resonance Frequencies *(THz)*
Bullet gunpowder	0.78; 1.03; 1.15
PETN	2;2.8
Mine gunpowder	1.75; 2.1
TNT	2.1
RDX	0.8; 1.08; 1.3; 1.55; 1.95; 2.2

The results obtained here are very similar to the resonance frequency peaks of the explosives that can be found in the bibliography validating the measurements and the corresponding test system.

III.5.2.- Detonated explosives characterization

Previous section have measured the absorbance and the refractive index of different explosives which have been characterized at laboratory level, it means, samples of non-detonated explosives. Although non-detonated explosives characterization is very important to identify the origin and type of explosive in counterterrorism fight, a data-base of detonated explosive can also be even more very useful in this context.

This section is focused on the electromagnetic characterization of different detonated explosives using Time Domain Spectroscopy in the THz range (THz-TDS). It is very important to remark that, to the best of our knowledge, this is the first time that a detonated explosive is characterized.

Spanish National Security Force “Guardia Civil” together with the Antenna Group detonated samples of common explosives, such as PETN, TNT and RDX. After the detonation, samples of the exploded compounds have been characterized in the laboratory, using the theoretical model presented in this thesis (Section III.3.2).

III.5.2.1- Explosive detonation

Firstly, to prepare the detonations, a plastic box was filled with sand for every explosive. Secondly, in each case, a detonator and explosive material were placed inside the box (Fig.3.13). Finally, the detonator starts the process by an electric excitation and the explosive is detonated. Note that explosives were detonated by Guardia Civil experts.

After the detonation, a sample of the sand burned by the detonated explosive was collected into a plastic container. These samples will be characterized in laboratories.

(a) *(b)*

Fig. 3.13. (a) Sample ready for the detonation and (b) sample detonated.

III.5.2.2- Sample preparation

Several pellets were prepared to characterize the explosives in the TPS Spectra 3000. In this case, 250 mg of PE and 100 mg of explosive were mixed to obtain a pellet of 350 mg, following the procedure described in Section III.3.2.1. Note that the detonated explosive sample is formed by sand and detonated explosive.

III.5.2.3- Reference sample

In addition to sample pellets, a pellet made with 250 mg of PE and 100 mg of “white sample” was done. The white sample is formed by the sand using in the detonations and an exploded detonator. That is why the detonator has been used in every explosion as a starter for the detonation. Thus, the detonator after the explosion has been characterized and used as reference.

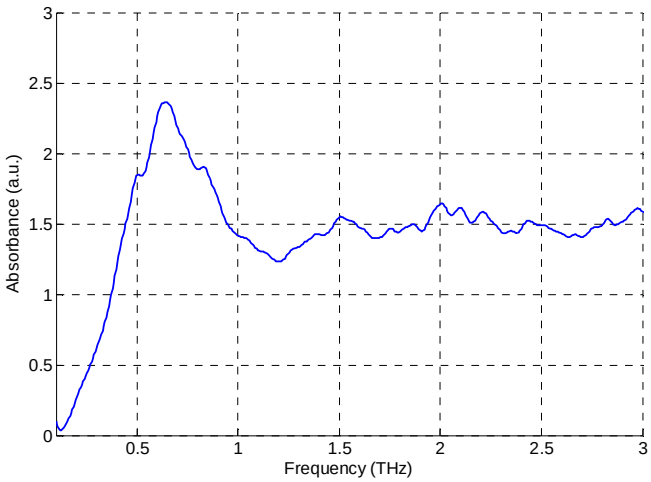

Fig. 3.14 Absorbance of the sample made with the exploded detonator and PE base

As it is depicted in Fig. 3.14, the reference sample has a significantly peak at 0.8 THz. This absorption peak will appear in each characterization because the detonator is present in each sample of detonated explosive.

III.5.2.4- Refractive index of detonated explosives

The refractive index of the detonated explosives has been measured as it is descripted in Section III.5.1.1. It presents intervals of constant value (see Fig. 3.15). As in the previous case (Section III.5.1.1), they are separated by absorption peaks which will be described in the following section. In average, their refractive index is: PETN (n_{PETN}= 1.46), TNT (n_{TNT}=1.50) and RDX (n_{RDX}=1.55). Note that the refractive indexes of PETN

and TNT are very similar to the refractive indexes obtained for non-detonated PETN and TNT (n_{PETN}= 1.44, n_{TNT}=1.46, see Fig. 3.10). On the other hand, the refractive index of RDX presents the large difference (detontated n_{RDX_D}=1.55 and non-detonated ,n_{RDX_ND}=2).

Finally, it is important to remark that the change in the trend due to the resonator (placed at 0.8 THz) in the case of the RDX is softer than in the other two cases. Thus, the peak of the resonator will be smoother in the absorbance of the detonated RDX.

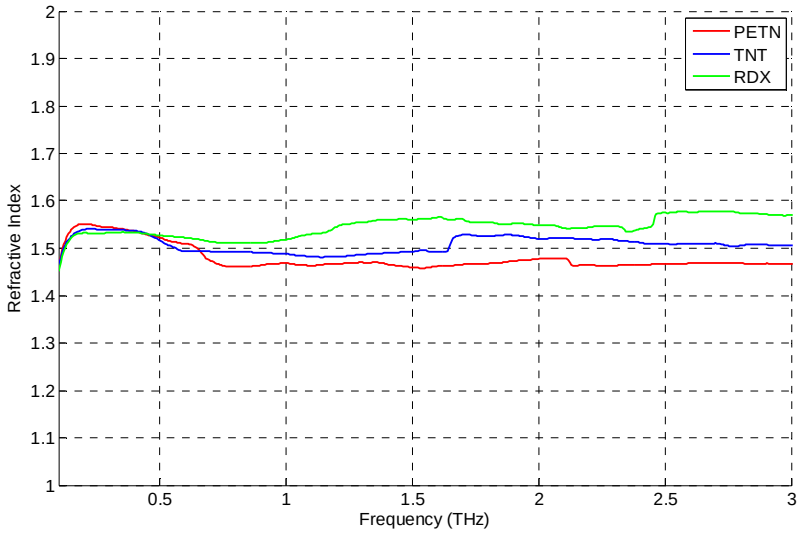

Fig. 3.15 Refractive Indexes of the detonated explosives

III.5.2.5- Absorbance of detonated explosives

In this subsection, the absorbance of the detonated explosives is presented.

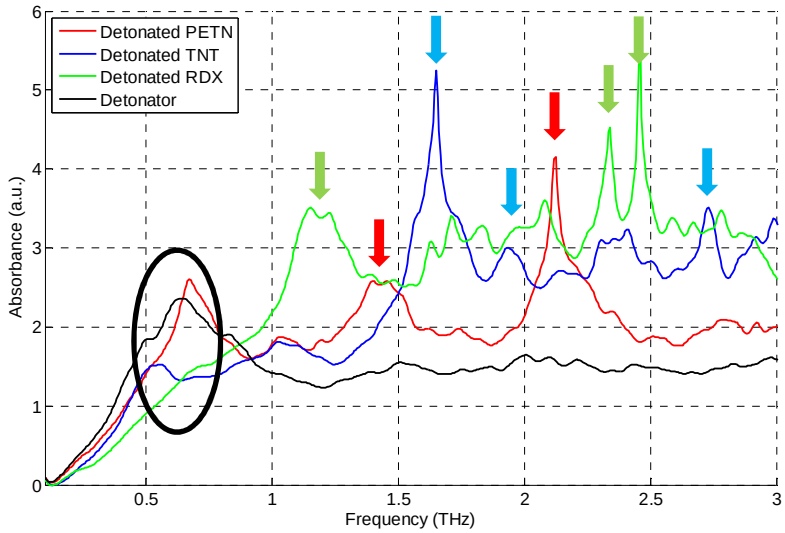

Fig. 3.16 Absorbance of detonated explosives

As it is depicted in Fig. 3.16, the absorption peak due to the detonator appears at 0.8 THz in each graph (they are rounded by a black circle). In the case of detonated PETN, two resonances (1.45 and 2.15 THz) are clearly identified. Note that only peaks that are positioned at the same frequencies that trend changes in the refractive index are descripted. This procedure has been following for all the explosives. Thus, several minor peaks are not considered.

Detonated TNT exhibits more resonance peaks (1.55, 1.95 and 2.75 THz). There is also a remarkable zone, near to 2.45 THz where several peaks appear. Note that those peaks are placed at the same frequency that the trend changes in the refractive index.

Absorbance peaks of the detonated RDX are placed at 2.4 and 2.5 THz. Also, several peaks are detected near to 1.2 THz.

III.5.2.6- Absorbance comparison

In Table 3.3, the absorption frequencies of the non-detonated (Section III.5.1.2) and detonated explosives are listed. It is important to remark that it is supposed that these frequencies are different since the chemical reaction during the detonation has transformed the commercial explosive into a detonated explosive. As it can be seen in this Table, there are appreciable differences in the resonance peaks. Note that the peaks placed at 0.8 THz are not listed as they are introduced by the detonator.

Table 3.3.- Main absorption frequencies

Explosive	Commercial Frequencies *(THz)*	Detonated Frequencies *(THz)*
PETN	2;2.8	1.45; 2.15
TNT	2.1	1.55;1.95; 2.45; 2.75;
RDX	0.8; 1.08; 1.3; 1.55; 1.95; 2.2	1.2; 2.4; 2.5

Note that these absorption frequencies of the detonated explosives would allow identifying each explosive.

III.5.3.- Silicon characterization by Null Ellipsometry

These measurements have been achieved in order to characterize the null ellipsometry system implemented for this thesis (Fig 3.17), a null ellipsometer working at 1 THz [Alva2002] [Hoffmann2006]. This system is descripted in Section III.4.4.

In this case, a silicon wafer has been characterized by the model described in Section III.2.3.

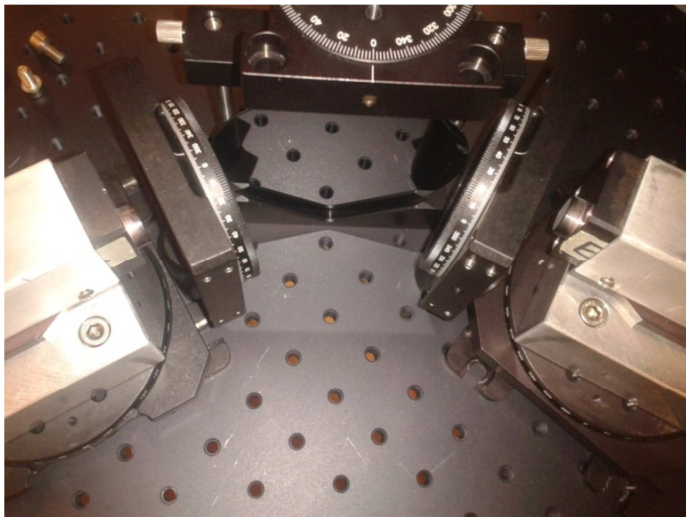

Fig. 3.17 Photo of the null ellipsometer mounted in the laboratory.

III.5.3.1- Measuring procedure

Firstly, the angle of incident over the Silicon wafer, a critical parameter for an ellipsometry system, has been fixed to 70º. As the system is based on TPS Spectra 3000, the angle of incidence has been calculated taking into account the diameter of the pellets (13 mm as it is described in Section III.3.2). Note than these pellets have a diameter of 13mm, enough for THz-TDS, but a slightly small for the ellipsometry system. Due to this fact and after some simulations, the incident angle has been fixed to 70º (θ_i=70º).

Secondly, the angle of the polarizer (polarizer before the sample) to 45º (P_i=45º). This angles fixes four zones where the spectrum is expected to be nulled [Alva2002]. These zones are presented in Table 3.4.

Thirsty, the null angles of the analyzer (polarizer after the sample) have been founded around 10º (A_1=10; A_2=8.5º; A_3=10.5; A_4=9º).

Table 3.4.- Pairs of Ψ and Δ

Zones	Ψ	Δ
1	P_1	$2A_1 + \frac{\pi}{2}$
2	P_2	$-2A_2 - \frac{\pi}{2}$
3	$-P_3$	$2A_3 - \frac{\pi}{2}$
4	$-P_4$	$-2A_4 + \frac{\pi}{2}$

Using Eq. (3.33) and Eq. (3.34), four null-pairs have been obtained in the zones presented in Table 3.4. Calculated refractive index, using Eq. (3.35) is depicted in Fig. 3.18.

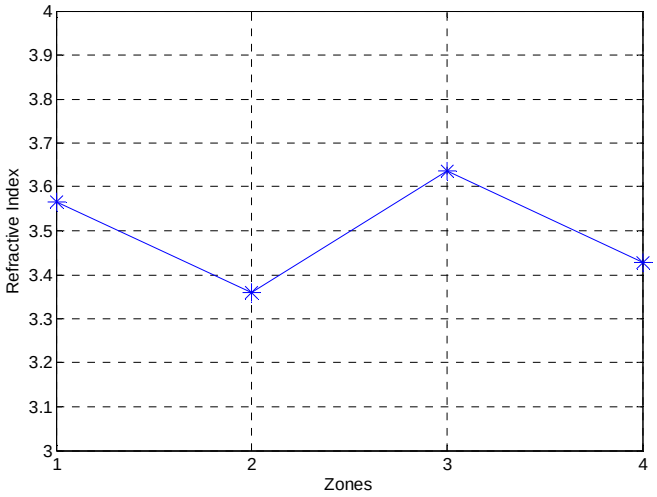

Fig. 3.18. Calculated refractive index of a Silicon wafer.

As it can be seen, the results are around n=3.5, while the refractive index of the silicon is n_{SI}=3.44. Although the system has not achieved an exact value, this result can be improved using better positioning system and better angular precision.

III.5.4.- Explosive Characterization by Null-Ellipsometry

For the sake of comparison null ellipsometry with THz-TDS, the same samples characterized in Section III.5.1 have been measured again. As it has been commented, the samples are gunpowder, mine gunpowder, TNT; PETN and RDX.

As in the case of the Silicon wafer characterization, the angle of the polarizer is 45º (P=45º) and the angle of incident is θ_i=70º. Table 3.5 shows the obtained results:

Table 3.5.- Refractive index measured with THz-TDS and null ellipsometry

Explosive	n THz-TDS	n Null ellipsometry
Gun explosive	1.6	1.55
PETN	1.44	1.31
Mine gunpowder	1.55	1.54
TNT	1.46	1.39
RDX	2	1.95

It is important to remark that these results have been obtained as an average of four measurements for each case, following the procedure descripted in the previously section.

Note that both results have been compared at 1 THz. Both techniques THz-TDS and null ellipsometry provides very similar results.

Unlike the THz-TDS system, null ellipsometry system can characterize thick samples or samples with high attenuation in the THz range. Also, if the sample is composed by several layers of different materials, this technique allows to measure the refractive index and the thickness of each layer [Alva2002]. Note that this characteristic is a future development of this system.

On the other hand, THz-TDS provide a higher dynamic range (the path is shorter and THz radiation is lower attenuated). Also, the characterization can be performed in a large bandwidth not at only one frequency.

III.6.- Conclusions

In this chapter, several electromagnetic characterization systems and the theoretical model followed for their design have been presented. Also, the electromagnetic parameters used for the characterization (permittivity, refractive index, absorption coefficient and absorbance) have been introduced. These systems have been demonstrated be able to characterize several materials in the THz, measuring in transmission or reflection configuration, by the defined parameters.

Firstly, a measuring systems based on a network analyzer has been implemented. This system characterizes thin samples in the range 0.090 - 0.500 THz. It measures the scattering parameters and is based on the theoretical model for one single interface to obtain the refractive index and/or permittivity of the sample (using Fresnel coefficients).

The second system is a THz-TDS commercial device. It allows measuring the absorbance and the refractive index of small samples, powder samples or liquid samples, from 0.060 THz to 3.5 THz in transmission/reflection configuration (note that each sample has its particular theoretical model).

In order to illustrate an application for this system, an electromagnetic characterization (based on the absorbance and the refractive index) of several non-detonated explosives (mine gunpowder, PETN, TNT, RDX and bullet gunpowder) has been performed. Note that this system allows identifying these compounds by its absorbance spectrum.

Also, the absorbance and the refractive index after the detonation of some explosives (PETN; TNT and RDX) have been measured and it presents clearly identifiable peaks. These resonances allow distinguishing among explosives even after the detonation. Thus, THz-TDS can be used for the identification of several compounds in transmission configuration, as it has been demonstrated using non-detonated and, for the first time, detonated explosives.

Moreover, a null ellipsometry system has been implemented. This system determinates the refractive index of samples based on the state of polarization of the detected beam and it uses the external headers of TPS Spectra 3000 as emitter and detector. As it has been shown, the

implemented system can identify materials in reflection configuration by its refractive index.

Finally, for the sake of comparison, THZ-TDS system and null ellipsometry system have measured non-detonated explosives. This system allows to obtain the refractive index of the analyzed explosives and the results agree with the THz-TDS values. It is possible to conclude that THz-TDS and the null-ellipsometry system developed for this thesis provide similar results. On one hand, null-ellipsometry can obtain the refractive index of thin and thick samples at one single frequency. On the other hand, THz-TDS provides a large bandwidth and a higher dynamic range for the characterization (by the refractive index and absorbance) of thin samples.

CHAPTER IV

THz APPLICATIONS OF THE IMPLEMENTED SYSTEMS

Several applications of the THz systems implemented for this thesis are presented in this chapter. First section is related with the imaging system and its capabilities for water evolution control for agriculture applications. Secondly, a food industry application for unwanted objects detection is related. Last section shows a study of explosives focused on the manufacturing process and the sensitivity of the system

IV.1.- Introduction

Chapters II and III have described measurement techniques (imaging system and characterization systems) implemented for this thesis. In this chapter, some studies based on those systems are presented.

In first section, an agriculture application of the imaging system is shown. In this case, the imaging system measures the water content level evolution by transmission and reflection images. Note that some samples were measured in real time and other samples every 24 hours. Thus, both approaches have been compared.

Secondly, a preliminary study of the THz images focused in the detection of unwanted objects (quality control process) is descripted. This study tests the viability of the THz radiation for developing a quality control system for food industries.

Thirstily, in order to complete the explosives characterization performed in Chapter III, measurements about the study of non-pure explosives and the comparison of differently manufactured PETN samples have been performed in this Chapter. Furthermore, the sensitivity of the measuring system is also analyzed.

Finally, some conclusions of the THz radiation based on the obtained results are commented.

IV.2.- Applications of THz technology in Agriculture

In this section, a leaf has been measured in the THz range to study its water content level. The imaging system (Chapter II) has obtained images of the leaf in transmission and reflection configuration and an average value of the achieved power in each case has been performed in order to determine the water content of the leaf. Note that two types of analysis have been performed (each 24 hours and every minute) using both techniques.

IV.2.1.- Study of water evolution for agriculture application

In this case, the performances of a reflection system for water control monitoring are analyzed. In particular, the feasibility study of a single pixel sensing system to measure the water content of a plant by THz inspection of the leaves in reflection mode is presented. For the first time and as a difference with previous works, such as [Hadjiloucas2002] [Zhang2008], reflection measurements are used, which from a practical point of view, lead to simplified sensor system (with non-destructive, non-invasive and real-time properties). As a first step towards the design of this sensor, transmission and reflection images in the range of 0.140 to 0.220 THz have been obtained in the frequency domain, using a network analyzer as emitter/detector. Note that an extended analysis of this study for a broadband frequency range is provided in Appendix B. In this Section and after the results presented in Appendix B, the selected operational frequency is f=0.215 THz. These results show the viability of the reflection systems and their advantages versus transmission configurations to characterize water content distribution inside the leaf.

Thus, a leaf was cut and placed in the imaging system during three days. Fig. 4.1 presents a photo of the leaf on the first day (day of cutting) and 48 hours later. Note that there is difficult to appreciate any difference in visible spectrum about water level content.

(a) *(b)*

Fig. 4.1. (a) Photo of the leaf the day of cutting and (b) 48 hours later

IV.2.1.1.- Characterization of the water content in transmission

Transmission images (f=0.215 THz) at different times (t_0, t_0+24h and t_0+48h) were taken over the same sample. The obtained results are presented in this Section.

Those results can be seen in Fig 4.2. For the sake of comparison the imaging results, the images were post processed in order to quantify the drying evolution process. The average of the power transmission through the leaf was calculated. The values obtained for each image are summarized in Table 4.1.

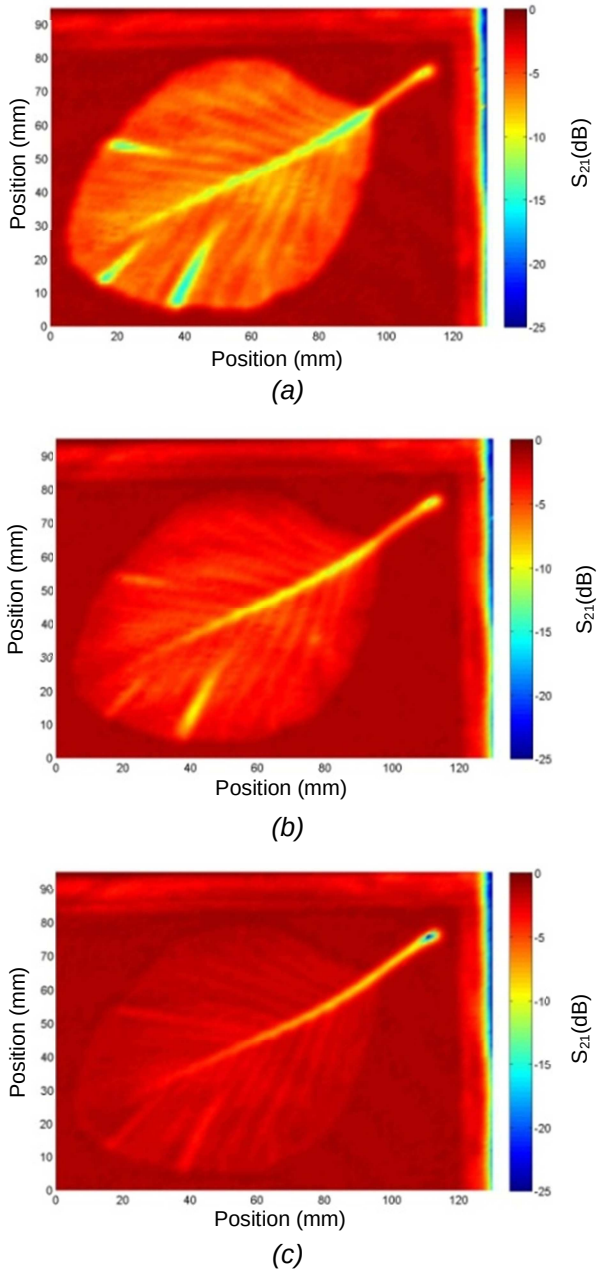

Fig. 4.2. (a) THz image in transmission of the first day, t_0 (b) THz image 24 hours later, t_0+24 hours. (c) THz image 48 hours after the day of cutting, t_0+48 hours. , f=0.215 THz

Table 4.1. Average Transmitted Power Trough the Leaf, f=0.215 THz

Time *(Hours)*	Value *(Modulus)*
0	0.332
24	0.498
48	0.667

Transmission images at 0.215 THz show differences in water content (as it can be seen in Table 4.1), due to the transmitted signal level dependence with the water content. A high level of water content is related with a low transmission, i.e. green color in the image (larger attenuation due to the water contain and reflection produced by a high permittivity) and a low value in Table 4.1. The transmission level has been duplicated in only two days as it is identified by a higher value of the average power (Table 4.1). It can be observed that the amount of transmitted power is increased in a lineal way (from 0.332 to 0.498 and from 0.498 to 0.667). This variation is not possible to identify in the visible image (Fig. 4.1), but it is characterized and quantified at the THz range (Fig. 4.2 and Table 4.1). The reduction of water content level is translated in an increase in the transmission level. Note that all the values in Table 4.1 are below 1, as they are normalized.

IV.2.1.2.- Characterization of the water content in reflection

In this case, the reflected power and the corresponding phase (f=0.215 THz) are recorded with the Transmission/Reception Module. The set-up is simpler than in the transmission case (there is only one pair of lenses and one OML extender) and will be in line with a future sensor. As in the case of the previous subsection, this parameter will be directly dependent of the amount of water in the leaf. The images obtained with this method are represented in Fig 4.3. Results of the averaging post process of the reflected power (modulus of S_{11}) are presented in Table 4.2.

Table 4.2. Average Reflected Power In the Leaf, f=0.215 THz

Time *(Hours)*	Value *(Modulus)*
0	0.215
24	0.118
48	0.074

In this case, a small value of S_{11} in Fig. 4.3 (darker area) can be linked to a low level of water content in the leaf. As it has been commented in Chapter II, if the leaf has a high water content level, the permittivity will be higher and the reflected electromagnetic power will be larger (S_{11} magnitude will be higher). For the first studied case, image at t_0, the leaf shows an averaged reflection level of 0.215. This value is reduced in the next cases, t_0+24 and t_0+48 (see Table 4.2). After 24 hours, the values have been reduced close to the half, meanwhile after 48 hours the values are three times smaller.

From the transmission and reflection results depicted in Table 4.1 and 4.2, and assuming small scattering due to the relatively long wavelength used, the average absorption values, included in Table 4.3, can be inferred. The absorbed power decreases as a function of time once the leaf has been cut. The absorption due to the water content at the leaf moves from 45% to 25% (almost half the initial value) in 48 hours.

Table 4.3. Average Absorption Power Levels In the Leaf, f=0.215 THz

Time *(Hours)*	Value *(Modulus)*
0	0.453
24	0.393
48	0.259

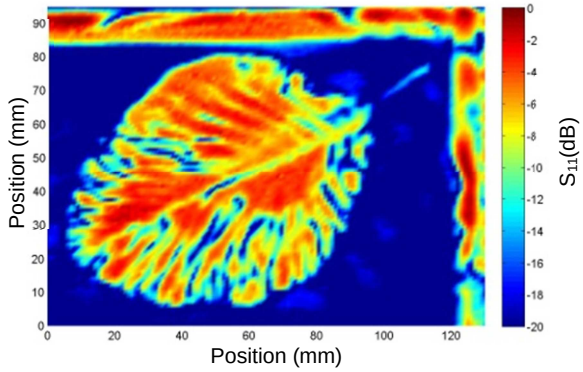

(a)

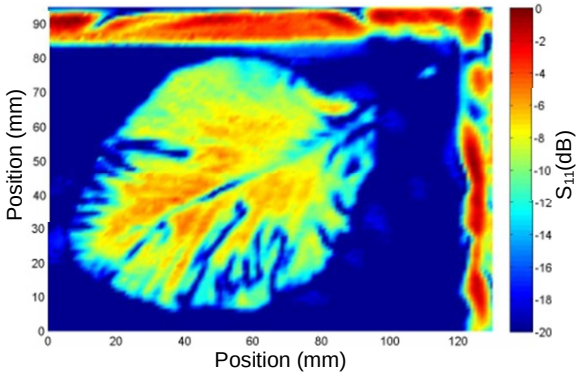

(b)

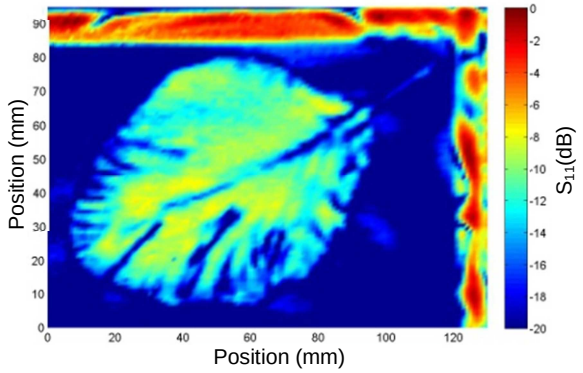

(c)

Fig. 4.3 (a) THz image in reflection of the first day (b) THz image 24 hours later. (c) THz image 48 hours after the day of cutting, f=0.215THz.

IV.2.2.- Water content evolution by control points

IV.2.2.1.- Analysis of the water content evolution from imaging results

Time evolution of the water content in different areas of the leaf has been analyzed. Three sample points were selected (see Fig. 4.4). The first one was placed out of the leaf and represents the reference value. As expected, the level of this line does not exhibit changes with time. The leaf stack was selected as the second zone. The third part was chosen near the border of the leaf. In Fig. 4.5 and Fig. 4.6, three lines representing the evolution of the reflection and transmission of these three sample regions are depicted.

Regarding reflection values, the results are presented in Fig. 4.5. The solid line in Fig. 4.5 is the reference value, taken in an area where there is no leaf. It has a low value (-25 dB approximately) and its variation is negligible.

The dotted line (sample zone 2) corresponds with the leaf stack. This is the point of the leaf with the highest water content and the last to be dried. Therefore it exhibits the highest value of reflected power. The received power decreased along the time, due to the drying process. In this case, an overall reduction in the reflected power of 82% is obtained (In Fig.4.5 it is represented by -9dB of difference). Note also that the drying process is not lineal, being less pronounced with time evolution.

The dashed line (sample area 3) exhibits a similar behavior than the previous case. At the beginning, its level is lower than in the leaf stack, and after 48 hours, it is 2.5 times higher than the reference. It is clear that the drying process is faster in the leaf border than in the leaf stack. In this case, the measured reduction in the reflected power is 92%.

Note that a large analysis has been performed in Appendix B to validate this method and the frequency selection.

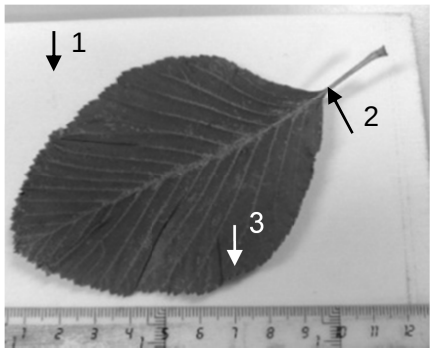

Fig. 4.4. Characterization areas for results depicted in Fig. 4.5 and Fig.4.6. 1.- Sample Control. 2.-Leave stack. 3.- Leave border

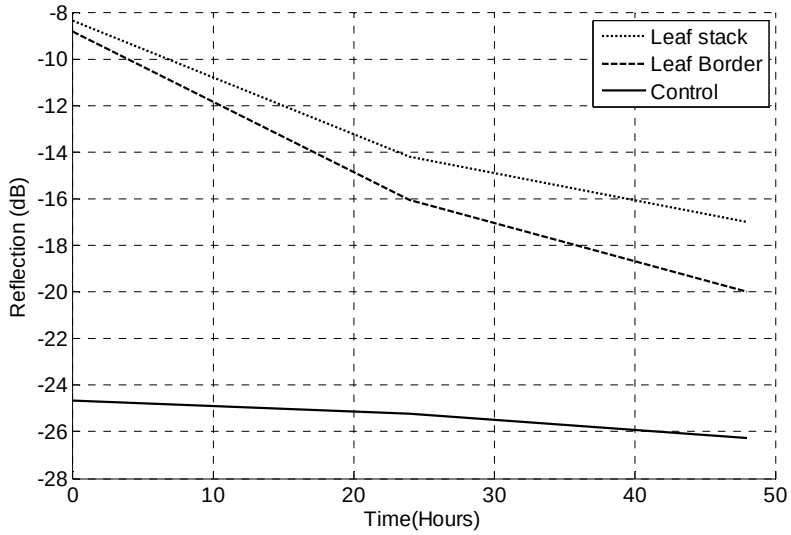

Fig. 4.5. Water evolution of the reflected signal in the points indicated in Fig. 4.9 at f=0.215 THz.

From the sake of comparison, the transmission results are also shown, see Fig. 4.6. Similar results to those corresponding to the reflection case have been obtained. The reference area (point 1) does not show any variation with time. In the case of the leaf stack, dotted line, there is a change of transmission due to the water content reduction. In the plot, the higher water content corresponds to a low level of received power (13 dB

which means 20 times lower than the control value). After 48 hours of study, the level of transmitted power was increased. It means that the absorption due to the water content in the leaf stack is lower as the leaf is drying. The final value, compared with the control point, is 5 times lower.

The dashed line (point 3) is related with a point placed at the border of the leaf. In this case, the water content is lower than in the leaf stack case, as shown by the higher transmission value. In particular, the difference of levels is close to 7dB, which means a relative difference between points of 80%.

In this case, the received power level tends to the value of the reference when time is progressing, which means that the remaining water is very low. Meanwhile, the leaf stack still keeps considerable amount of water, as its level of reflected power is 8dB lower than the reference (control point). It means that leaf stack has a water content level more than 5 times higher than the border of the leaf.

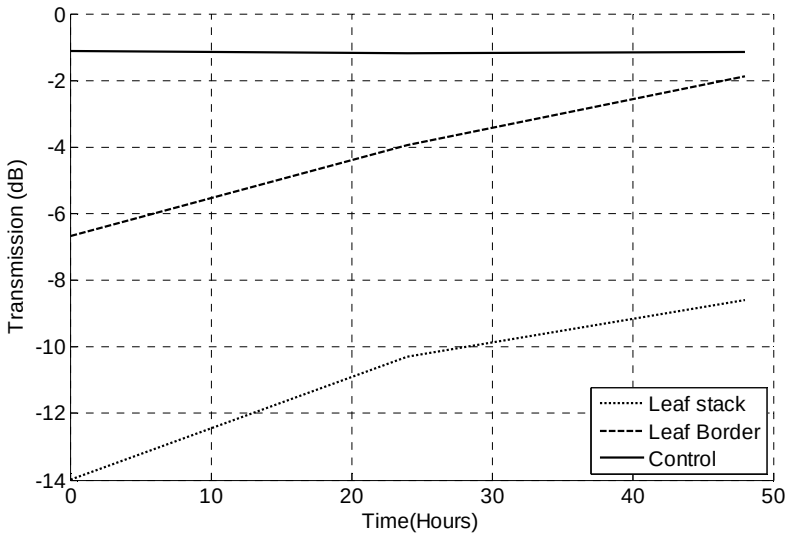

Fig. 4.6. Water evolution of the transmitted signal in the points indicated in Fig. 4.9 at f=0.215 THz.

IV.2.2.2.- Water content evolution from continuous measurements along time

In previous section, an analysis of the water content absorption (from imaging results) has been performed every 24 hours. This Section presents a real-time analysis of the water content evolution. In this study, S_{21} and S_{11}-time domain parameters were measured each minute during two days.

Unlike the results presented in the preceding section, only one point has been monitored in this case. This point was selected in the border of the leaf because of, as it has been demonstrated in Section IV.2.1.1, border area is the most sensible part to water variation.

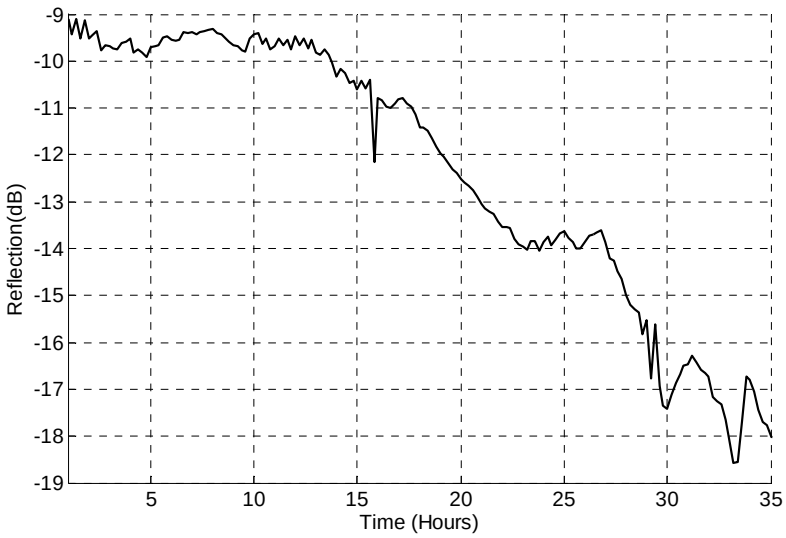

Fig. 4.7. Time evolution of the power reflected by a sample point placed in the leaf border at f=0.215 THz.

In this case, the time evolution of the reflected power by the leaf at 0.215 THz is depicted in Fig. 4.7. Note that in this case, the parameter S_{11} in frequency domain has been measured. During the first hours the leaf still keep stable its water content. Afterwards the drying process is evident; 24 hours later, the leaf reflects 60% less power (4dB less reflected power). In

the next hours, this reflected power continues clearly its reduction. As previously mentioned, this decreasing in the value of the reflected power is due to the change in the permittivity of the leaf caused by the reduction in its water level content.

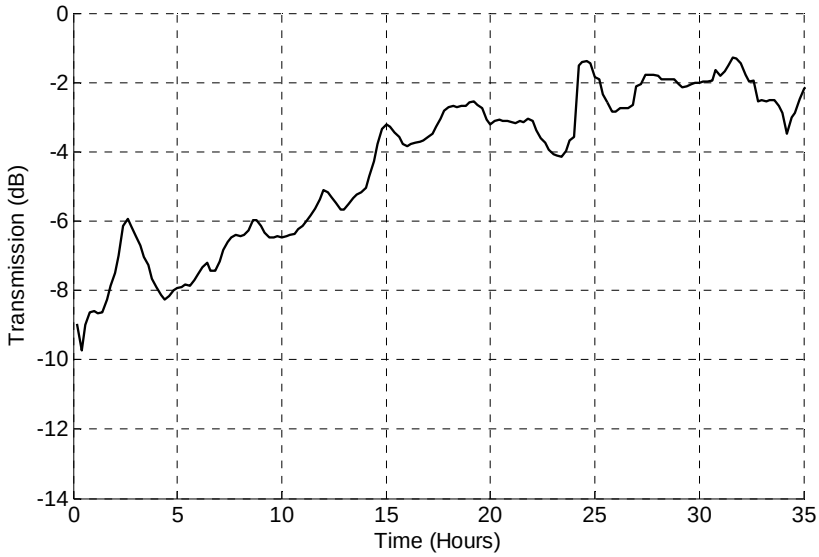

Fig. 4.8. Time evolution of the power transmitted through a sample point placed in the leaf border at f=0.215 THz. Note that this point is the same point measured for Fig.4.7

For the sake of comparison, the S_{21} parameter at 0.215 THz is depicted in Fig. 4.8. As can be seen, transmission power duplicates (in linear scale) its value in 24 hours (more than 3dB larger power received). Note that this tendency coincides with the results shown in Fig. 4.6 although there is a small discrepancy. Comparing both figures (Fig 4.6 and Fig. 4.8) can be determined that in Fig 4.6, the transmitted power measured in the leaf border starts around -7 dB while in Fig 4.8, it starts in -9 dB. This difference of 2 dB comes from the position of the monitored leaf point at the border used for this experiment.

IV.3.- Quality Control in Food Industry

Water content study related before can be used in the food industry, for a non-destructive, non-invasive testing and one-by-one control of the cured process (quality control). Thus, the viability to of THz radiation to detect potentially harmful objects inside the food product (such as plastic parts or metal objects) is shown in this section. This study is focused on the detection of those objects inside the sample (Section II.5.2,).

The system (Section II.4.1) allows detecting defects or unwanted elements in the object under test. Some images of a Spanish sausage ("chorizo") which has been prepared with unwanted objects are presented.

Firstly, two glass fragments (objects 1 and 2) and a metal piece (object 3) were introduced in a Chorizo slice and a THz transmission image was obtained (f=0.200 THz). The results are presented in Fig. 4.9.

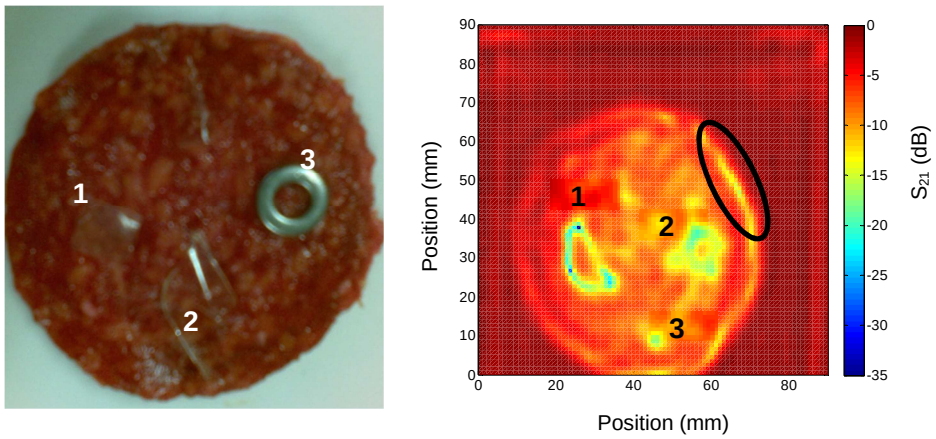

(a) (b)

Fig. 4.9. (a) Visible image of the chorizo slice and (b) THz transmission image of the same slice at f=0.200 THz.

It is possible to detect the three elements inside the sample by the difference observed in the transmitted power level. (Those items present a level around -17 dB while the level in the rest of the sample is -5 dB). This power difference allows detecting unwanted objects and differentiating them

from the sample, but it is not possible to identify the items (note that one of them is a metal ring and the other two are glass fragments and they present a similar power level).

There are also small zones of the sample which have a power level around -14 dB (rounded with a black circle). Although there are 3 dB of difference, it is necessary to improve the detection capability of the system in order to detect objects unambiguously.

Due to these considerations, instead of taking transmission images which are attenuated due to the water content of the sample slice, reflection images were achieved. This technique has been used to obtain more significant differences between the objects (these differences will appear in the reflected power level). Some of them that have been placed in the sample: metal pieces, glass fragments, paper scraps or plastic parts. Note that these items simulate objects that could be found in a food production chain. In Table 4.4, the kind of material and the size of each item placed in the slice of chorizo have been listed.

Table 4.4. Unwanted objects

Item	Material	Size (mm^2)
1	Paper	2x2
2	Plastic	4x4
3	Metal	2x2
4	Metal	6x8
5	Glass	3x6
6	Glass	3x15

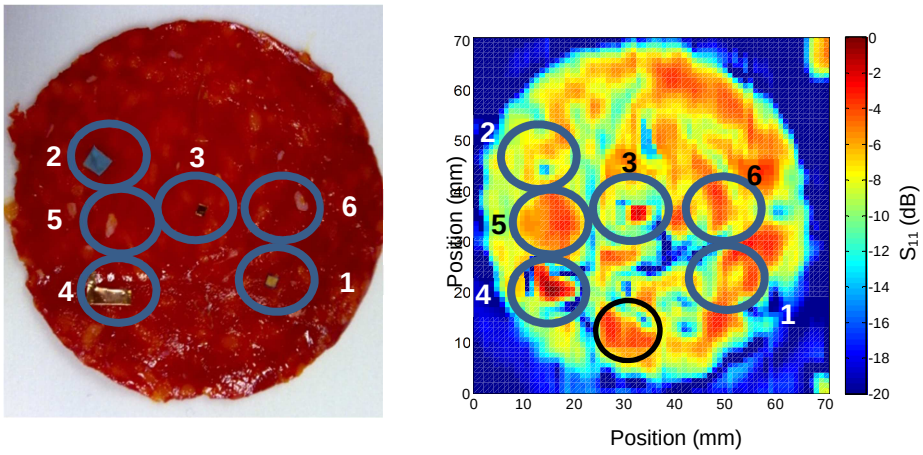

(a) (b)

Fig. 4.10. Visible image of the chorizo slice (a) and THz reflection image of the same slice (b) at f=0. 200 THz.

As it is depicted in Fig. 4.10, these small objects can be detected by THz image inspection (f=0.200 THz). For several applications, like in food industry, this detection can be enough: it is better to have a false positive (an element has been detected but it is not an unwanted object) than a false negative error (an item object has been not detected). On the other hand, it is necessary to remark that too many false positive errors can make that the system reject samples in good conditions.

However, due to the difference power level achieved at the detector, it is also possible to differentiate the type of the objects. As it has been commented in Chapter II, a piece of metal in reflection measurements appears as a maximum in the S_{11} parameter (the metal reflects the power). In this case two objects appear with high value in Fig. 4.10, number 3 (-3 dB) and number 4 (-3.5 dB). On one hand, object number 4 is detected by the THz system (see Fig 4.10b). On the other, object number 3, due to its small size, generates some doubts. It can be an unwanted object or can be a part of the sample. Thus, only one item (object 4) can be identified as a metal piece. On the other case (object 3), the system does not have enough resolution to detect the metal piece without doubts.

Secondly, glass fragments present similar levels of power (5 and 6) but they cannot be detected. In this case, differences cannot be found between them and the sample slice (for the case of metal pieces, the differences are around 2 dB while in this case; the difference is lower than 1 dB). On the other hand, both glass fragments have been detected in Fig. 4.9, Thus, the fragments (5 and 6) of this case are too thigh (the resolution achieve, 2 mm for this frequency range, is not enough) to detect them. Finally, items 1 and 2 have been not detected because the reflected power achieved is very similar to the reflected power by the sample.

As it has been shown in this section, THz images allow to detect objects either in transmission or reflection configuration. On the other hand, some problems have been identified.

The characteristics of the sample (absorption or water content) can affect to the measurements. In this case, in Fig 4.9 some zones (black circle) present a transmitted power level analogous to the elements under tests. Also, in Fig. 4.10 (black circle) are zones with a reflection level similar to the items allocated inside the sample. In both cases, it can generate a mistake in the detection system

Secondly, the resolution of the system is a critical parameter to detect objects, as it has been measured in the case of metal parts (Fig 4.10) and also, it is commented in Chapter II. In this case, it is very important to define the minimum resolution allowed in the system.

Thus, the combination of both techniques, transmission and reflection configuration could be a solution in order to obtain better images of the sample. Furthermore, as a function of the characteristics of the sample, a preliminary study (similar to that one) can determinate the operational frequency, the minimum resolution allowed and the best configuration for the final imaging system. In addition to that combination, a post-processing of the images can be implemented using computing tools in order to improve the detection capability of the THz system.

IV.4.- Explosives Characterization

In Section III.5, the refractive index and the absorbance of several explosives have been presented. In this section, first mixtures of explosives with additives have been analyzed and novel results (the characterization of the mine gunpowder [Etayo2013] and the absorbance spectrum of detonated explosives) have been obtained. This way the sensitivity in terms of the minimum explosive quantity required to detect it has been determined for the system TPS Spectra 3000. Besides, differences in terms of absorbance between pure explosives and explosives with additives (compounds added to stabilize the final product) have been measured.

As second point, for the first time, the influence of the manufacturing process used to make PETN has also been characterized by comparing the spectral properties of commercial versus home-made explosive. This result is considered very relevant for the Spanish National Security Forces in order to contribute to the identification of the explosive origin in counterterrorist investigations. Finally, a mixture of different explosive has been measured to check the capabilities of the system (TPS Spectra 3000, Section III.4.2) to determinate the spectral performances of a sample composed by two different explosives.

Several pellets were prepared and measured as it is described in Section III.2.3. With that theoretical model, the electromagnetic characteristics of the explosives were obtained. Note that all the samples have been prepared as Section III.3.2.1 describes. Furthermore, they have been measured using the TPS Spectra 3000 (Section III.4.2).

IV.4.1.- Spectral analysis of RDX with additives

In this analysis, the spectral influence of resins, coatings and additives added during the explosive manufacturing was studied. Commonly pure explosives are only available for industry, not for commercial use. Commercial explosives, though, are mixed with additional compounds to obtain the final product. For this evaluation, two samples of RDX were studied. The first one is an industrial sample of pure RDX, without any additives. The second one is a sample of RDX with the additives included to stabilize it and to reduce risks during handling and storage of the explosive.

Both explosives have been provided by “Guardia Civil” and the company MAXAM. This explosive was selected due to the fact that it is the one exhibiting more resonance peaks and any change produced by the use of additives can be easily reflected in its spectral behavior.

In Fig. 4.11, the spectral absorbance of the two samples is presented. The measured spectral resonance peaks appear at 0.8, 1.08, 1.3, 1.55, 1.95 and 2.2 THz in both cases, demonstrating the limited influence of the additives. Furthermore, in order to check the veracity of these results, a new set of measurements were performed using pellets with different quantities of explosive, decreasing from 100 mg to 50 mg. The amplitude of the absorbance peaks decreases along with the quantity of RDX, although the resonance frequencies are the same in both cases. Note that these pellets have always the same overall weight (350 mg), i.e., for example, 50 mg of explosive are combined with 300 mg of PE.

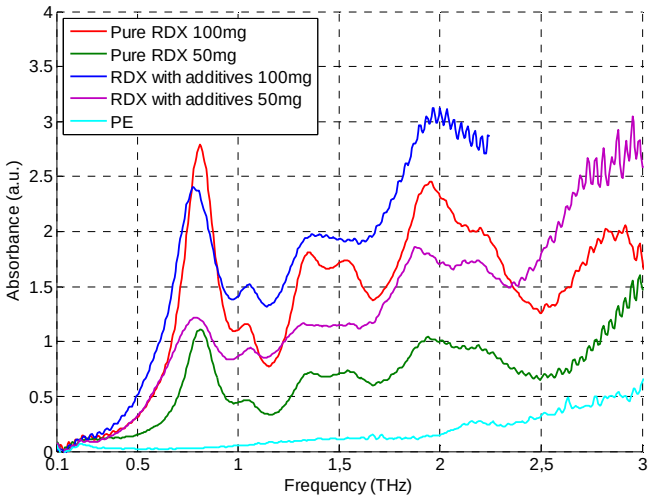

Fig. 4.11. Comparison between the absorbance of two types of RDX: Pure RDX and RDX with additives

IV.4.2- Spectral analysis of mixed explosives

This analysis was focused in finding out the capability of distinguishing between two different explosives mixed in one pellet. In this experimental study, an explosive composed by PETN and RDX was characterized. The pellet was manufactured using 175 mg of PETN and the same quantity of RDX. These values were chosen in order to have a final pellet of the same weight that in the previously analyzed cases. The results are presented in Fig. 4.12.

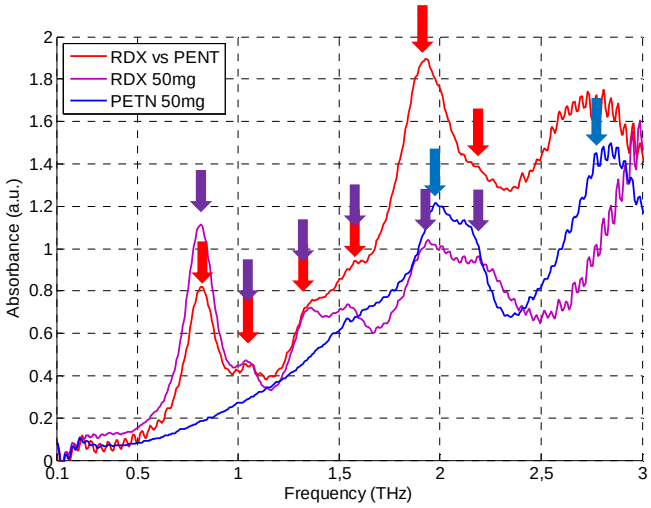

Fig. 4.12. Absorbance of a pellet made with RDX and PETN

The “RDSvsPETN” line corresponds to the mixed pellet, and it presents resonance peaks at 0.8, 1.08, 1.3, 1.55, 2, 2.2 and 2.8 THz. The “PETN 50mg” line shows the spectral response of PETN and the “RDX 50mg” line the RDX case. The peaks are placed at the same frequencies that the absorbance peak of the pure PETN (2 and 2.8 THz) and pure RDX (0.8, 1.08, 1.3, 1.55, 1.95, 2.2 THz).

Note that some peaks of the PETN (2 THz) are located very close to some peaks of the RDX (1.95 and 2.2 THz). As a consequence, the resonance peaks of the mixed pellet can be not as clear as the case of pure explosive (PETN or RDX).

IV.4.3- Spectral analysis of the manufacturing process

In the previous subsection, the influence of the additives used in the manufacturing process of a commercial explosive was studied. In this case, the samples under study were fabricated using two different processes. The first sample is a commercial PETN provided directly by the “Guardia Civil”. The second one corresponds to home-made PETN provided also by “Guardia Civil”. This explosive was selected due to the fact that it is the only one from the studied ones that can be manufactured by mixing different products bought in a drugstore.

Furthermore, as an extra experimental analysis, pellets with different amounts of explosive for both cases (commercial and home-made) were manufactured. The aim was to determine both the spectral difference between both compounds and the sensitivity of the measurement set-up.

From Fig. 4.13 it can be concluded that the resonance peak at 2 THz has a higher absorbance value in the case of home-made PETN that in the case of commercial PETN for all the pellets independently of the amount of explosive. Some differences can be appreciated at 2.8 THz. At this frequency, the pellet with 100 mg of commercial PETN presents a higher absorbance than home-made PETN. This difference is supposed to be caused due to the different additives used in each process.

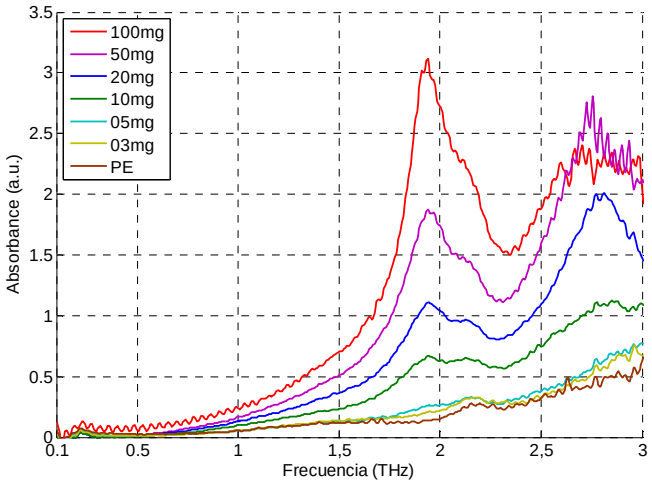

(a)

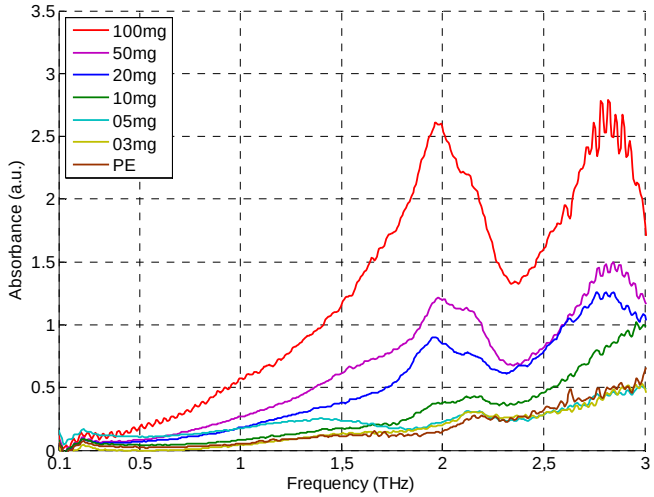

(b)

Fig. 4.13. Comparison between the absorbance of two different types of PETN: (a) Home-made PETN and (b) Commercial PETN

IV.4.4- Sensitivity of the measuring system

Taking advantage of the study performed in previous sections, some conclusions about the sensitivity of the system (TPS Spectra 3000), in terms of the minimum amount of explosive that can be detected, can be extracted. It is important to note that this sensitivity will be very dependent on the operational frequency (corresponding with the resonance frequencies for each explosive) and it will be obtained only for this measuring system, but it is possible to draw some guidelines for the case of PETN when the absorbance at the two characteristic frequencies (2 and 2.8 THz) are plotted versus the explosive quantity (from 5 mg to 100 mg). Fig. 4.14 shows these results.

For the sake of comparison the PE absorbance has also been represented. This value fixes the minimum sensitivity of the pellet due to the used mixture (PETN+PE). Therefore, for amounts of PETN larger than 10 mg the absorbance peak (it has been characterized in Section III.5.1.2) can be identified. On the other hand, the resonance peak at 2.8 THz needs a smaller quantity of PETN explosive to be detected (> 5 mg).

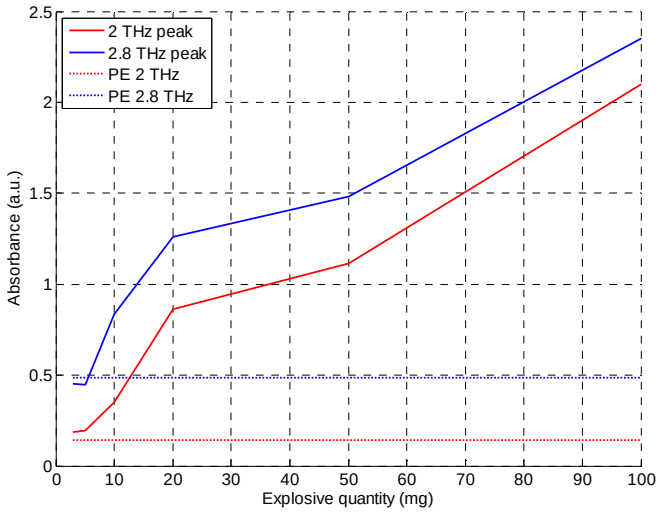

Fig. 4.14. Evolution of the absorbance of a PETN pellet as a function of the explosive concentration

Furthermore, it is also important to find out whether 10 mg of explosive is the limit of the system sensitivity or, on the contrary, this limit is due to the current concentration of explosive (10 mg over 350 mg total) used in the pellet.

In order to find it out, some extra measurements were carried out. In the next plot (Fig. 4.15) the sensitivity analysis of the system as a function of the weight of the pellet is represented. In this case, several pellets have been measured. For each pellet, the quantity of PETN included was fixed to 10mg and the quantity of PE added was that necessary to form pellets from 300 to 700 mg (in steps of 100 mg). With this variation of weight in each pellet, the influence of the explosive concentration can be checked. For the sake of comparison, the absorbance response of PE at 2 THz and 2.8 THz is also shown. Note that the weight of PE pellets also vary from 300 to 700 mg in steps of 100 mg. In all cases the 10 mg are distinguishable.

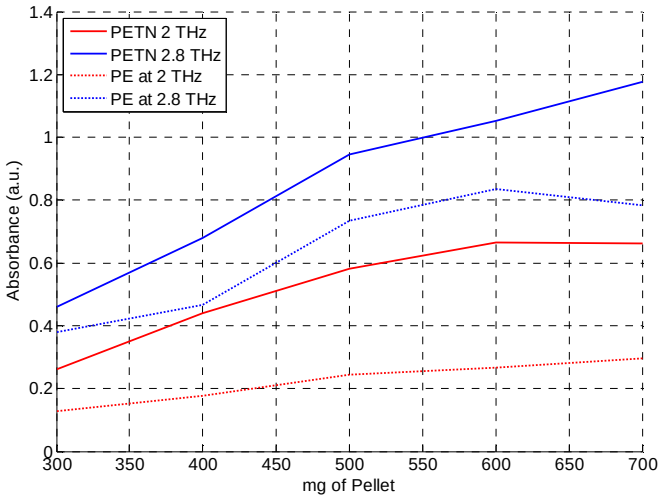

Fig. 4.15. Absorbance of 10 mg of PETN versus the weight of the pellet for the resonant frequencies 2 and 2.8 THz

As conclusion, the system exhibits enough dynamic range for all the pellet concentrations at both resonance frequencies. Therefore, the sensitivity of this system for the PETN explosive can be set to 10 mg.

IV.5.- Conclusions

In this chapter, the viability of the use of THz radiation for several applications has been demonstrated. As it has been shown, several samples (such as leaves, food samples or explosives) have been measured in the THz frequency range for future applications.

The obtained imaging results with an active sub-millimeter wave detection system confirm the possibility of developing water content sub-mm wave sensors based on the reflection properties of the leaves. These sensors will become an alternative technique for real time water control monitoring and will improve the quality control for instance in the viticulture industry.

THz wave high resolution images have been taken using transmission and reflection parameters at 0.215 THz. In these images, the distribution of water content inside the leaf, related with the power level in the detector, has been observed. As a matter of fact variations close to 50% of the reflected power during a 48 hours analysis have been measured.

THz characterization of water content level evolution has demonstrated a very useful method for irrigation control in agriculture. It provides a simple, real-time technique, able to measure differences that are not detected by optical inspection of the plant.

Also, the possibilities of the imaging system for quality control in food industry have been demonstrated, as the system is able to detect unwanted objects such as metal pieces or glass fragments. On the other hand, the proposed system has to be improved as the characteristics of the sample generate some false positive errors.

Finally, as it has been probed in the examples presented, the purity of the sample or the manufacturing process can be studied using THz radiation. Furthermore, the sensitivity of the system used for the measurements (TPS Spectra 3000) has been determined.

CHAPTER V

FZPL SPIRAL ANTENNA: DESIGN OF A DUAL BAND ANTENNA BASED ON FRESNEL THEORY

An integrated dual band detector intended to be used as a front-end for imaging applications and working at THz and IR frequencies is described in this chapter. The proposed configuration implements a spiral antenna working at sub-millimeter wave frequencies which design is based on Fresnel Zones theory. At the same time, this spiral antenna is used as Fresnel lens to focus IR power (12 μm) into an IR detector.

V.1.-Introduction

As it has been presented in the introduction (Chapter I), the situation of the THz in between the microwaves and the infrared allows to join the applications available in both frequency ranges. With the aim of proposing a detector for a THz imaging system a dual-band system is presented.

The device designed is configured for detecting in the THz range and also it works in the far-infrared (IR) wavelengths. A detector that can work simultaneously at those ranges would be very useful to take images (THz image and IR image), at the same time and saving measuring time. The combination of those images provides complementary information on the imaging object [deMaagt2006].

Instead of design a dual-band single antenna (the antenna and the detector work at two different frequency ranges), a dual-band device (with two different detectors) based on microwave techniques has been chosen. In this case, the detector for the submillimeter wave frequency range will be a spiral antenna designed for direct detection (homodyne detector). This type of antenna has been selected because its shape is very similar to a Fresnel Zone Plate Lens (FZPL) which allows focusing the IR power into the detector. Combining both characteristics, the spiral antenna and the FZPL, a dual-band detector will be obtained.

This chapter is structured as follows. Section II presents a short introduction about Fresnel Zones and Section III about spiral antennas. The design and performances of each frequency range (THz and IR) are described in Section IV. Section V explains the manufacturing process while Section VI summits the final characterization of the spiral antenna. Finally, some conclusions about the dual band detector based on FZPL are commented in Section VII.

V.2.- Classical Fresnel Zones

The Fresnel Zones concept was originated in the early XIX Century, by Augustin Fresnel [Fresnel1866], based on Huygens previous work [Huygens1690] and takes into account the space and time periodicity of light waves (electromagnetic waves). Fresnel was interested in the diffraction and interference of the electromagnetic waves as he used a geometrical construction of zones to solve the Huygens-Fresnel integral [Guenter1990].

These zones, known as Fresnel Zones, can be applied for differently shaped surfaces [Hristov2000] [Minim 2004]. A Fresnel zone is one of the (theoretically infinite number) concentric ellipsoids which define volumes in the radiation pattern of a (usually) circular aperture. Fresnel zones result from diffraction by the circular aperture [ITS1996].

These ellipsoids are represented in a two-dimensional planar structure by concentric rings, as it is shown in Fig. 5.1. Using this planar surface, a Fresnel Zone Plate Lens (FZPL) can be implemented. The FZPL is a planar structure which focus the power as a three-dimension lens. To focus the power, some considerations about the phase of the electromagnetic beam through the structure have to be taken into account.

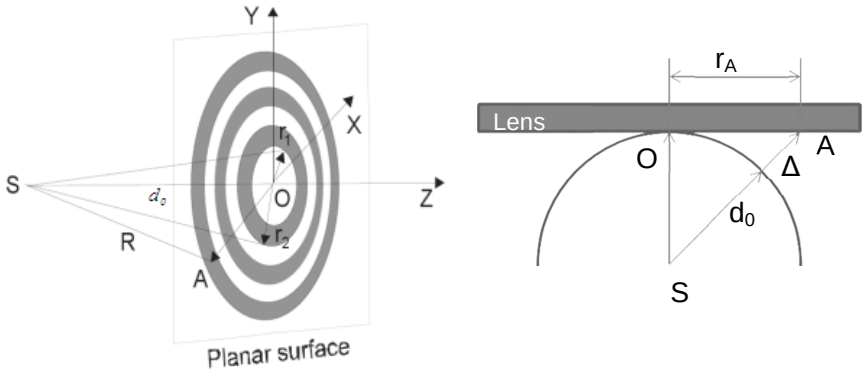

Fig. 5.1. Schematic of the Fresnel Zones [Minin2010]

The phase of the wave on the surface determinates the Fresnel Zones and it can be calculated using rays theory. As it is depicted in Fig. 5.1, from the point A, a triangle is created using SO (segment between Point

Source, S, and point O, Fig 5.1) and SA rays (segment between Point Source, S, and point A, Fig 5.1) and the radius r_A (the radius from O to A). The electrical path difference between SA and SO is the phase at point A. As the wave source is spherical, all rays from the source (S) to the surface have the same path difference if the radii from O are constant. These circles of constant radius and centered in O, fix the constant phase zones.

Taking these considerations into account, the phase at an arbitrary point on the surface, point A; is determined by:

$$\Delta = R - d_0 = \sqrt{r_A^2 + {d_0}^2} - d_0 \tag{5.1}$$

$$\phi = \frac{2\pi\Delta}{\lambda_0} \tag{5.2}$$

Where d_0 is the distance SO, R is the distance SA, r_A is the radius from O to A and Δ is the difference in path lengths between SO and SA. ϕ is the phase and λ_0 is the wavelength in the free space [Minin2010].

It is possible to define sub-zones where the phase difference between them is less than 360º [Hristov2000] [Minin2004]. It is common to break the 360º phase range in half so that each sub-zone covers 180º. It means that the contribution of the power of each odd zone has a phase difference of 180º from the even zone.

If this destructive interaction is eliminated, i.e. covering the even zones with metal to avoid transmission through them, a gain at the focus point (focus gain) can be obtained, as the structure is working as a lens (Fig. 5.2). This structure is called Fresnel Zone Plate Lens (FZPL). Note that similar results can be achieved if the odd zones are blocked.

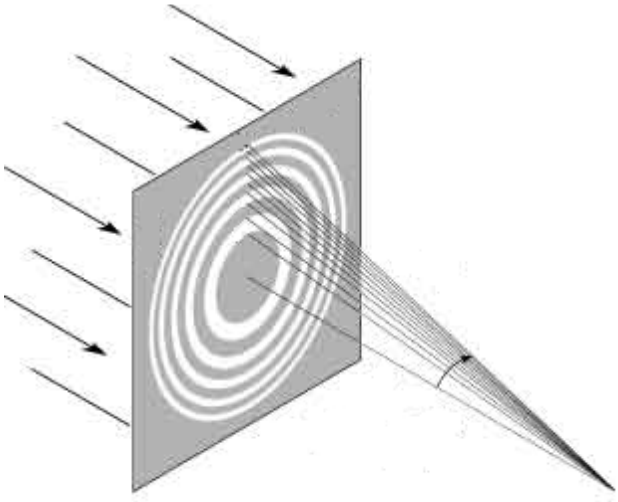

Fig. 5.2. Focalization of a Fresnel Zone Plate Lens [Attwood1999]

V.2.1.- Circular Fresnel Zones

The structure described previously is named as a circular Fresnel zone plate (CFZP). It consists of concentrically ring zones (in this case, even zones are blocked, odd zones are transparent) and works as a lens (Fig. 5.2). Note that the rings cover the subzones with a phase difference of 180º respect the unblocked zones [Guo2010].

When a plane wave is incident on a Fresnel lens, each point in a transparent zone acts as a secondary source (Huygens's diffraction principle). This secondary source emits a spherical wave. If the radiation from all the transparent zones arrives in phase within $\pm\pi/2$ range at the focal point, there will be constructive interference. This requires that the distance from the focal point to the edge of successive zones be integral multiples of the wavelength, as it is descripted by the following equation:

$$R_m = d_0 + \frac{m\lambda}{2} \tag{5.3}$$

Where R_m is the distance from the focal point to the m-th zone boundary, d_0 is the focal length and λ is the wavelength. The radius r_m of the m-th Fresnel Zone is given by:

$$r_m = \frac{m\lambda}{2}\sqrt{1+\frac{4f}{m\lambda}} \tag{5.4}$$

Once the Fresnel Zones have been calculated, they can be optimized in order to obtain a higher gain. Instead of blocking some zones, several changes (profiles) can be designed for phase-correction (see Fig. 5.3). These profiles eliminate the contribution of the blocked zones (profiles (a) or (b)) or added it to the total re-radiated power (profile (c)) changing the phase difference [Collings2008].

Although symmetry (Eq. (5.1) and Eq. (5.2)) defines the Fresnel Zones as circular, for some applications it could be useful to have rectangular or square FZPLs. For example, square FZPLs are better suited to design an array of rectangular pixels. Also, they are easier to design, as the transitions between two Fresnel Zones are easier using square pads than spiral pads. An approximation used for change from a circular FZPL to a square FZPL is fixed by [Alda2010]

$$x_m = \frac{\left(md_0\frac{\lambda_0}{n}\right)^{1/2}\sqrt{\pi}}{2} \tag{5.5}$$

Where *m* is the Fresnel Zone index, d_0 is the focal length, λ_0 is the wavelength at working frequency, *n* is the refractive index of the substrate and x_m is the half side of the adapted square FZ.

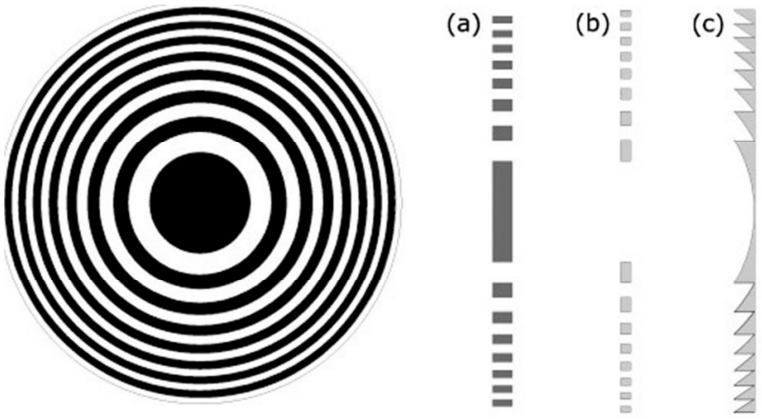

Fig. 5.3. Left images shows a Fresnel Zone with (a)the odd zones blocked, (b) even zones blocked and (c) phase-correction profile [Collings2008]

V.3.- Spiral Antenna

A spiral antenna is shaped as a two-arm (or more) spiral [Johnson1961] and they were first described in 1956 [William1976]. Spiral antennas belong to the class of frequency independent antennas which operate over a wide range of frequencies due to polarization, radiation pattern and impedance of such antennas remain unchanged over large bandwidth [Mayes1992].

These antennas are inherently circularly polarized, due to the turns of the arms and present low gain (although arrays of spiral antennas can be used to increase the gain). Furthermore, spiral antennas are reduced size antennas with its windings making it an extremely small structure and they are classified into different types (see Fig. 5.4); such as Archimedean spiral (which is the most popular configuration and it is shown in Fig. 5.4a), square spiral (Fig. 5.4b), log-periodic spiral (Fig. 5.4c) or equiangular spiral (Fig. 5.4d)

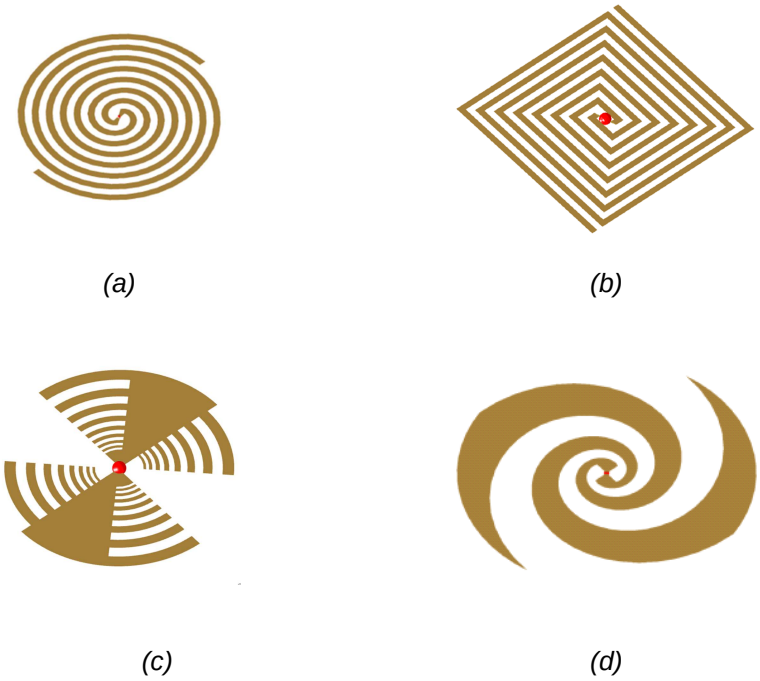

(a) *(b)*

(c) *(d)*

Fig. 5.4. Several shapes of spiral antennas: (a) Archimedean, (b) square, (c) log-periodic and (d) equiangular [CST].

Taking into account some of the schemes presented in Fig. 5.4, the shape of an Archimedean spiral antenna is very similar to a Fresnel Zone Plate Antenna. Thus, it is possible to modify the FZPL with the double purpose of detecting THz radiation (as a spiral antenna) and focusing the IR radiation (as a FZPL).

Note that due to this modification, the FZPL will provide lower focus gain as some blocked zones will be connected. Also, the spiral antenna will have lower gain and worse matching as the spacing between the arms of the spiral is fixed by FZ theory. On the other hand, this device (FZPL transforming into a spiral antenna) will comply with both characteristics: it will act as IR lens and as sub-millimeter wave antenna.

V.4.- Design of the Fresnel Zone Plate Lens Spiral Antenna.

This section describes the design of the FZPL, the transformation into a spiral antenna and the final performance, as a FZPL in the IR range, and as a spiral antenna in the submillimeter wave range.

V.4.1.- Frequency Range

This device is designed for imaging applications which require the combination of THz-IR information so those are the frequency range of operation chosen for the design of the device. Also, the availability of IR detectors at the selected frequency contributes to fix the wavelength. Taking these facts into account, a wavelength of 12 μm (25 THz) has been chosen for the design of the FZPL. Note that this band is typically used for IR astronomy applications [Ipac].

Furthermore, the operational frequency selected for the submillimeter wave range was 450 GHz because, at this frequency, it is able to design, fabricate and measure at the laboratories of the Antenna Group at UPNA.

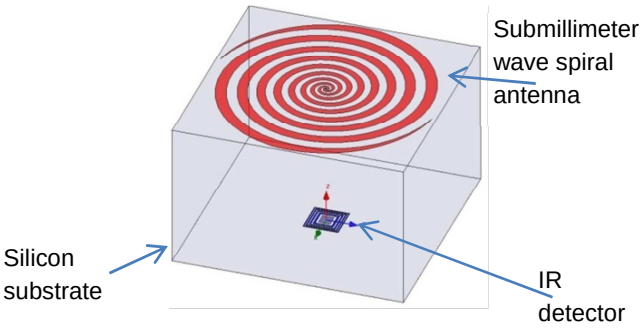

Fig. 5.5. Scheme of the proposed THz-IR receiver

V.4.2.- Scheme of the Detector

The proposed dual band configuration consists of a planar spiral antenna and an IR detector, as it is shown in Fig 5.5. Both of them are mounted in a Silicon (Si) substrate. The spiral antenna placed on the top of

the Si substrate is designed to operate at sub-millimeter wave frequencies, in particular around 450 GHz [Brown2006]. This antenna results from a conversion of an ideal FZPL to a quasi-spiral antenna. As FZPL, it focuses, at the same time, the incoming IR radiation into the IR detector, which is placed at the bottom of the Si substrate, as depicted in Fig. 5.5.

V.4.3.- Study of the Fresnel Zone Plate Lens

The radii of the Fresnel zones used for FZPL design are calculated using Eq.(5.6). They depend on the wavelength, the material used as substrate and the focal distance.

$$r_m = \left(m d_0 \frac{\lambda_0}{n} \right)^{1/2} \tag{5.6}$$

where r_m is the radius of the m-Fresnel Zone, m, the Fresnel Zone index, d_0 is the focal distance, λ_0 is the wavelength at working frequency and n is the refractive index of the substrate, in this case silicon. The obtained circular Fresnel zones are shown in Fig. 5.6.

The circular rings of the Fresnel lens must be transformed into a quasi-spiral in order to act as sub-mm wave antenna. This must be done by connecting adjacent rings. These connecting sections degrade its performance as antenna, and therefore, the use of a square FZ lens seems to be more suited for the final design.

Therefore an approximation to square FZ was carried out using Eq. (5.7)

$$x_m = \frac{r_m \sqrt{\pi}}{2} \tag{5.7}$$

where r_m is the radius of the circular FZ and x_m is half length of the adapted square FZ. The shape of the square FZs obtained by Eq. (5.7) are depicted in Fig. 5.7.

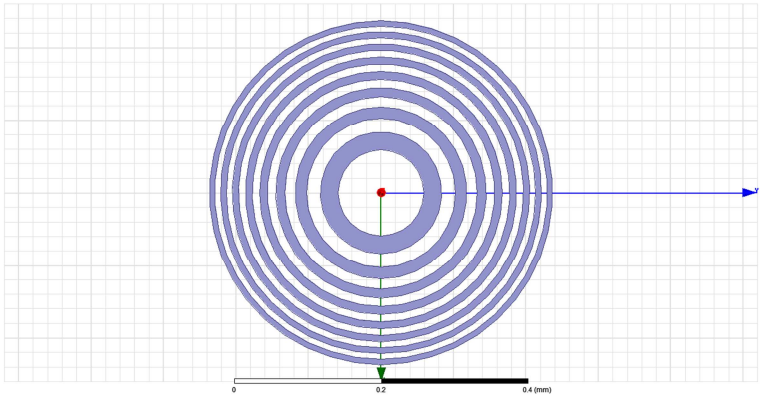

Fig. 5.6. Circular Fresnel Zones (16 FZ are shown)

On the other hand, it is important to point out that a Schottky diode will be used as sub-mm wave detector. Therefore, its size will impose a size condition in the implementation of the FZPL. In fact, the size of the first Fresnel Zone has to be at least 100 x100 μm^2 (for a circular area larger than 10000 μm^2, r_1> 57 μm) in order to have enough space to place a Virginia Diode Inc. (VDI) [VDI] diode in the central point of the square spiral antenna (see Fig. 5.7). Taking this into account the Fresnel lens is designed for an ideal focal distance of 1000 μm using Eq. (5.6). Note that for d_0=1000 μm, the radius of the first Fresnel zone is r_1=59.2 μm which is larger than 57 μm, as required. Finally, using Eq. (5.7) to calculate the size of the square Fresnel Zone, a value of x_1= 52.5 μm is obtained. The relationship between the values to the ideal radius of the FZ and the ones of the square zones are presented in Table 5.1. The latter ones will be used to design the Fresnel Zone Plate sub-mm wave antenna.

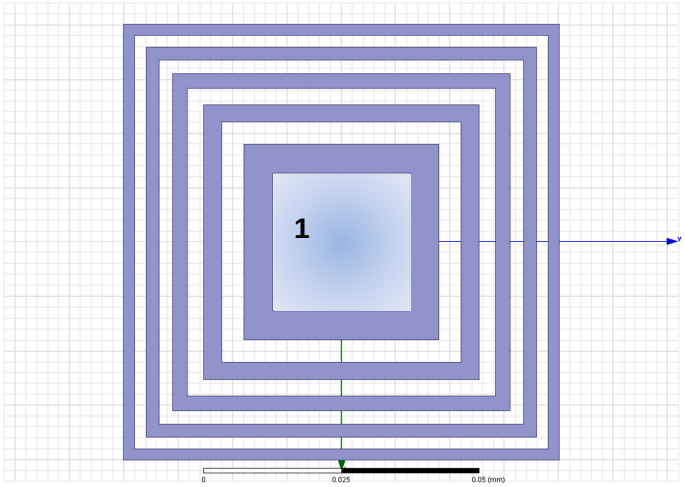

Fig. 5.7. Square Fresnel Zones and (1) the blue zone represents the area for diode placing

The values corresponding with the ideal radius of the FZ and the calculated side of the square zones are presented in Table 5.1. These square Fresnel Zones are used to develop the Fresnel Zone Plate Antenna.

Note that the metal rings used for the implementation of the FZPL are obtained subtracting to the n-th even zones the previous odd zone (zone n-1). Thus, the external radius of each metal FZ corresponds with the radius of the even zones and the inner radius is given by the odd zones. Following this procedure, the minimum spacing obtained is 6.7 μm and the maximum spacing is 21.7 μm.

Due to the use of a finite number of FZ and the square shape of the spiral sub-mm wave antenna, both its focusing performances as IR lens and its radiation properties at sub-mm wave frequencies will be affected. Simulation results and theoretical expression [Mao2009] [Sato2011] show that sharp corners (bends) have more influence than smooth circular paths on the propagation of electromagnetic fields due to reflections caused by the change in the characteristic impedance that they introduce. On the other hand, smooth circular paths do not introduce this change, and therefore, the transformation from circular to square FZ affects the performances of the FZPL working as submillimeter-wave antenna. These effects will be analyzed in the next sections.

Table 5.1. Fresnel Zones size

Zone number	Circular FZ	Square FZ
	Radius (μm)	*Half size(μm)*
1	59.2	52.5
2	83.8	74.2
3	102.6	90.9
4	118.5	105.0
5	132.5	117.4
6	145.1	128.6
7	156.7	138.9
8	167.5	148.5
9	177.7	157.5
10	187.3	166.0
11	196.5	174.1
12	205.2	181.8
13	213.6	189.3
14	221.6	196.4
15	229.4	203.3
16	236.9	210.0

V.4.4.- Fresnel Zone Plate Lens IR performances

Once the limitation of the first Fresnel zone has been considered in the design, it is necessary to determine, the real focal distance of the FZPL taking into account the use of square spirals; and the focal gain obtained as a function of the number of Fresnel zones used in the design of the sub-mm wave square spiral antenna.

In order to check its IR performances when square FZ are employed, seven different square antenna configurations were analyzed; all the even cases from 4 to 16 FZ. The study was carried out with Ansys-HFSS software [Ansys]. Note that no more than 16 Fresnel zones have been implemented in the design due to the resolution of the available photolithographic process in our laboratory, which is limited to 5 µm. With these constrains, it is difficult to fabricate the 18FZ-antenna because the gap in between the 16^{th} FZ and the 18^{th} FZ is close to 6 µm.

An incident plane wave (negative z-axis propagation direction) has been used as an excitation. The analysis has been limited to linear polarization, so that, the incident plane wave has a linear polarization along the x-axis. Note that due to its symmetry the FZPL presents a similar behavior for both linear polarizations (x-axis and y-axis). Furthermore, in order to have enough simulation resources (memory requirements), only a thin region of the structure has been simulated, as it is depicted in Fig. 5.8 (lower row). This region is a transversal cut, defined from the lens central axis (x-axis) to the external face (the final volume simulated is 400 µm x 5 µm x 1000 µm). In this case, symmetry boundary conditions have been defined in both side faces. This approach is adequate to determine the properties of the structure as a lens.

Fig. 5.8 (upper row) shows a comparison between the performances of the sub-mm wave antenna acting as lens implemented with ideal (i.e. circular) FZ and with square FZ operating at the IR frequency (12 µm). This Figure shows the propagation of the electric field magnitude through the Si substrate where the lens is implemented. In both cases, 16 FZs are used to form the sub-mm wave antenna.

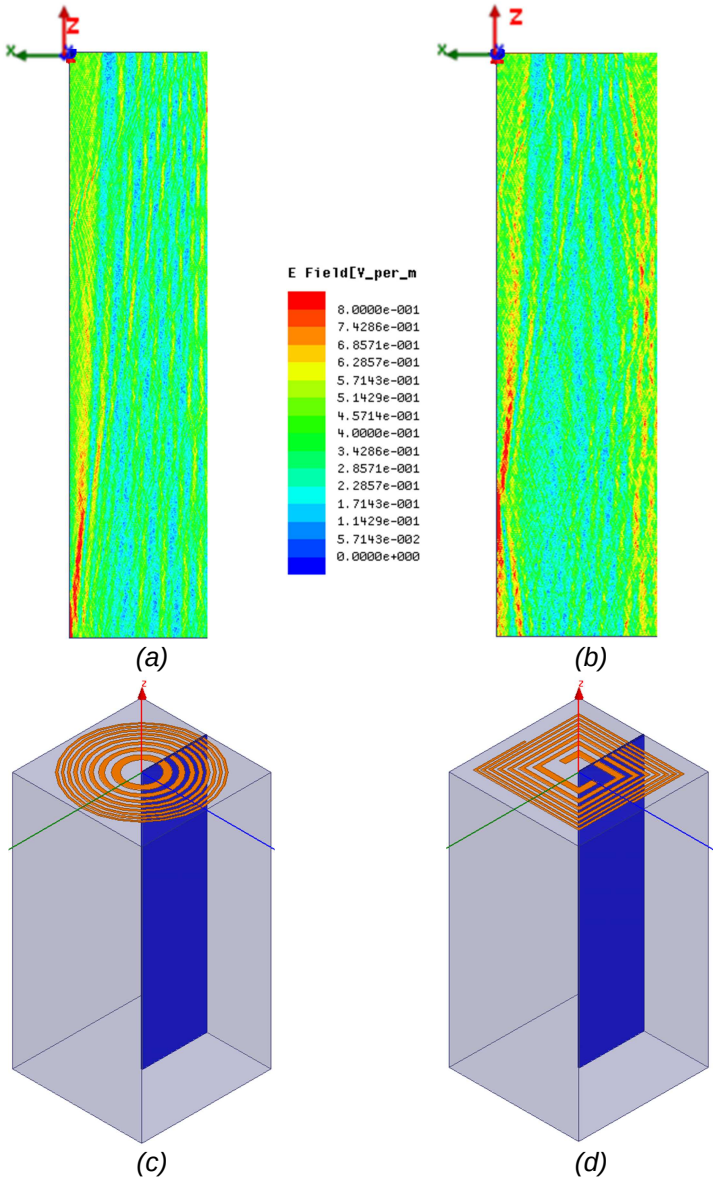

Fig. 5.8 Comparison of the magnitude of the electric field between (a) 16 circular Fresnel zones and (b) 16 square Fresnel zones. Note that only half of the substrate is depicted in the upper row. In the lower row, a full view of each device is depicted The simulation slice is marked in blue.

The magnitude of the electric field focuses at 1000 µm for the case of circular Fresnel zones (Fig. 5.8a). On the other hand, square Fresnel zones (Fig. 5.8b) focus the electric field at a shorter distance. This result shows an important shifting of the focal distance due to the transformation from circular to square of the Fresnel zones.

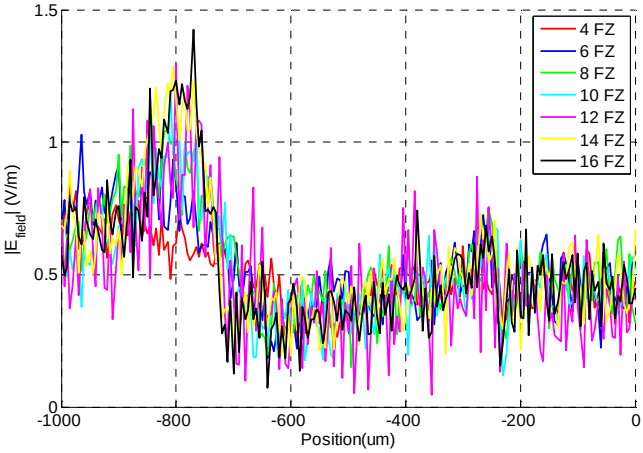

(a)

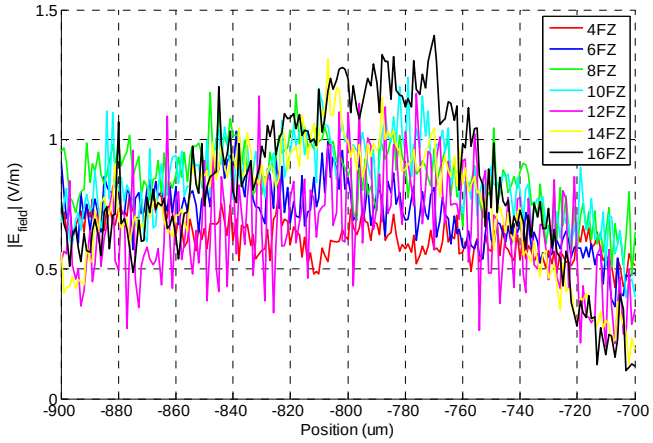

(b)

Fig. 5.9 (a) Amplitude distribution of the electric field within the silicon substrate. 0 µm corresponds with the sub-mm wave antenna position. λ=12 µm and (b) zoom around 800 µm.

Note that there is a small fraction of the electric field that is not focused by the FZPL, as it is clearly depicted in Fig. 5.8b and will be studied later on. Note that the value of this fraction decreases as the area of the FPZL increases.

To analyze the displacement of the focal point and to obtain the focal distance for the square FZ, the maximum amplitude along the z-axis of the magnitude of the electric field within the silicon substrate for the different number of analyzed FZs is depicted in Fig. 5.9. Note that 0 μm position represents the point where the FZPL is located.

As it is depicted in Fig. 5.9, it can be concluded that the maximum of the electric field using square Fresnel zones is concentrated around 800 μm instead of the ideally expected 1000 μm. This result clearly shows that the focal distance is affected by the shape of the FZs.

On the other hand, if the number of FZ is increased, the magnitude of the electric field at the focus point is expected to be increased. For the sake of representation, the ratios between the magnitude of the electric field at the focal point for the cases with and without a FPZL are calculated (Gain Factor). This ratio is defined as follows;

$$\mathrm{GF} = \frac{\text{Electric Field with FPZL}}{\text{Electric Field without FPZL}} \tag{5.8}$$

This Gain Factor at the bottom of the Si substrate (along the x axis for z=800 μm) for each analyzed square FZPL is shown in Fig. 5.19. Note that the same substrate volume (400 μm x 5 μm x 800 μm) has been used for each simulation. Excitation and boundary conditions (incident plane wave and symmetry boundary conditions) are the same as in the previous cases. The FZPL formed by 16 Fresnel zones exhibits the maximum Gain Factor which is close to 4.5 (the magnitude of the electric field obtained using the FZPL is 4.5 times higher than the case of no lens). For the sake of simplicity, only FZPLs made with 12, 14 and 16 FZs are depicted.

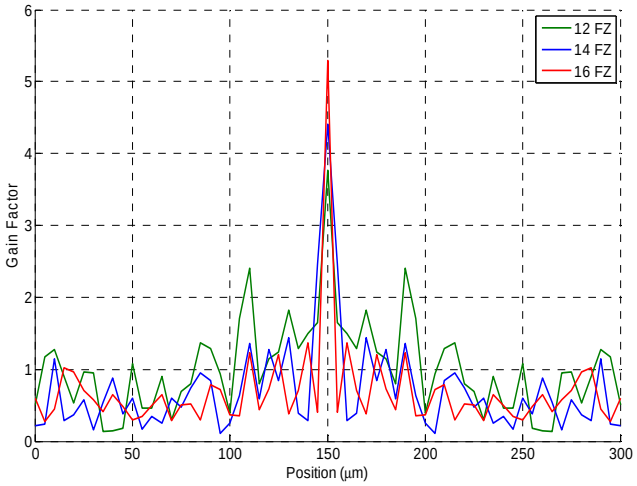

Fig. 5.10 Gain Factor value as function of the number of square Fresnel Zones along the x axis for z= 800 µm. Operational wavelength of 12 µm.

Note that the small fraction of the electric field flowing at the edge of the Si substrate which was previously noticed (Fig. 5.8b) has no influence in the focalization gain, as seen in Fig. 5.10, i.e. the maximum value of the power is concentrated around 150 µm.

Fig. 5.11 summarizes the maximum value of the Gain Factor for each FZ antenna analyzed. Furthermore, the maximum value of the theoretical Gain Factor for circular Fresnel Zones has also been depicted for comparison issues. For this analysis, the number of FZ has been extended from 4 FZ to 50 FZ.

In this figure, it can be noted that the circular FZL theoretical Gain Factor (CFZ) is higher than the square FZ (SFZ) for all the cases. Note that both curves present a similar trend. It is important to remark that the focal distance for the SFL is 800 µm. This value, as the number of Fresnel zones increases, saturates to a constant value; i.e., 6.5 and 5.7 for CFZ and SFZ zones respectively. Note that its trend will depend on the focal distance [Minim2004].

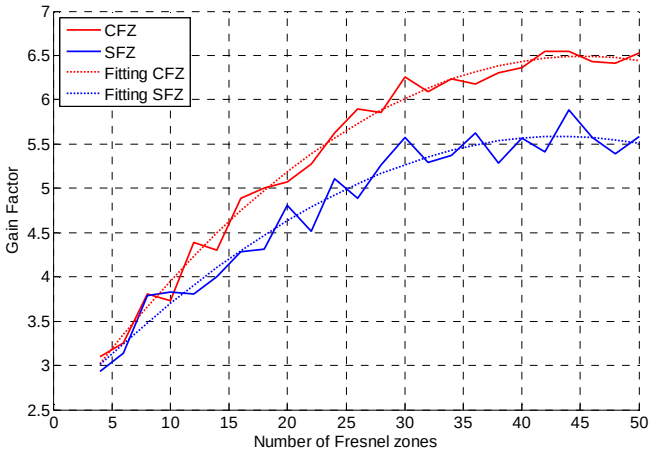

Fig. 5.11 Gain Factor for each antenna at 800 µm. CFZ is calculated for Circular Fresnel Zones and SFZ for square Fresnel Zones.

V.4.5.- Submillimeter wave antenna performances

In the previous section, the study of the focal distance and the GF for the Fresnel Zone Plate Lens, working at 12 µm has been presented. In this section, the study of its performance as a sub-millimeter wave antenna, operating at 450 GHz, is described.

For analyzing the sub-mm antenna radiation performances, a lumped port has been defined as excitation port (central square area in Fig. 5.12). This excitation models the diode that will be used as detector in the final implementation. Note that the size, W, and the input impedance, Z_{diode}, of the simulated diode are obtained from a commercial VDI diode [VDI] (Z_{diode}=15 Ω at 427 GHz, W=30 µm, and a total length of 150 µm).

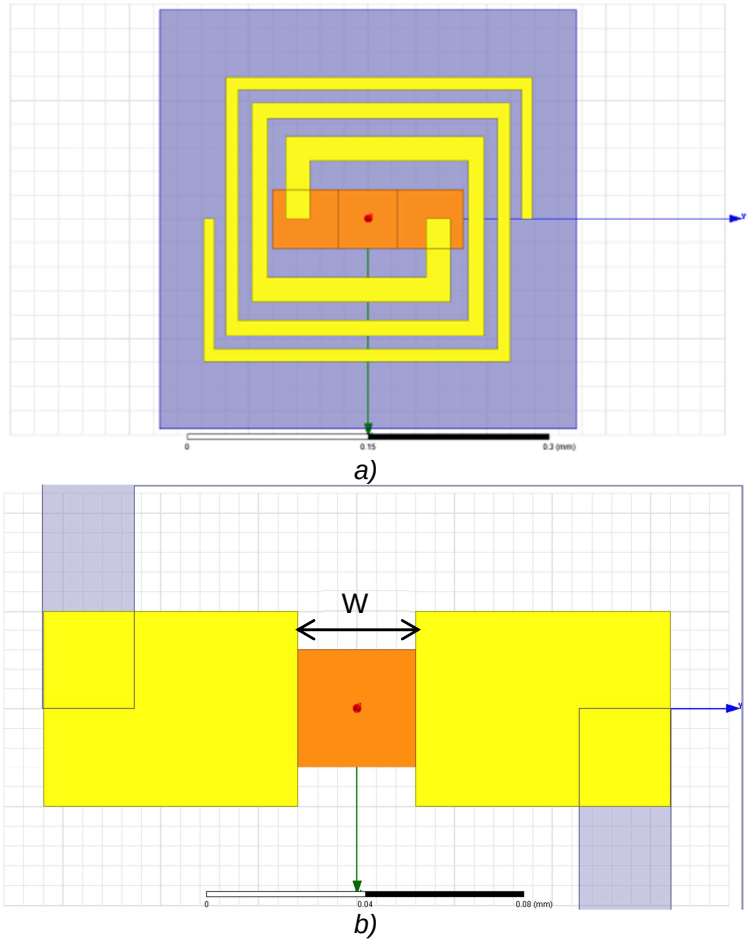

Fig. 5.12 (a) Sub-millimeter Wave Antenna (yellow) and detector diode (orange). Note that the spiral antenna depicted is made with 8 FZ. (b) Detail of the diode model.

To simulate the model, symmetric boundary conditions have been defined in both side faces to replicate an infinite array [Ansys]. Furthermore, the top/bottom faces of the structure have been designated as radiation boundary condition. The size of the Si substrate is 500 µm x 500 µm x 800 µm.

In Fig. 5.13, the reflection coefficient (S_{11} parameter) of the square spiral antenna is depicted. The values for the 4-6FZ antennas have been not included due to their low GF value. The results show two antenna working bands, around 210 GHz and 427 GHz.

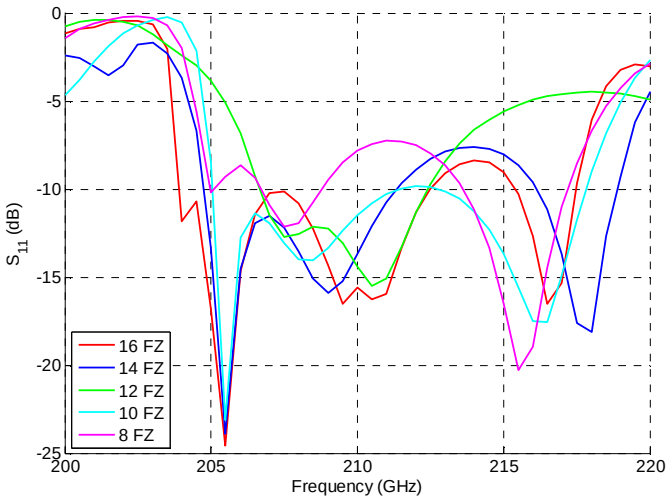

(a)

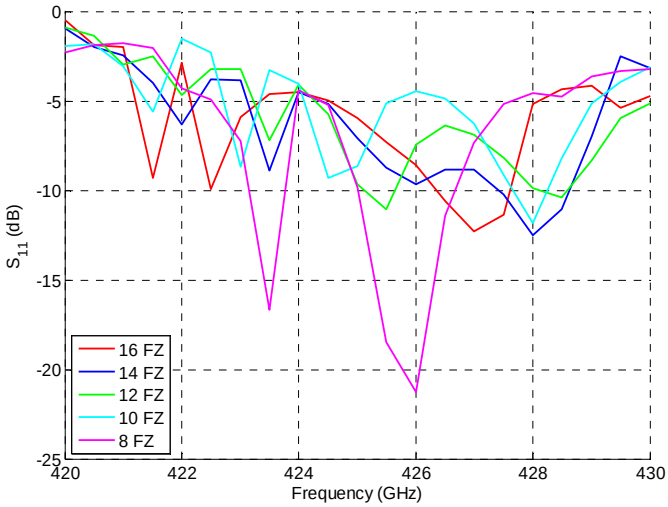

(b)

Fig. 5.13 (a) S_{11} parameter of the sub-mm wave antennas working at 210GHz and (b) 427GHz

The simulated S_{11} parameter is better than -5 dB from 424 GHz to 430 GHz for most of the simulated sub-mm square spiral antennas. In the lower band, the scattering S_{11} parameter is better than -7 dB from 205 to 215 GHz.

Finally, the directivity pattern of the square spiral antennas is shown in Fig. 5.14. Note that due to the fact that the sub-mm wave antenna is placed on a Si substrate, more power is trapped by the substrate than radiated to free space, and therefore, the back radiation is higher than the front one (see Theta=±180º versus 0º).

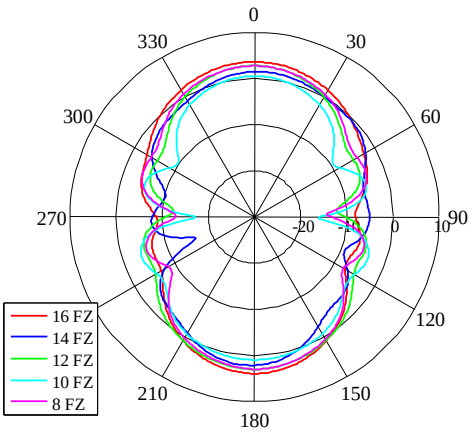

Fig. 5.14 Directivity of the square antennas at 427 GHz.

The maximum value of the directivity is obtained for the case of 16-FZ (the largest antenna analyzed in this frequency range) square spiral sub-mm antenna, which has a value larger than 3 dBi.

This FZ-spiral antenna is the unit cell of the final array. In order to check the coupling between the antennas in the array configuration, a study of this parameter has been performed. Fig. 5.15 shows the scheme used to characterize the coupling. Note that the substrate size is 1000 µm x 1000 µm x 800 µm for each antenna under study.

The study has been performed in using a 2x2 array, as it is shown in Fig. 5.15.

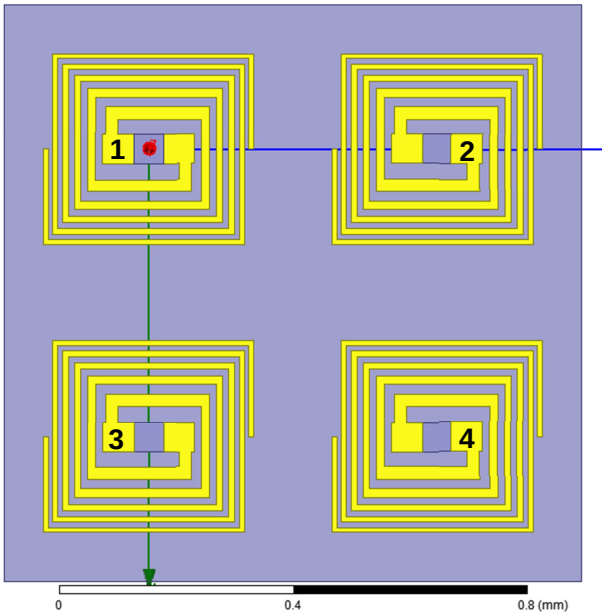

Fig. 5. 15. Scheme of the structure for the coupling study. In this case, a pair of 12-FZ antenna is represented.

In this case, a simulation of the transmission parameter S_{21} (S_{31} for the second pair and S_{41} for the third pair) has been achieved for each pair of antennas (pairs (1,2), (1,3) and (1,4), see Fig. 5.15). The obtained results are depicted in Fig. 5.16. As it can be seen, the best case is obtained for 4-FZ antenna (the separation between antennas is the highest). Furthermore, the S_{21} parameter is better than 25 dB for each case. Note that pairs (1,2)-(3,4); (1,3)-(2,4) and (1,4)-(2,3)provide the same results.

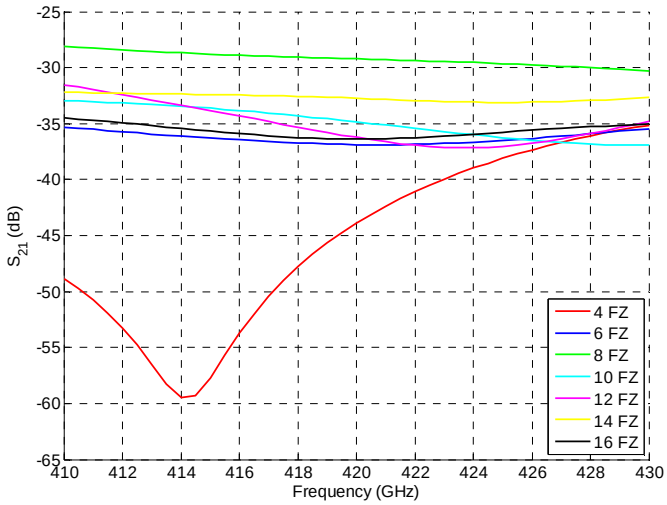

(a)

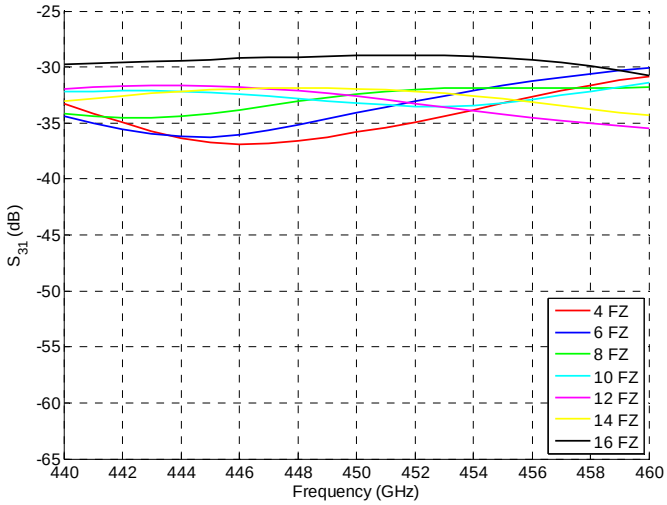

(b)

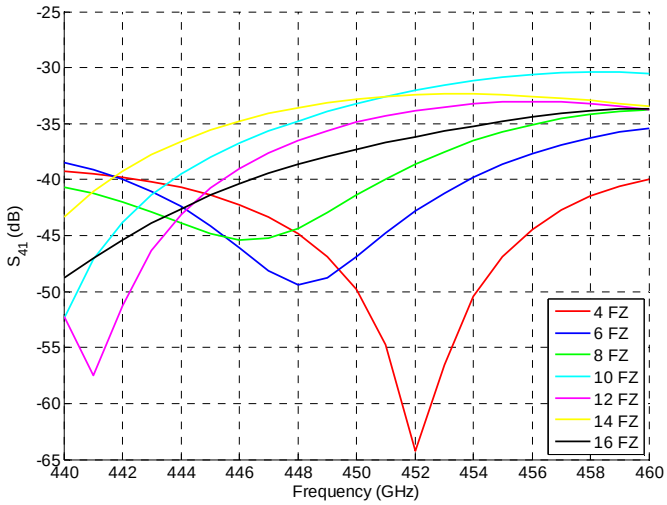

(c)

Fig. 5.16. Coupling study for each pair of antennas (a) coupling between antennas 1 and 2, pair (1,2), (b) coupling between 1 and 3, pair (1,3) and (c) coupling between 1 and 4, pair (1,4) as it is descripted in Fig. 5.15.

V.5.- Fabrication Process

As it has been commented in Section V.4.2, a silicon wafer (thickness 800 µm) was used as a substrate. Due to the size of the spiral antennas, a photolithography process has been followed for the manufacturing of the spirals [Jaeger2002]. A short description of this process is related below:

First of all, the silicon wafer (Si) is cleaned using isopropyl alcohol (Fig. 5.17a). Secondly, the wafer is covered with a photoresist (PR) by spin coating. The photo resist-coated wafer is then prebaked to drive off the excess photoresist solvent (Fig. 5.17b). Thirdly, a photomask (PM) is allocated in the wafer. Note that the PM has the drawing of the spiral antenna and it has been specifically designed for be used in this process.

After prebaking, the PR is exposed to a pattern of intense light (Fig. 5.17c). The exposure to light causes a chemical change (cure process) that allows some of the PR to be removed by a special solution, called developer (Fig. 5.17d). Note that the chemical agent removes the PR zones cured by the light (the areas that were not protected by PM).

Next step is the sputtering process. Atoms of gold are launched to the PR-covered wafer (the PM has been removed) and they totally cover the area, as it is shown in Fig. 5.17e. Finally, the photoresist is no longer needed and it must be removed from the substrate. This process usually requires a liquid (resist stripper), which chemically alters the PR so that it no longer adheres to the substrate. Note that this process also eliminates the gold layer that covers the PR (see Fig. 5.17f). On the other hand, it can also eliminate some parts of the gold circuit.

An example of the manufactured spiral antenna is depicted in Fig. 5.18. Note that the design of an 8FZ-antenna has been used for the fabrication. This antenna has a minimum spacing (10 µm) between the arms of the spiral. As the resolution of the manufacturing process is 5 µm this antenna presents no problems to fabricate it.

Note that for this dissertation, only the design, fabrication and measurement of the THz frequency range antenna has been presented because the IR range is out of the scope of this thesis.

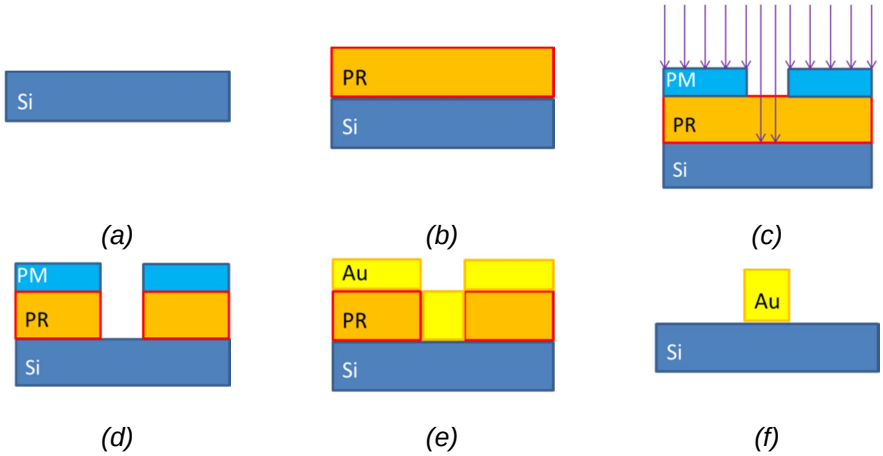

Fig. 5.17. Scheme of the photolithography process followed for the spiral antenna fabrication

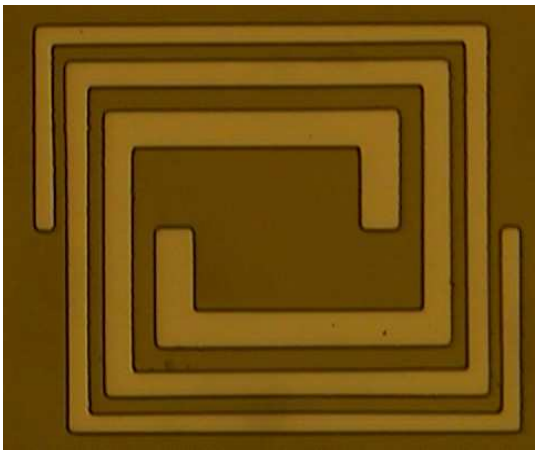

Fig. 5.18. Single Spiral manufactured using the process related.

Table 5.2 shows the differences between the manufactured antennas and the simulated antennas. These deviations can have influence on the resonance frequency described in Section V.3.1 and a little shifting can appear in the measurement results.

Table 5.2. Comparative of Fresnel Zones size

Zone number	Manufactured (um)	Theoretical (um)
1	114	105
2	164.7	148.4
3	194.5	181.8
4	232.9	210
5	253.2	234.8
6	282.1	257.2
7	297.8	277.8
8	326.4	297.0

In order to measure the resonance of these spiral antennas, a 2x5 array (2 rows, 5 columns) has been manufactured, following the same photolithography process described previously. A photo of the array is shown in Fig. 5.19

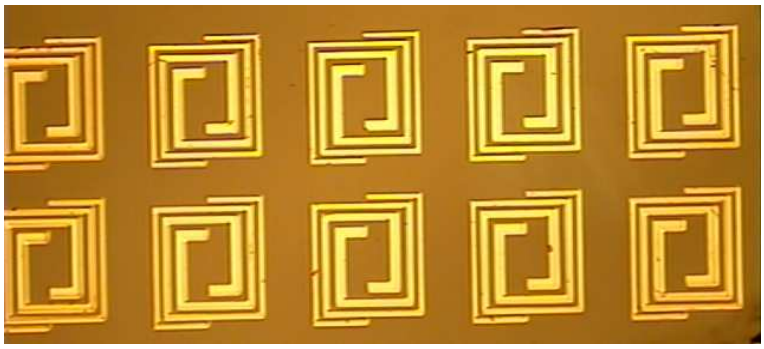

Fig. 5.19. Photo of an array 2 x 5 of spiral antenna.

V.6.- Measurement Results

Some measurements of the array shown in Fig. 5.19 were carried out using two characterization devices, a network analyzer (descripted in Chapter II) and the TPS Spectra 3000 (described in Chapter III). Also, in order to eliminate the influence of the manufacturing process, two different arrays were measured.

V.6.1.- TPS Spectra 3000 results

Firstly, a description of the measuring setup implemented is presented to illustrate the measurements performed in the laboratory. Fig. 5.20a shows a silicon wafer that will be used as a reference. In this case, an incident THz pulse passes around the sample. A small fraction of the power of the pulse is reflected and it goes back to the emitter. The highest fraction of the power is transmitted and arrives to the detector. Note that the absorbed power is not depicted.

In Fig. 5.20b, the same silicon wafer is turned. In this case, the reflected power is deviated due to the angle of incidence. The transmitted power, as in the previous case, arrives to the detector but it has a lower level than in case (a).

On the other hand, the sample under test depicted in Fig. 5.20c is the array of spirals (they are represented in yellow). This case is very similar to the case (a). Most of the power is transmitted to the detector and a small fraction is reflected to the emitter.

Finally, in Fig. 5.20d the sample is turned. In this case, there is also a re-radiated power (green power) due to the resonance of the spiral antenna Note that the transmitted power is even lower than the case of Fig. 5.20b, due to the re-radiation of the incident power.

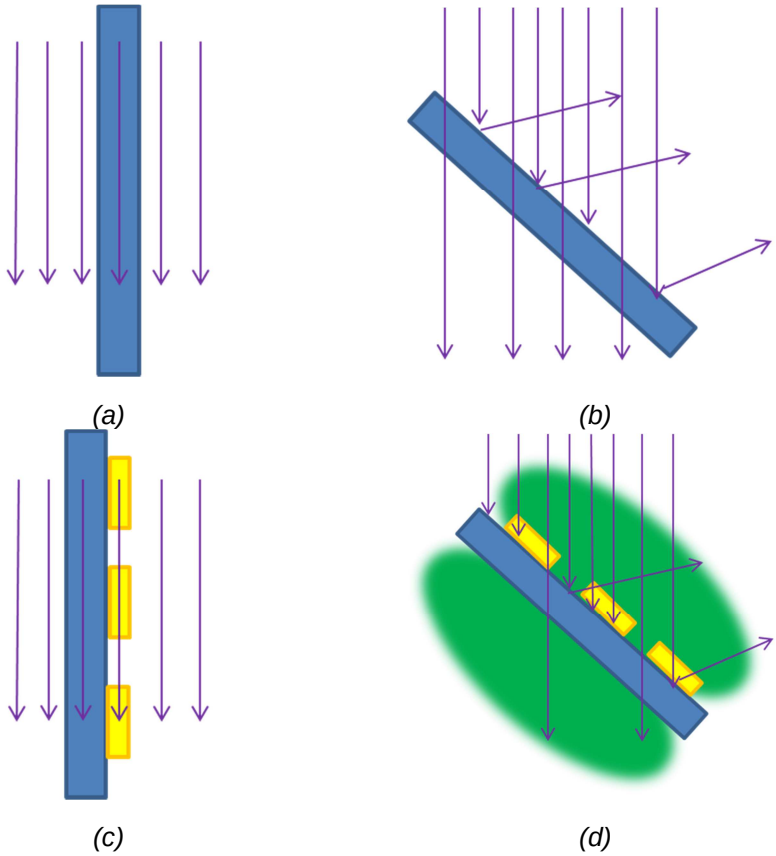

Fig. 5.20. Scheme of the measuring setup proposed

Using the schemes illustrated in Fig. 5.20d, a minimum in the transmitted power is expected to be achieved. The obtained results are presented Fig. 5.21 and Fig. 5.22. In Fig. 5.21, the transmittance of the spiral array (setup configured as in Fig. 5.20c) is depicted. It is easy to corroborate that there is no peaks or valleys with this configuration.

On the other hand, Fig. 5.22 shows the transmittance for the case of the rotated sample (see Fig. 5.20d). In this case is easy to observe a decrease in the transmittance value and also, some clear valleys appear at 0.55 and 0.8 THz.

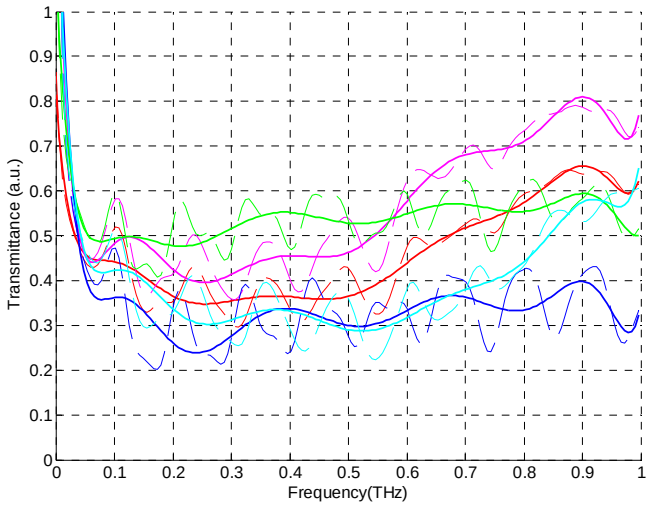

Fig. 5.21. Transmittance through the array using TPS Spectra 3000 corresponding with the configuration descripted in Fig 5.20c

Note that the graphs in Fig. 5.21 and Fig. 5.22 represent several measurements (represented with a dotted line). Furthermore, the ripple in those figures is due to the resonances in the substrate. To show the trend of the measurement, a fitting curve has been obtained for each one (represented with a solid line). These valleys (0.55 THz and 0.8 THz) appear at the frequencies where the incident power is re-radiated, as it is described in Fig 5.20d.

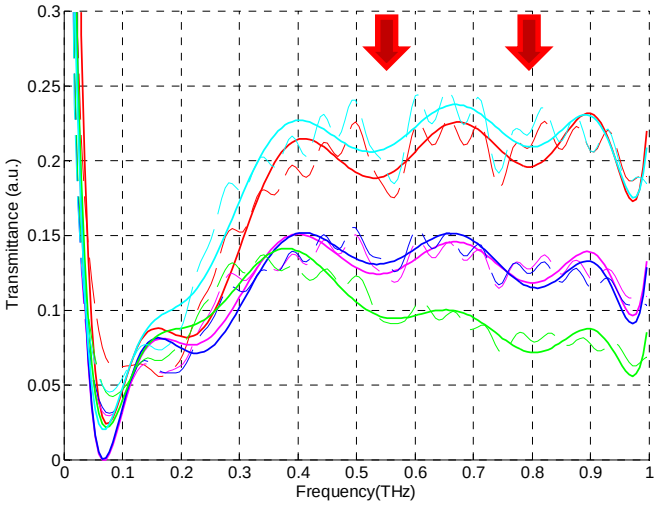

Fig. 5.22. Angular incident of the array using TPS Spectra 3000. The configuration it is descripted in Fig 5.20d

V.6.2.- Network Analyzer results

Once these results have been obtained using the TPS Spectra 3000, a similar measurement setup has been performed using the network analyzer (it has been described in Chapter II). In this case, the VNA extenders for the band 0.325-0.500 THz have been used to measure the devices.

As in the case previously related, the arrays of spiral antenna have been characterized in transmission with an angular incident (θ_i) of the THz beam. A photo of the implemented setup is depicted in Fig. 5.23a, and a simplify scheme is also shown (Fig. 5.23b)

The measures can be influenced by the distance between the VNA extender emitter and the sample (d_1), the distance between the sample and the detector (d_2) and the incident angle (θ_i). Both distances have influence in the standing wave which can appear between the extenders and the angle of incident modifies the level of the detected power, due to the gain of the spiral antennas.

The measured magnitude is the S_{21} scattering parameter which has been descripted in Chapter II. It is expected that the incident power over the

spiral antennas will be re-radiated by the spiral antennas themselves. (Note that this power will be radiated as it is shown in the gain pattern (see Section V.3.4, Fig. 5.14). The obtained measurements are depicted in Fig. 5.24

(a)

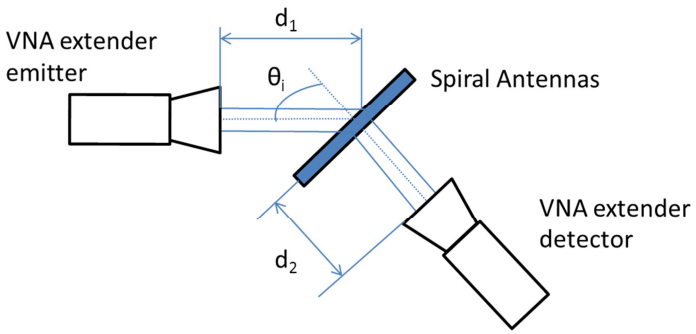

(b)

Fig. 5.23. (a) Photo of the measuring system based on the network analyzer and (b) a simplify scheme of the setup

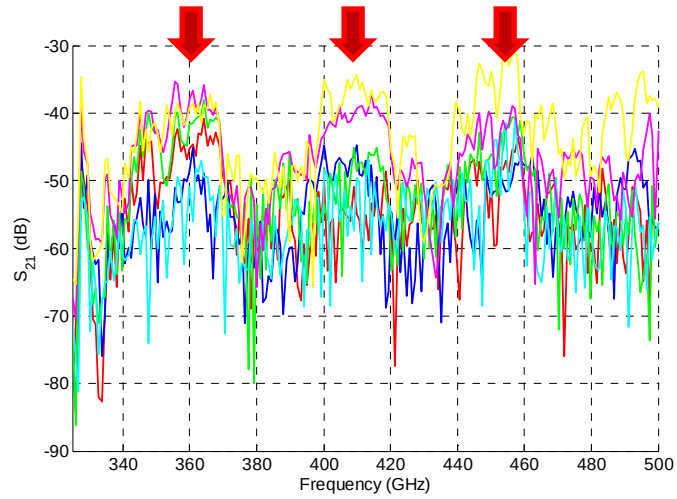

(a)

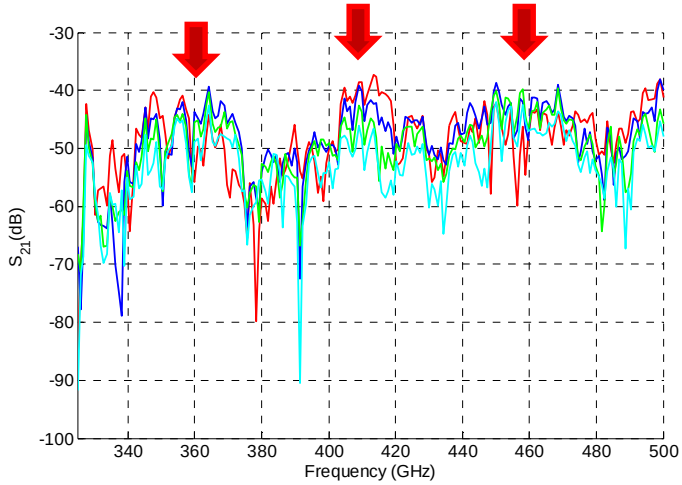

(b)

Fig. 5.24. Transmitted power varying (a) the distance d_1 and (b) the distance d_2 measured by the network analyzer

In this Figure (Fig 5.24), a variation of both distances d_1 and d_2 is shown. In Fig. 5.24a, the distance d_1 is varied (from 50 to 75 mm in steps of 5 mm) and in Fig. 5.24b, d_2 is the distance modified (in the range 30-45 mm and a step of 5 mm). Several graphs in both figures represent different measurement distances.

As it is depicted, it is possible to detect three zones of maximum transmission (360, 410 and 450 GHz). The spiral antennas resonate and radiate power. In order to test that these resonance frequencies are produced by the array, a simulation of the measurement setup using Ansys-HFSS [Ansys] is presented. In this case, an angular incident plane wave has been used as an excitation. The transmitted power through the structure (S_{21} parameter) is represented in Fig. 5.25. Furthermore, in order to clarify that result, a smoothing (represented by a red line in Fig. 5.25) and a fitting curve have been obtained.

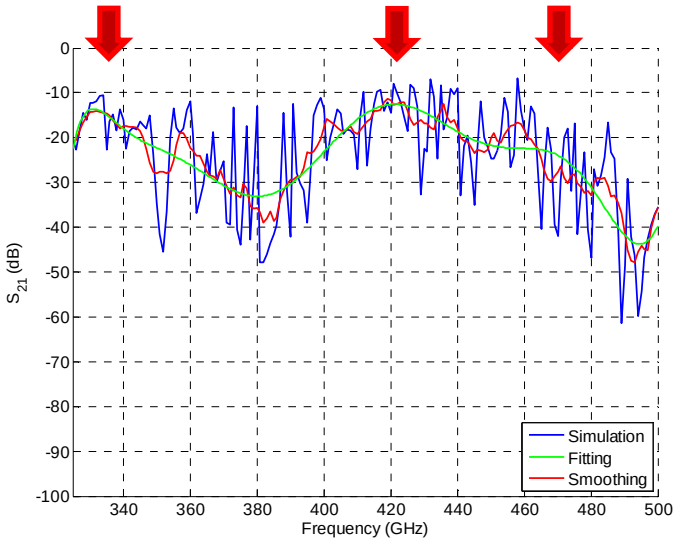

Fig. 5.25. Simulation result of the transmitted power with angular incident

It is possible to check that there are also three frequencies where the S_{21} is maximum, around 335, 420 and 470 GHz. These resonance frequencies are similar to the measured frequencies (360, 410 and 450 GHz). The discrepancies come from the fabrication tolerances.

V.7.- Conclusions

The design of a submillimeter wave antenna, operating at 427 GHz, which also acts as Fresnel Zone Plate Lens at IR frequencies (12 μm), has been presented. The sub-mm wave antenna resulted from a transformation of a Fresnel Zone Plate Lens. This device has been designed intended to be used as a front-end for imaging applications which requires THz-IR information.

The influence of the number of FZ used to implement the submillimeter wave antenna on the IR power focalization has been studied for the case of linear polarization. As the number of FZ forming the sub-mm wave antenna increases, the gain factor also enlarges. A Gain Factor improvement of 4.5 times has been obtained with the implementation of 16 FZs. Furthermore, the shifting of the focal point due to the square shape of Fresnel Zones used to implement the Fresnel Zone Plate Antenna has also been investigated.

The antenna exhibits reasonable performances operating at sub-mm wave frequencies with a S_{11} parameter below -5dB (from 424 to 428 GHz) and a directivity of 3.6 dBi (f=427 GHz). Also, the coupling between the antennas is lower than 25 dB.

Furthermore, some arrays 2x5 of spiral antennas have been manufactured using a photolithographic process. These arrays have been characterized for the band 0.060 - 1 THz. Note that the obtained results in the laboratory agree with the simulation results.

CHAPTER VI

CONCLUSIONS AND FUTURE RESEARCH LINES

This chapter relates the conclusions of this dissertation and the future research lines.

VI.1.-Conclusions

In this thesis, the capabilities of the THz radiation to detect and identify several materials have been presented. Very interesting compounds (such as explosives) have been characterized by the implemented systems. Furthermore, a THz-IR front-end based on Fresnel Theory has been designed and manufactured.

In Chapter II, a THz imaging system based on a network analyzer has been implemented, in order to obtain THz active images, in transmission/reflection configuration for this dissertation. This system allows measuring the magnitude and/or the phase in frequency and time domain.

This system is able to measure from 0.090 THz to 0.500 THz with a resolution of 1 mm (f=0.220 THz). The maximum size of the image is 500 mm x 700 mm with a minimum dynamic range of 95 dB and sensitivity better than -105 dB for the overall bandwidth.

The implemented characterization systems descripted in Chapter III have demonstrated the capabilities of the THz radiation to identify unwanted or dangerous objects inside the sample under test, by the use of a non-invasive, non-destructive and non-ionizing radiation.

As a reference for the implemented systems, a TPS Spectra 3000 has been used. This system (a THz-TDS) measures in the 0.060 - 3.5 THz frequency band. Typically, it is used for small samples (composed by one material), powder samples or liquid samples. Secondly, a measuring system based on a network analyzer has been implemented for the band 0.090 - 0.500 THz. This system obtains the refractive index and the permittivity of the sample by measuring the scattering parameters. This system characterizes thick samples, typically in reflection configuration. Finally, a null-ellipsometry system has been implemented to measure the refractive index at 1 THz. It is based on the TPS Spectra 3000 but it can measure thin or thick samples in a reflection scheme.

The identification of the energetic materials or explosives is a very important topic for counterterrorist fight. This thesis has characterized explosives before and, for the first time, after the detonation. They have been characterized using the TPS Spectra 3000 and the ellipsometry system, by its absorbance and its refractive index. The obtained absorbance spectrum allows identifying these compounds even after the detonation

(using the THz-TDS system). Thus, these results provide new possibilities for explosive identification to security forces to fight against terrorist actions. Furthermore, the measured refractive index shows that both systems, THz-TDS and ellipsometry system can be used for the characterization as they provide similar results. Note that they have different requirements about the measurement (sample size or bandwidth).

In Chapter IV; in order to illustrate the capabilities of those systems, applications for agriculture and food industry have been commented. THz radiation has demonstrated that a sensor based on this technology can determine the water content evolution of a leaf, using reflected power. Furthermore, THz images can detect unwanted object in a quality control system. In addition to these results, a study of the influence of the manufacturing process and the additives in the absorbance spectrum of several explosives has been presented.

Finally, as it has been presented in Chapter V in this dissertation, a new dual-band device that works at THz frequencies and at IR range has been designed. This detector combines the measurements in the THz (at 427 GHz) and the IR region (25 THz), to save measuring time and also to join the applications of both domains.

The use of Fresnel theory in this device allows obtaining a Gain Factor of 4.5 times, for an antenna made with 16 FZ. Note that this value has been obtained working in the IR range (25 THz). Furthermore, this antenna presents a S_{11} parameter better than -5 dB and a directivity of 3.6 dB at 427 GHz.

VI.2.-Future research lines

In Chapter III, a null-ellipsometry system working at 1 THz has been presented. This system is able to characterize the sample under test by its refractive index, using the change in the polarization state and the incident angle. The natural prolongation of this work is to design a vary-incident angle ellipsometry system. That evolution allows to measure samples with different size/diameter. Furthermore, the development of an in-house tool for an automatic measuring of the polarization state will generate an improvement in the quality of the results.

In order to generate a final broadband characterization system, the ellipsometry system can be improved to measure in the overall bandwidth, not at only one single frequency (spectroscopic ellipsometry). This bandwidth expansion allows a better comparison between THz-TDS and the ellipsometry system. Also, if the sample under test is composed by several layers, the thickness of each layer, and its refractive index could be obtained.

Chapter IV has shown some applications of the THz waves. In this case, the post processing of the images appears as a promising field for quality control systems. Also, filling the actual THz databases, as it has been shown with the explosives, is a very important topic. For instance, some results have actually been obtained in the Antenna Group measuring some drugs and medicines.

In Chapter V, a dual band detector has been designed. In this case, due to the scope of this thesis, the IR detector has been not taken into account. The next step consists on introducing the IR detector and also the sub-millimeter wave detector in order to obtain the final device. Furthermore, some images should be taken to show its capabilities.

APPENDIX A

ABSORBANCE OF THE EXPLOSIVES

For the sake of simplicity, only one absorbance for each explosive has been presented in Chapter III. Thus, the rest of the figures achieved are depicted below.

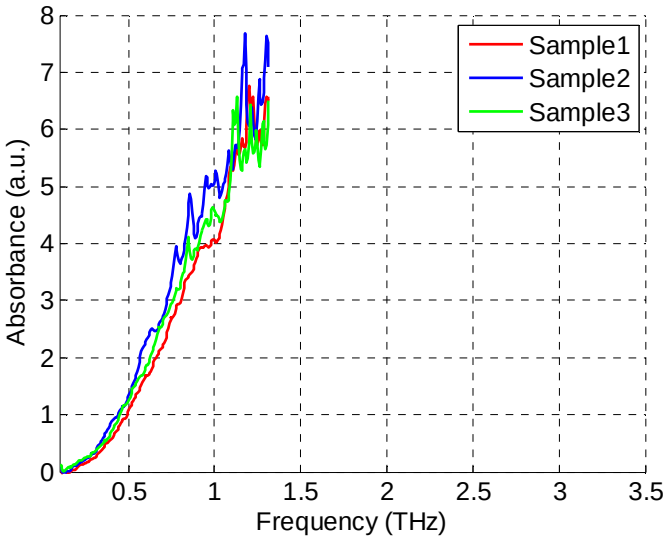

Fig. A.1. Absorbance the Gun Explosive

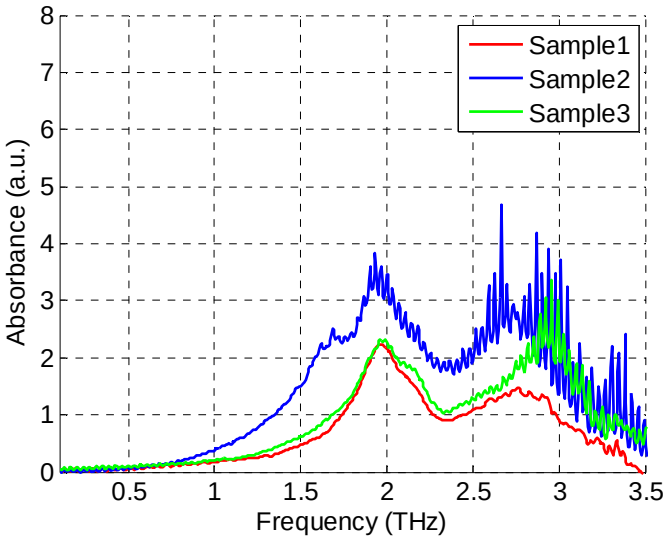

Fig. A.2. Absorbance of the PETN

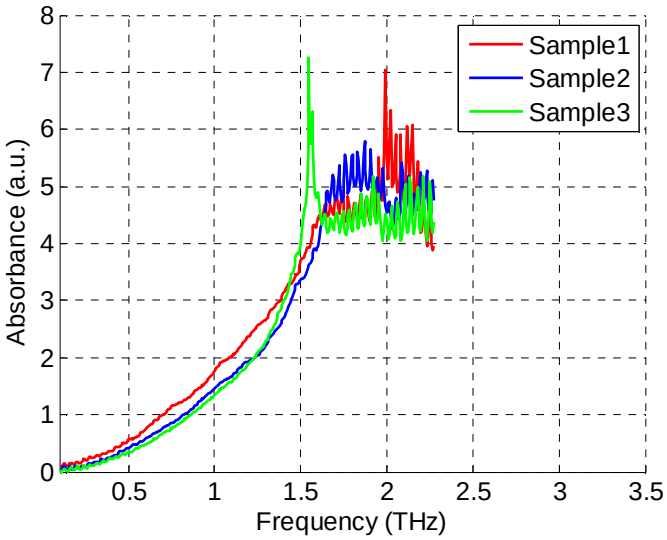

Fig. A.3. Absorbance of the Mine Gunpowder

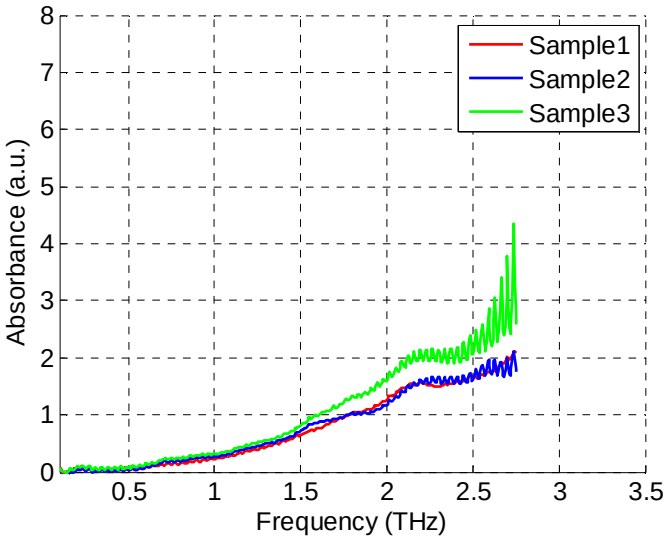

Fig. A.4. Absorbance of the TNT

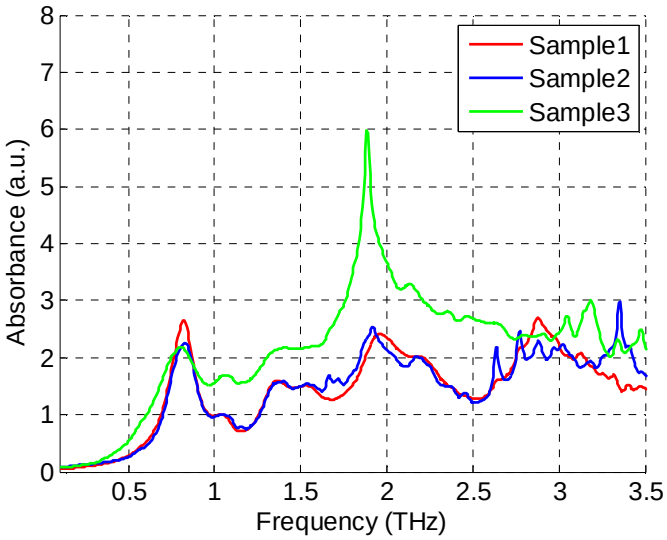

Fig. A.5. Absorbance of the RDX

As can be seen in all figures, the trend of the samples is very similar in each type of explosive. Also, the peaks related in Section III.4.1.2 are placed at the same resonance frequencies.

Note that the values for sample 3 in each case are different from the other samples. It is important to remark the fabrication process. First of all, 300 mg of sample and 750 mg of PE are weighted and mixed. Then, 350 mg of the mix sample+PE are used for the first pellet (Sample 1). This process is done another time to obtain the second pellet (Sample 2). Finally, the rest of the mix sample+PE generates the last pellet (Sample 3).

This process has been following in order to obtain two pellets with a weight of 350 mg each one. The last pellet weights less than 350 mg, due to the losses during the manufacturing process. These losses are related with the differences shown in this Appendix.

On the other hand, although the levels are quite different, the resonance peaks are placed at the same frequencies. Thus, the manufacturing process of the pellet does not affect to the characterization study.

APPENDIX B

FREQUENCY SELECTION FOR AGRICULTURE APPLICATION

An extended study of the frequency influence in the water control evolution for an agriculture application is presented in this Appendix.

B.1.- Introduction

In Section IV.II, an agriculture application of the THz radiation at f=0.215 THz is shown. In this appendix, an extended study focused on the frequency influence is presented. To obtain the results presented in Section IV.II, 401 images using both configurations (transmission and reflection) have been achieved. Instead of analyze all frequencies; three representative frequencies have been evaluated: the lower frequency (0.140 THz), a resonance frequency of water (0.180 THz) and the highest frequency of the range (0.220 THz).

These frequencies have been selected due to some characteristics: it is expected that the water content of the sample will be easily detected in a characteristic frequency (resonance frequency) of water. Also, the resolution has been determined as a critical parameter for an imaging system. Thus, f=0.220 THz provides the best resolution of that frequency range. Finally, the lower frequency (f=0.140 THz) has been studied to cover the available bandwidth and to study the obtained results with a lower resolution.

B.2.- Analysis of the results

The measurement procedure has been realized as it is descripted in Section IV.II. In this section, only transmission images are depicted. As can be seen, in all the analyzed frequencies the same trend is detected. The first day (t_0, upper row in Fig. B.1, Fig. B.2 and Fig. B.3), the leaf presents zones with low transmission level. These zones are related with the areas of the leaf which accumulate water (veins and leaf stack). Also, it is possible to detect that the level of transmitted power through these zones grows during the second and the third day.

For each frequency analyzed, the detected power increases its value each 24 hours, as it is summarized in Table B.1, Table B.2 and Table B.3. It is remarkably that, in the three cases, the average transmitted power has been duplicated, as it can be also concluded from Table 4.1 (f=0.215 THz). For each frequency, that power is increased in lineal way while, as it is depicted in Fig. 4.1, this variation cannot be detected in visible spectrum.

Table B.1. Average Transmitted Power Trough the Leaf at f=0.140 THz

Time *(Hours)*	Value *(Modulus)*
0	0.274
24	0.372
48	0.602

Table B.2. Average Transmitted Power Trough the Leaf at f=0.180 THz

Time *(Hours)*	Value *(Modulus)*
0	0.269
24	0.381
48	0.605

Table B.3. Average Transmitted Power Trough the Leaf at f=0.220 THz

Time *(Hours)*	Value *(Modulus)*
0	0.241
24	0.366
48	0.579

Note that in Fig B.3 it is possible to identify some parts of the leaf (leaf veins and leaf stack) while in Fig B.1 it is not as clear that in this case, due to the lower resolution achieved at this frequency (Section II.2.1).

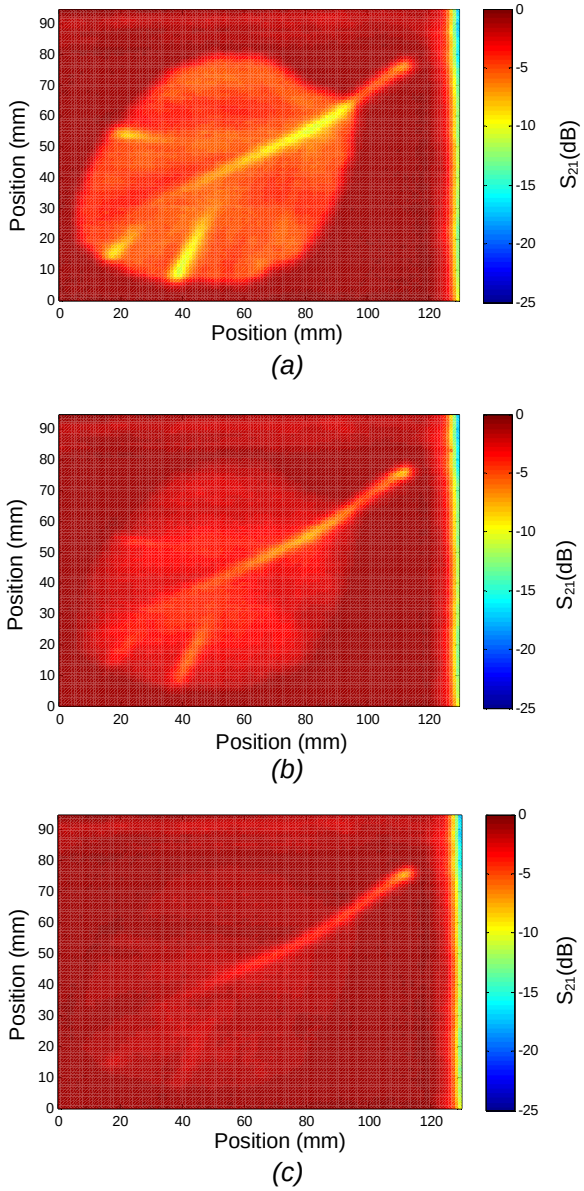

Fig. B.1. (a) THz image in transmission of the first day, t_0 (b) THz image 24 hours later, t_0+24 hours. (c)THz image 48 hours after the day of cutting, t_0+48 hours obtained at f=0.140 THz

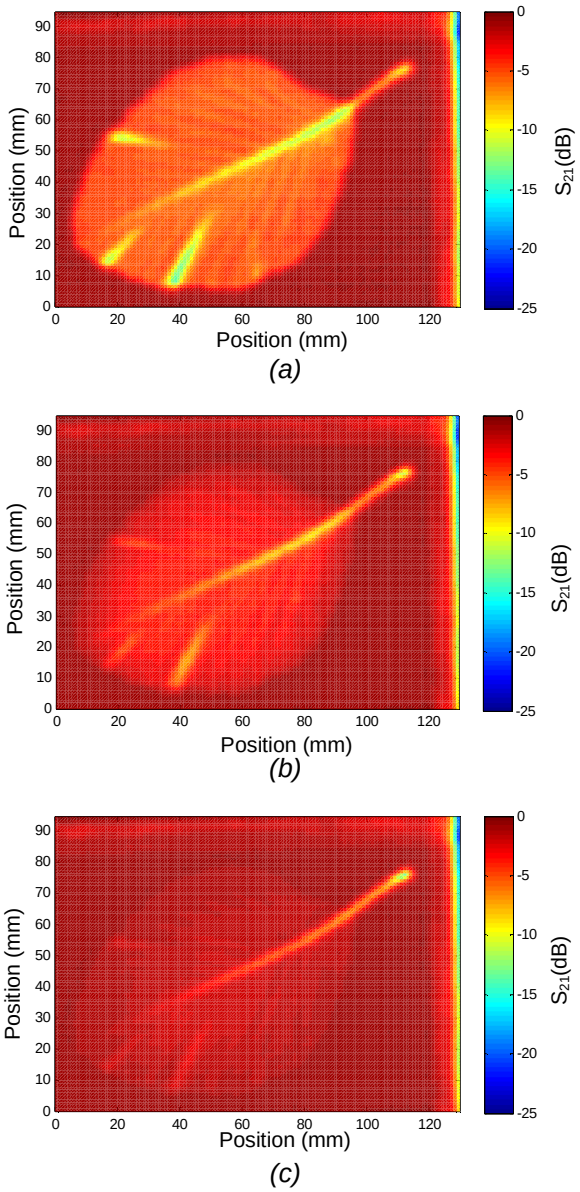

Fig. B.2. (a) THz image in transmission of the first day, t_0 (b) THz image 24 hours later, t_0+24 hours. (c)THz image 48 hours after the day of cutting, t_0+48 hours obtained at f=0.180 THz

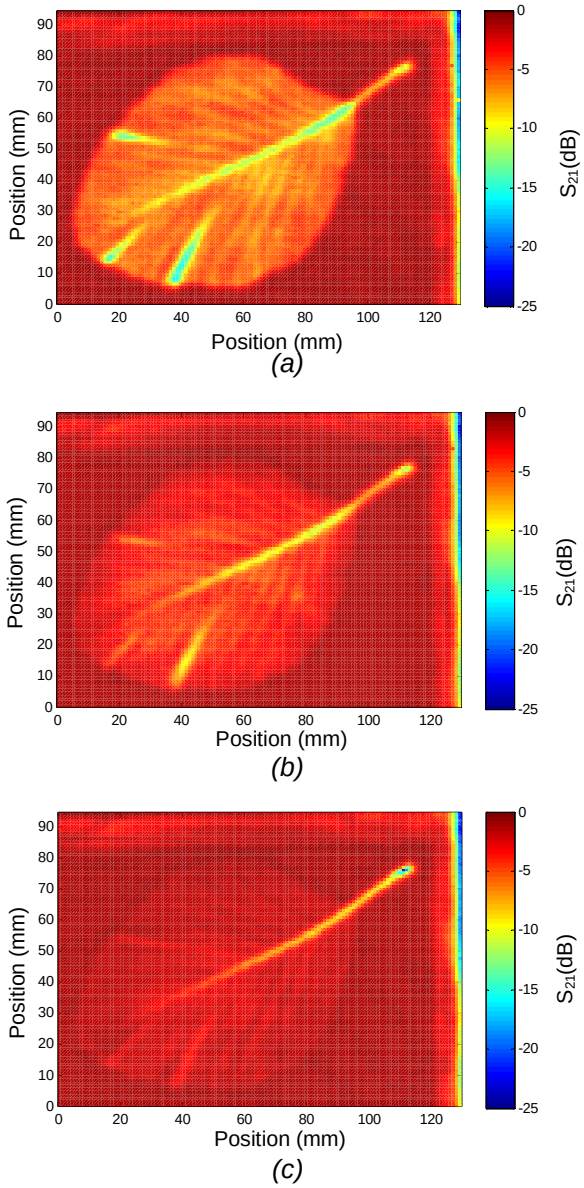

Fig. B.3. (a) THz image in transmission of the first day, t_0 (b) THz image 24 hours later, t_0+24 hours. (c)THz image 48 hours after the day of cutting, t_0+48 hours obtained at f=0.220 THz

Note that Table B.2 presents higher values than the other cases. This difference is due to the resonance of the water. (This frequency, f=0.180 THz was selected because the water spectrum presents a resonance peak).

In order to clarify the imaging results, a single point analysis has been realized, as it is described in Section IV.2.2. Selected points are display in Fig. 4.4 and summarized in Table B.4, Table B.5 and Table B.6.

Table B.4. S_{21} parameter (dB) achieved during the first day (t0)

Position	f = 0.140 THz	f = 0.180 THz	f = 0.220 THz
	(dB)	*(dB)*	*(dB)*
Leaf Border	-4.631	-4.786	-4.69
Leaf Stack	-8.285	-10.258	-12.032
Control	-0.8471	-0.865	-1.241

Table B.5. S_{21} parameter (dB) achieved during the second day (t_0+24 hours)

Position	f = 0.140 THz	f = 0.180 THz	f = 0.220 THz
	(dB)	*(dB)*	*(dB)*
Leaf Border	-2.353	-2.932	-2.931
Leaf Stack	-5.640	-7.080	-9.790
Control	-0.883	-0.900	-1.146

Table B.6. S_{21} parameter (dB) achieved during the third day (t_0+48 hours)

Position	f = 0.140 THz	f = 0.180 THz	f = 0.220 THz
	(dB)	*(dB)*	*(dB)*
Leaf Border	-1.152	-1.444	-1.790
Leaf Stack	-4.200	-6.380	-8.075
Control	-0.874	-0.923	-1.110

In both sample points (leaf border and leaf stack) for all the analyzed frequencies (0.140, 0.180 and 0.220 THz) a increase in the transmitted power is obtained. The evolution of this trend is represented in Fig. B.4 (leaf border) and Fig. B.5 (leaf stack). Furthermore, the level of control point remains constant for each frequency. Note that each frequency graph has been referenced to its control value.

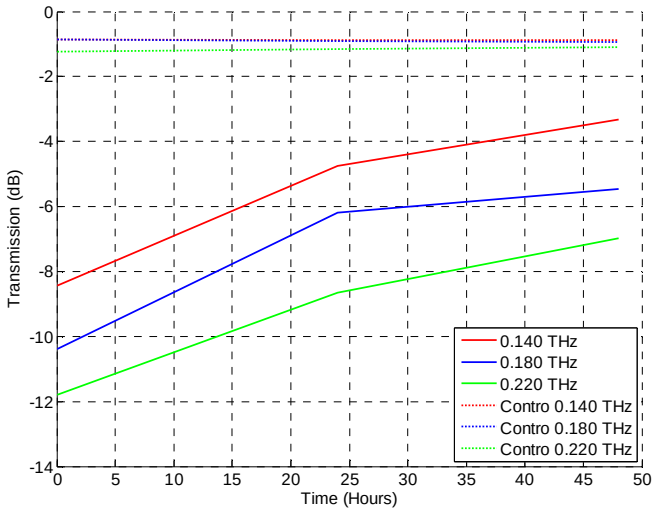

Fig. B.4. Water evolution of the transmitted signal in the leaf stack for the selected frequencies.

In Fig B.4 it is possible to analyze the evolution of the transmitted signal in the leaf stack. Note that Fig 4.6 shows the evolution of that point at f =0.215 THz. Taking into account both figures, it can be concluded that the water content evolution measured at the leaf stack presents a similar trend for all the studied frequencies although there are some differences in the first value achieved. (f=0.140 THz, S_{21}(t=0)=-9.1 dB; f=0.180 THz, S_{21}(t=0)=-11.1 dB; f=0.215 THz, S_{21}(t=0)=-14 dB; f=0.220 THz, S_{21}(t=0)=-13 dB). As in the previous case, each frequency curve is referenced to its control value.

The detected power tends to the control point value (value of reference) in each case and after 48 hours of study, this increment is around 4 dB at each operational frequency.

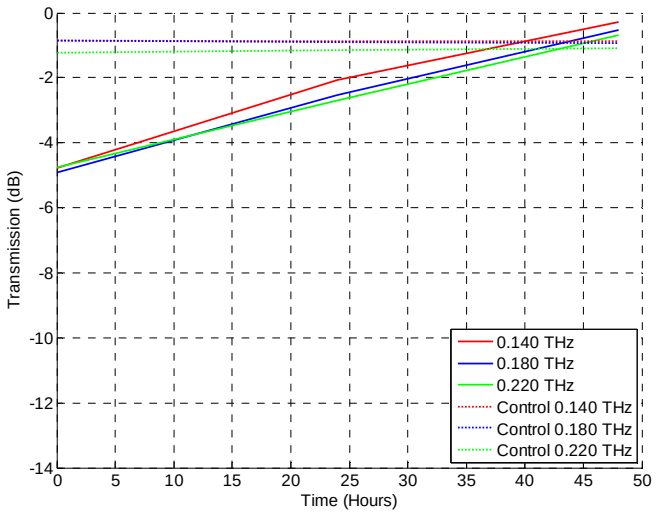

Fig. B.5. Water evolution of the reflected signal in the leaf border for the selected frequencies.

As in the previous case, the evolution of the transmitted signal measured in the leaf border is depicted in Fig B.5. Note that the evolution of the leaf border at f=0.215 THz is illustrate in Fig. 4.6. Comparing both figures, the detected signal for each frequency also presents a very similar trend.

After two days (48 hours), the detected power in the leaf border tends to the control value, as the water content level in this part is much lower. As in the case of the leaf stack, there are small discrepancies in the first point achieved (at f=0.215 THz is -6.5 dB while for the other frequencies is -6 dB).

B.3.- Conclusions

Taking these results into account, it can be concluded that the water content evolution of a leaf presents a similar trend in the range of 0.140-0.220 THz, as the study of three representative frequencies, 0.140 THz, 0.180 THz and 0.220 THz has been demonstrated.

Thus, the frequency selected for the analysis in Section IV.II (f=0.215 THz) allows to study this trend. Furthermore, this frequency presents a higher resolution (see Section II.2.1, Eq. (2.2)), as it has been demonstrated in the images shown in this Appendix.

BIBLIOGRAPHY

[Abbe1873] Abbe E. "Beiträge zur Theorie des Mikroskops und der mikroskopischen Wahrnehmung" *Archiv für Mikroskopische Anatomie* 9 (1): 413–468. 1873

[Abita1990] Abita J. L. “Microwave technology”. Johns Hopkins APL Technical Digest (Applied Physics Laboratory), 11(1-2), 145-153. 1990.

[Agilent] Agilent [Online]. Available: http://www.agilent.com

[Alda2010] González F. J. and Alda J. "Fresnel spiral antenna for detection at visible and far-infrared bands", *4th European Conference on Antennas and Propagation, EuCAP* 2010.

[Allis2006] Allis D. G., Korter T.M. ”Theoretical Analysis of the Terahertz Spectrum of the High Explosive PETN” *ChemPhysChem* Volume 7, Issue 11, pages 2398–2408, November 13, 2006

[Allis2008] Allis D. G., Zeitler JA, Taday PF, Korter TM. “Theoretical analysis of the solid-state terahertz spectrum of the high explosive RDX”. *Chemical Physics Letters*, 463(1-3), 84-89. 2008

[Alva2002] Alvarez A. “Caracterización elipsométrica de materiales dieléctricos de aplicación en el desarrollo de sensores evanescentes de fibra óptica para el sector aeroespacial”. *Ph.D. Dissertation*. Universidad Complutense de Madrid. 2002

[Ansys] Ansys HFSS 14.0 [Online]. Available: http://www.ansoft.com

[Appleby2004] Appleby R., “Passive Millimetre-wave Imaging and how it differs from terahertz imaging”, *Phil.Trans. R. Soc. Lond*. A, vol. 362, pp.379-394, 2004.

[Attwood1999] Attwood D. T., “Soft X-Rays and Extreme Ultraviolet Radiation: Principles and Applications” *Cambridge Univ. Press*, Cambridge, 1999.

[Auston1973] Auston D. H., Glass A M and LeFur P “Tunable far-infrared generation by difference frequency mixing of dye lasers in reduced (black) lithium niobate” *Applied. Physics Letters*. 23 47–8. 1973.

[Auston1983] Auston D. H. “Impulse response of photoconductors in transmission lines”. *IEEE Journal of Quantum Electronics.* Volume:19 , Issue: 4. 1983.

[Auston1984] Auston D. H. “Picosecond photoconductors: Physical properties and applications in Picosecond Optoelectronics Devices”. C.H. Lee Academic, Orlando, FL pp. 73-117. 1984.

[Bailey1998] Bailey M. C., “Design and Evaluation of an Electromagnetic Beam Waveguide for Measuring Electrical Properties of Materials”, *NASA Langley Technical Report Server.* Rdp3418.tex. 1998.

[Balanis1989] Balanis C. A. “Advanced Engineering Electromagnetics” John Wiley ans Sons, Inc. 1989

[Beard2002] Beard M. C., Turner G. M., Schmuttenmaer C. A. “Progress towards two-dimensional biomedical imaging with THz spectroscopy” *Physics in Medicine and Biology*, 47 (21), pp. 3841-3846. 2002.

[Beer1852] Beer A., “Bestimmung der Absorption des rothen Lichts in farbigen Flüssigkeiten”. *Annual Review of Physical Chemistry.* 86 78–88. 1852.

[Bram2001] Bramble S. K., Carapezza E. M., Rudin L. I. “Passive millimetre-wave concealed weapon detection”. *Enabling Technologies for Law Enforcement and Security*. 2001.

[Brown2006] Brown E. R., Lee A. W. M., Navi B. S., Bjamason J. E. “Characterization of a planar self-complementary square-spiral antenna in the THz region” *Microwave and Optical Technology Letter.* Volume 48, Issue 3, pages 524–529. 2006

[Chan2007] Chan W. L., Deibel J., Mittleman D. M. “Imaging with terahertz radiation”. *Reports on Progress in Physics*, 70(8), 1325-1379. 2007

[Guenter1990] Guenther R.. “Modern Optics”. John Wiley & Sons Inc. New York 1990

[Chen2007] Chen, J., Chen, Y., Zhao, H., Bastiaans, G. J. and Zhang, X. "Absorption coefficients of selected explosives and related compounds in the range of 0.1-2.8 THz", *Optics Express,* vol. 15, no. 19, pp. 12060-12067. 2007

[Cheo1978] Cheo P. K “Far-infrared laser system for detection of defects in polyethylene-insulated power cables” *Optics Letters*, Vol. 2, Issue 2, pp. 42-44. 1978.

[Choi2004] Choi, M. K., Bettermann, A., Van Der Weide, D. W., Crompton, A., Roskos, H., Unterrainer, K., Withington, S. and Smith, G. "Potential for detection of explosive and biological hazards with electronic terahertz systems", *Philosophical Transactions of the Royal Society A: Mathematical, Physical and Engineering Sciences,* vol. 362, no. 1815, pp. 337-349. 2004

[Collings2008] Collings N., Georgiou A., Crossland B. and Christmas J. “Projection display using computer-generated phase screens”. *SPIE Newsroom.* 2008.

[Crowe2005] Crowe T. W., Porterfield D. W., Hesler J. L, Bishop W. L., Kurtz D. S. and Hui K. “Terahertz sources and detectors”, *Proceedings of SPIE* 5790 , art. no. 32 , pp. 271-280. 2005

[CST] CST Antenna Magus [Online]. Available: http://www.cst.com

[deMaagt2006] De Maagt, P. “Terahertz technology for space and earth applications” *European Space Agency*, (Special Publication) ESA SP 626 SP. 2006

[Duvi1996] Duvillaret, L., Garet, F., and Coutaz, J. L. “A reliable method for extraction of material parameters in terahertz time-domain spectroscopy”, *IEEE Journal of Selected Topics in Quantum Electronics.* 2, (3), pp. 739–746. 1996.

[Etayo2012] Etayo D., Maestrojuán I., Teniente J., Ederra I. and Gonzalo R. “Experimental Explosive Characterization for Counterterrorist Investigation”. *Journal of Infrared, Millimeter, and Terahertz Waves*. Volume 34, Issue 7-8, pp 468-479. 2013

[Fattinger1989] Fattinger C, Grischkowsky D. “Terahertz beams”. *Applied Physic Letter.* 54(6):490-492. 1989.

[Federici2012] Federici J. F., “Review of moisture and liquid detection and mapping using Terahertz imaging” *Journal of Infrared, Millimeter, and Terahertz Waves*, 33 (2), pp. 97-126. 2012.

[Ferguson2002]Ferguson B. and Zhang X. “Materials for terahertz science and technology”. *Nature Materials,* 1(1), 26-33. 2002

[Fresnel1866] Fresnel A. J., "Calcul de l'intensité de la lumière au centre de l'ombre d'un ecran et d'une ouverture circulaires eclairés par un point radieux", *Oeuvres Complètes d'Augustin Fresnel, Imprimerie Impériale*, Paris, 1866.

[Gebbie1970] Gebbie H. A. “Some uses of submillimeter waves in science and technology” *Proceeding. Symposium on Submillimeter Waves* Polytechnic Press of the Polytechnic Institute of Brooklyn. 1970.

[Guan2011] Y. Guan, K. Mizukoshi, K. Suizu, K. Kawase. “THz techniques for human skin measurement” *Progressing Biomedical Optics and Imaging - Proceedings of SPIE,* 7897, art. no. 78970D. 2011.

[Gum2009] Gumbmanss F., Tran P., Cenanovic A. and Methfessel S. “Millimeter-wave imaging concepts: synthetic aperture radar (SAR) and digital beam forming (DBF)”. *Frequenz*, 63(5-6), 106-110. 2009

[Guo2010] Guo, Y. J., Barton S. K. “Fresnel Zone Antennas” *Kluwer Academic Publishers*. 2010.

[Hadjiloucas2002]Hadjiloucas S., Galvão R. K. H. and Bowen J. W., "Analysis of spectroscopic measurements of leaf water content at terahertz frequencies using linear transforms" *Journal of the Optical Society of America A: Optics and Image Science, and Vision*, vol. 19, no. 12, pp. 2495-2509, 20. 2002.

[Haring2000] Brucherseifer M., Nagel M., Haring Bolivar P., Kurz H., Bosserhoff A. and Büttner R. “Label-free probing of the binding state of DNA by time-domain terahertz sensing “ *Applied Physics Letter*. 77, 4049. 2000.

[Haring2003] Bolivar P. H., Brucherseifer M, Rivas J. G., Gonzalo R., Ederra I., Reynolds A. L., et al. “Measurement of the dielectric constant and loss tangent of high dielectric-constant materials at terahertz frequencies” *IEEE Transactions on Microwave Theory and Techniques* 51 (4 I) , pp. 1062-1066. 2003.

[Hartwick1976] Hartwick T. S., Hodges D. T., Baker D. H. and Foote F. B. “Far infrared imagery” *Applied Optics.* 15 1919–22. 1976.

[Hoffmann2006]Hoffman M. “Novel Techniques in THz-Time-Domain-Spectroscopy” *Ph.D. Dissertation*. Albert-Ludwigs-UniversitÄat Freiburg. 2006.

[Hristov2000] Hristov H. D. “Fresnel Zones in Wireless Links, Zone Plate Lenses and Antennas” *Artech House, Inc*. Boston, 2000.

[Hu1995] Hu B. B. and Nuss M. C., “Imaging with terahertz waves” *Optics Letters*, Vol. 20, Issue 16, pp. 1716-1718. 1995.

[Huang2004] Huang, F., Schulkin, B., Altan, H., Federici, J. F., Gary, D., Barat, R., Zimdars, D., Chen, M. and Tanner, D. B. "Terahertz study of 1,3,5-trinitro-s-triazine by time-domain and Fourier transform infrared spectroscopy", *Applied Physics Letters,* vol. 85, no. 23, pp. 5535-5537. 2004.

[Hunsche1998]Hunsche S. Mittleman D. M., Koch M. and Nuss M. C. “New dimensions in T-ray imaging”. *IEICE Transactions on Electronics*, E81-C(2), 269-275. 1998.

[Huygens1690]Huygens C., “Traitė de la Lumiere” *Gauthier-Villars Ed.* Leyden. 1690.

[Ipac] Infrared Processing and Analysis Center [Online]. Available: http://www.ipac.caltech.edu/

[ITS1996] Institute for Telecommunication Sciences [Online]. Available: http://www.its.bldrdoc.gov/

[Jaeger2002] Jaeger, R. C. "Lithography. Introduction to Microelectronic Fabrication" (2nd ed.). *Upper Saddle River: Prentice Hall*. 2002.

[Jansen2010] Jansen C., Wietzke S., Peters O., Scheller M., Vieweg N., Salhi M., Krumbholz N., Jördens C., Hochrein T. and Koch M. "Terahertz imaging: applications and perspectives" *Applied Optics.* Vol. 49, No. 19. 2010

[Jepsen2005] Jepsen P. U., Fischer B. M. "Dynamic range in terahertz time-domain transmission and reflection spectroscopy" *Optics Letters*, Vol. 30, Issue 1, pp. 29-31. 2005.

[Johnson1961] Johnson R. C., Jasik H., "Antenna Engineering Handbook", Second Edition, *McGraw Hill Book Co.* 1961

[Kemp2011] Kemp, M. C. "Explosives detection by terahertz spectroscopy - A bridge too far?", *IEEE Transactions on Terahertz Science and Technology,* vol. 1, no. 1, pp. 282-292. 2011.

[Kindt1996] Kindt J. T. and Schmuttenmaer C. A. "Far-Infrared Dielectric Properties of Polar Liquids Probed by Femtosecond Terahertz Pulse Spectroscopy". *Journal of Physical Chemistry* 100, 10373-10379. 1996

[Koch1998] Koch M., Hunsche S. Schuacher P., Nuss M. C., Feldmann J., Fromm J. "THz-imaging: A new method for density mapping of wood". *Wood Science and Technology*. Volume 32, Issue 6, Pages 421-427. 1998

[Leahy2007a] Leahy-Hoppa M. R., Fitch M. J., Zheng X, Hayden L. M., Osiander R. "Wideband terahertz spectroscopy of explosives" *Chemical Physics Letter.* 434 (4-6), pp. 227-230 2007.

[Leahy2007b] Leahy-Hoppa, M. R., Fitch, M. J., Zheng, X., Hayden, L. M. & Osiander, R. "Molecular absorption cross-section and absolute absorptivity in the THz frequency range for the explosives TNT, RDX, HMX, and PETN" *Chemical Physics Letters* 443 (4-6) , pp. 284-288. 2007.

[Lee2009] Lee Y. S. "Principles of Terahertz Science and Technology". *Springer*. 2009

[Lie1991] Liebe, H. J., Hufford, G. A., Manabe, T. "A model for the complex permittivity of water at frequencies below 1 THz". *International Journal of Infrared and Millimeter Waves*. Volume 12, Issue 7, 659-675. 1991.

[Liu2006] Liu H.-B., Chen Y., Bastiaans G. J. and Zhang X.-C., "Detection and identification of explosive RDX by THz diffuse reflection spectroscopy," *Optics Express*, vol. 14, no. 1, pp. 415-23. 2006.

[Mao 2009] Mao J., Xu Y., Zhang R., Yang M. and Liu J. "Analysis of microstrip discontinuities and their compensation via the finite difference time domain method" *International Conference on Microwave Technology and Computational Electromagnetics ICMTCE*. p. 235 – 237. 2009.

[Martin1967] Martin D. H. "Spectroscopic Techniques for Far-Infrared. Submillimeter, and Millimeter Waves". *North-Holland Publ*. 1967.

[Martin2007] Martin C. A., Lovberg J. A., Ibrahim E. "High resolution passive millimeter-wave security screening using few amplifiers". *Proceedings of SPIE 6548, Passive Millimeter-Wave Imaging Technology X*. 2007

[Maxwell1904] Maxwell-Garnett, J. C. "Colours in metal glasses and in metallic films", *Philosophical Transactions of the Royal Society, Series A*, 203, 385–420. 1904.

[May2009] May T., Zieger G., Anders S.,Zakosarenko V., Meyer H. G., Schubert M.,Sarkloff M., Rössler M., Thorwirth G.,Krause U. "Safe VISITOR: Visible, infrared and terahertz object recognition for security screening application". *Proceedings of SPIE 7309, Passive Millimeter-Wave Imaging Technology XII.* 2009.

[Mayes1992] Mayes P. E., "Frequency-Independent Antennas and Broad-Band Derivatives Thereof", *Proceedings of the IEEE*, Volume: 80 , Issue: 1, 103 – 112. 1992

[Meditherm] Meditherm Inc. [Online]. Available: http://www.meditherm.com

[Mehta2012] Mehta A. "Ultraviolet-Visible (UV-Vis) Spectroscopy – Derivation of Beer-Lambert Law" *Analytical Chemistry Notes.* 2012.

[Minim2004] Minin O. V., Minin I. V., "Difractional Optics of Millimetre Waves". *Institute of Physics Publishing*, 2004.

[Minin2010] Minin O. V., Minin I. V., "*Basic principles of Fresnel Antenna Arrays". Springer* , 2010

[Mittleman1996]Mittleman D. M., Jacobsen R. H., Nuss M. C., "T-ray imaging" *IEEE Journal on Selected Topics in Quantum Electronics*, 2 (3), pp. 679-692. 1996

[Mittleman1997]Mittleman D M, Hunsche S, Boivin L and Nuss M C "T-ray tomography" *Optics Letters*. 22 904–06.1997.

[Mittleman2003]Mittleman D. M. "Sensing with Terahertz Radiation". *Springer. Optical Sciences*. 2003.

[Mukherjee2008]Mukherjee P. and Gupta B. "Terahertz (THz) frequency sources and antennas - A brief review". *International Journal of Infrared and Millimeter Waves,* 29(12), 1091-1102. 2008.

[Naft2007] Naftaly M. and Miles, R. E. "Terahertz time-domain spectroscopy for material characterization", *Proceedings of the IEEE,* vol. 95, no. 8, pp. 1658-1665. 2007.

[Nagatsuma2009]Nagatsuma T. “Generating millimeter and terahertz waves”. *IEEE Microwave Magazine.* 10(4),64 – 74. 2009.

[OML] Oleson Microwave Laboratories [Online]. Available: http://www.omlinc.com/

[Oppenheim1998]Oppenheim A. V., Willsky A. S., Nawab S. H. “Señales y Sistemas” *Pearson Education*. 1998

[Palka2010] Palka N. “Spectroscopy of explosive materials in the THz range” *Acta Physica Polonica* A 118(6):1229-1231. 2010.

[Parasoglou2009]Parasoglou P., Parrott E. P. J., Zeitler J. A., Rasburn J., Powell H., Gladden L. F., Johns M. L.. “Quantitative moisture content detection in food wafers” *34th International Conference on Infrared, Millimeter, and Terahertz Waves, IRMMW-THz 2009*. 2009

[Peiponen2007] Peiponen K. E., “Imaging through the atmosphere at terahertz frequencies”. *IEEE MTT-S International Microwave Symposium, IMS 2007.* 2007.

[Peiponen2013]Peiponen K. E., Zeitler J. A., Kuwata-Gonokami M. “Terahertz Spectroscopy and Imaging”. *Springer Series in Optical Sciences*. 2013

[Pradarutti2007]Pradarutti B., Matthäus G., Riehemann S., Notni G., Nolte S. and Tünnerman A. “Advanced analysis concepts for terahertz time domain imaging”. *Optics Communications*, 279(2), 248-254. 2007.

[Rudd2000] Rudd J. V., Johnson J. L. and Mittleman D. M. “Quadrupole radiation from terahertz dipole antennas” *Optics Letters*. 25 1556–8. 2000

[Rudd2001] Rudd J. V., Johnson J. L. and Mittleman D. M. “Cross-polarized angular emission patterns from lens-coupled terahertz antennas” *Journal of the Optical Society of America* B 18 1524–33. 2001

[Sato2011] Sato N., Kitagawa J. and Kadoya Y. “THz Pulse Propagation on Microstrip Discontinuities” *Journal of Infrared, Millimeter, and Terahertz Waves*, Volume 32, Issue 5, pp.666-672. 2011.

[Sciencecodex] Sciencecodex [Online]. Available http://www.sciencecodex.com/

[Shen1976] Shen Y. R. “Far-infrared generation by optical mixing”. *Progress in Quantum Electronics* 4(PART 3):207-232. 1976.

[Shen2004] Shen Y., Taday P. F. and Kemp M. C. 2004, "Terahertz spectroscopy of explosive materials". *Passive Millimetre-Wave and Terahertz Imaging and Technology*. 2004.

[Siegel2004] Siegel P. H., “Terahertz technology in Biology and Medicine”, *IEEE Transactions on Microwave Theory and Techniques*. vol. 52, no. 10, pp. 2438-2447. 2004.

[Sierra2003] Sierra M., Galocha B., Fernandez J. L and Sierra M. “Electronica de comunicaciones” *Pearson. Prentice Hall*. 2003

[Sim2009] Sim Y. C., Maeng I. and Son J. “Frequency-dependent characteristics of terahertz radiation on the enamel and dentin of human tooth”. *Current Applied Physics*, 9(5), 946-949. 2009

[Smith2001] Smith R. M. and Appleby R. “Polarimetric passive millimetre wave imaging”. *Passive Millimeter-Wave Imaging Technology V*. 2001.

[Teraview] Teraview [Online]. Available: http://www.teraview.com

[Thorlabs] Thorlabs [Online]. Available: http://www.thorlabs.com

[Thrane1995] Thrane L., Jacobsen R. H., Uhd Jepsen P. and Keiding S. R. “THz reflection spectroscopy of liquid water”. *Chemical Physics Letters* 240(4):330-333. 1995.

[Tomp1999] Tompkins H. G. and McGahan W. A. “Spectropic ellipsometry and reflectometry” *John Wiley and Sons, Inc*. 1999.

[Tomp2005] Tompkins H. G and Irene E. A. “Handbook of ellipsometry” *William Andrew Publications. Springer*. 2005

[Ung2007] Ung B., Balakrishnan J., Fischer B., Ng B.W. and Abbott, D. "Terahertz detection of substances for security related purposes", *Smart Structures, Devices, and Systems III*. 2007

[VDI] Virginia Diodes [Online]. Available: http://vadiodes.com/

[vdValk2005] van der Valk N. C. J., van der Marel W. A. M. and Planken P. C. M. “Terahertz polarization imaging” *Optics Letters*. 30 2802–04. 2005.

[Velmex] Velmex [Online]. Available: http://www.velmex.com

[Volk1985] Volkov A. A., Goncharov Y. G., Kozlov G. V., Lebedev S. P. and Prokhorov A. M. “Dielectric measurements in the submillimeter wavelength region”. *Infrared Physics*. 25(1-2):369-373. 1985

[Volk1989] Volkov A. A., Kozlov G. V. and Prokhorov A. M. “Progress in submillimeter spectroscopy of solid state”. *Infrared Physics.* 29(2-4):747-752. 1989.

[Wilk2008] Wilkinson J., Caulder S. M., Portieri A. “Manufacturing process effects on the terahertz spectra of RDX” *Proceedings of SPIE 6949, Terahertz for Military and Security Applications VI*. 2008.

[William1976] William I. O. “Beam Antenna Handbook”, 5th Edition. *Radio Publications, Inc*. 1976.

[Wooten1972] Wooten F. “Optical Properties of Solids” *Academic Press*. 1972

[Wu1996a] Wu Q., Hewitt T. D. and Zhang X.-C. “Two-dimensional electro-optic imaging of THz beams” *Applied Physics Letters*. 69 1026–8. 1976.

[Wu1996b] Wu Q., Sun F. G., Campbell P. and Zhang X.-C. “Dynamic range of an electro-optic field sensor and its imaging applications” *Applied Physics Letters.* 68 3224–6. 1996

[Yamamoto2004]Yamamoto K., Yamaguchi M., Miyamaru F., Tani M., Hangyo M., Ikeda T., Matsushita A., Koide K., Tatsuno M. and Minami Y. "Noninvasive inspection of C-4 explosive in mails by terahertz time-domain spectroscopy", *Japanese Journal of Applied Physics, Part 2: Letters,* vol. 43, no. 3 B, pp. L414-L417. 2004.

[Yan2008] Yan Z., Hou D., Huang P., Cao B., Zhang, G. and Zhou Z. "Terahertz spectroscopic investigation of L-glutamic acid and L-tyrosine", *Measurement Science and Technology,* vol. 19, no. 1. 2008.

[Yang1973] Yang K. H., Morris J. R., Richards P. L. and Shen Y. R. “Phase-matched far-infrared generation by optical mixing of dye laser beams” *Applied Physics Letters.* 23 669–71. 1973.

[Zhang2008] Zhang H., Mitobe K. and Yoshimura N., "Terahertz imaging for water content measurement", *International Symposium on Electrical Insulating Materials, ISEIM 2008*. 2008.

[Zomega] Zomega [Online]. Available: http://www.zomega.com

[Zwie1990] Zwietering M. H., Jongenburger I., Rombouts F. M., van 'T Riet K. "Modeling of the Bacterial Growth Curve". *Applied and Environmental Microbiology* 56 (6): 1875–1881. 1990.

LIST OF PUBLICATIONS

Journal Papers

1.D. Etayo, I. Maestrojuan, & J. Teniente, I. Ederra and R. Gonzalo. "Experimental Explosive Characterization for Counterterrorist Investigation" Journal of Infrared Millimeter and Teraherzt Waves (2013) 34:468–479

International Conferences

1.David Etayo, Juan Carlos Iriarte, Inés Palacios, Ramón Gonzalo. Active THz inspection of water content in plants. SPIE Defense, Security, and Sensing 2010 Orlando, USA. 5-9 April 2010

2.Juan Carlos Iriarte, **David Etayo**, Iñigo Ederra, Ramón Gonzalo. Active THz inspection of water content in plants. EUCAP 2010 Conference. Barcelona; Spain.12-16 April 2010

3.Juan Carlos Iriarte, **David Etayo**, Inés Palacios, Itziar Maestrojuan, Iñigo Liberal, Ainara Rebollo, Jorge Teniente, Iñigo Ederra, Ramón Gonzalo. Water Content Evolution in Leaves Based on Active THz Imaging System. EUCAP 2011 Conference. Rome, Italy. 11-15 April 2011

4.*David Etayo*, *Juan Carlos Iriarte, Inés Palacios, Itziar Maestrojuan, Jorge Teniente Iñigo Ederra, Ramón Gonzalo.* THz Imaging System for Industrial Quality Control. 2011 Emerging Wireless Technologies Week. Sitges, Spain. 15-16 September 2011

5.Itziar Maestrojuán; Ines Palacios ; Ainara Rebollo; **David Etayo**; Jorge Teniente; Iñigo Ederra; Ramon Gonzalo. Development of a Sub-Harmonic Mixer Working at 220 GHz. 2011 Emerging Wireless Technologies Week. Sitges, Spain. 15-16 September 2011

6.David Etayo, Juan Carlos Iriarte, Inés Palacios, Iñigo Ederra, Ramón Gonzalo. Active THz imaging system to measure water content evolution in leaves. SPIE Defense, Security, and Sensing 2011. Prage, Czech Republic. 19-22 September 2011

7.Itziar Maestrojuan, **David Etayo**, Inés Palacios, Juan Carlos Iriarte, Iñigo Ederra, Ramón Gonzalo. Explosives Characterization in the THz Range. SPIE Defense, Security, and Sensing 2011.. Prage, Czech Republic. 19-22 September 2011

National Conferences

1.David Etayo, Juan Carlos Iriarte, Inés Palacios, Itziar Maestrojuan, Iñigo Liberal, Ainara Rebollo, Jorge Teniente, Iñigo Ederra, Ramón Gonzalo. Evolución del Contenido en Agua de Hojas Basado en Imágenes Activas en Terahercios. XXVI Simposium Nacional de la Unión Científica Internacional de Radio (URSI 2011). Madrid; Spain.7-9 September 2011

2.Itziar Maestrojuan, **David Etayo**, Inés Palacios, Jorge Teniente, Iñigo Ederra, Ramón Gonzalo. Caracterización de Explosivos en el rango de los THz. XXVI Simposium Nacional de la Unión Científica Internacional de Radio (URSI 2011). Madrid; Spain. 7-9 September 2011

3.David Etayo, Juan Carlos Iriarte, Inés Palacios, Iñigo Liberal, José Luis Martínez de Falcón,Itziar Maestrojuan, Iñigo Ederra, Jorge Teniente, Ramón Gonzalo. Tecnología de THz para la caracterización del contenido en agua en plantas. XXV Simposium Nacional de la Unión Científica Internacional de Radio (URSI 2010). Bilbao; Spain. 15-17 September 2010.